Antenna Array Design for Retrodirective Wireless Power Transmission and Radar

Pascual D. Hilario Re

Submitted for the degree of Doctor of Philosophy

School of Engineering & Physical Sciences

Heriot-Watt University

April 2019

Abstract

This thesis presents antenna array design and the integration of microwave circuit systems for retrodirective wireless power transmission and radar. Wireless power transmission (WPT) and automotive radar are emerging topics which have attracted a lot of interest in the past few years. The development of these systems usually brings high associated costs if competitive performance is required. The first part of the thesis is concerned with the development of a new retrodirective antenna array (RDA) system for WPT which uses sub-arrays in transmit to save costs, however, losing tracking in one plane. Nevertheless, depending on the application, the proposed system might be an alternative solution to existing approaches as similar performances are achieved, but at generally a lower cost for the proposed RDA design as compared to the conventional solution. The proposed system has been designed to work in the ISM band (2.5 GHz for receiving and 2.4 GHz for transmitting) which exhibits an 80° 3-dB half-power beamwidth for the monostatic pattern. Additionally, it has been demonstrated that the system is able to work in the near-field region, being able to achieve wireless charging of a handeld electronic device at a 50 cm distance. The power for the beacon signal sent by the device to be charged by the system (for tracking purposes) is 6.6 dBm, whereas the received RF power from the RDA is in excess of 27 dBm, which means that the device is receiving a hundred times the power sent for battery charging.

On the other hand, the second part of the thesis relates to the development of two important elements within a frequency-modulated-continuous-wave (FMCW) automotive radar working at 24 GHz: a substrate integrated waveguide (SIW) butler matrix antenna array as the transmitter and a new post-processing technique called Pwr_+. These two in combination bring some interesting advantages in terms of angular resolution improvements when compared to conventional single-input-multiple-

output (SIMO) radars. For example, the proposed system is able to distinguish two targets which are 2 degrees apart as well as a higher field-of-view (FOV) thanks to the beamforming network that generates 4 individual beams covering a wide FOV. The newly developed radar system is also comparable to multiple-input-multiple-output (MIMO) radars but with the added value of having a shorter processing time, which for automotive radar applications is a crucial characteristic to be minimized, and could, therefore, avoid potential road accidents.

It should also be mentioned that this thesis was supported by the Samsung Advanced Institute of Technology.

Dedication

To my parents, for having raised me through life
with humility, effort and respect to others.

To my sister, which has been and will always be a role model.
I will never meet a better person than her.

And to Estela, even though life put us on different paths,
she has always been an unconditional support in every moment.

A mis padres, por haberme enseñado la vida a través
de la humildad, el esfuerzo y el respeto a los demás.

A mi hermana, la cual ha sido y será un espejo en el que mirarme.
Nunca conoceré a mejor persona que ella.

Y a Estela que, aunque la vida nos haya hecho tomar caminos distintos,
ha sido un apoyo incondicional en todo momento.

Acknowledgements

I would like to express my most sincere gratitude to my supervisor Dr. Symon K. Podilchak for always having a positive attitude and making me change my personal view of research, from an impossible challenge to an opportunity to learn, be creative and grow as engineer. His infinite patience and passion for microwaves is inspiring to many of us in the Microwave Group. This gratitude goes beyond the professional sphere, as he supported me over tough times as a big brother would do.

I would also like to thank Dr. Reza Mohammadi for being like a father, always willing to help and give useful advices. Even though he is an awful football player, he deserves my infinite respect.

Thanks also to Prof. George Goussetis for giving me the opportunity to join this group and to Dr. José Luis Gómez Tornero for encouraging me to come to Edinburgh which has been one of the best decisions I ever made.

A special thanks goes to all my colleagues and friends in the Microwave Group at Heriot-Watt University. Specially to José Antonio, Salvador, Adrián, Carlos, Victoria, María Jesús, María, Julia, Costas, Cristian, Dave Watson, Rahil, Alex, Sam, Wenxing, Jia-ni, Ross, Ibrahim, Jessica, Zhou-Zhou, Spyros, Sadeque, Khaled, Hassan and Dave Czerski. It has been a wonderful experience to share uncountable hours and interesting discussions, learning together and always helping each other.

Thanks also to the guys from the electrical workshop, to Steve and our old superintendent Alistair for being such nice people and professionals.

Finally, thanks to the colleagues I found along the way which I had the pleasure to collaborate with on very interesting works: Davide from Sapienza Universitá di Roma, Paul from Université de Rennes, Miguel from Universidad Politécnica de Cartagena and Colum and Kieran, old MSc students from Heriot-Watt University.

Research Thesis Submission

Please note this form should be bound into the submitted thesis.

Name:	Pascual David Hilario Re		
School:	Engineering and Physical Sciences (EPS)		
Version: *(i.e. First, Resubmission, Final)*	Final	Degree Sought:	PhD. (Electrical Engineering)

Declaration

In accordance with the appropriate regulations I hereby submit my thesis and I declare that:

1. The thesis embodies the results of my own work and has been composed by myself
2. Where appropriate, I have made acknowledgement of the work of others
3. The thesis is the correct version for submission and is the same version as any electronic versions submitted*.
4. My thesis for the award referred to, deposited in the Heriot-Watt University Library, should be made available for loan or photocopying and be available via the Institutional Repository, subject to such conditions as the Librarian may require
5. I understand that as a student of the University I am required to abide by the Regulations of the University and to conform to its discipline.
6. I confirm that the thesis has been verified against plagiarism via an approved plagiarism detection application e.g. Turnitin.

ONLY for submissions including published works

Please note you are only required to complete the Inclusion of Published Works Form (page 2) if your thesis contains published works)

7. Where the thesis contains published outputs under Regulation 6 (9.1.2) or Regulation 43 (9) these are accompanied by a critical review which accurately describes my contribution to the research and, for multi-author outputs, a signed declaration indicating the contribution of each author (complete)
8. Inclusion of published outputs under Regulation 6 (9.1.2) or Regulation 43 (9) shall not constitute plagiarism.

* *Please note that it is the responsibility of the candidate to ensure that the correct version of the thesis is submitted.*

Signature of Candidate:		Date:	09/09/2019

Submission

Submitted By *(name in capitals):*	
Signature of Individual Submitting:	
Date Submitted:	

For Completion in the Student Service Centre (SSC)

Limited Access	Requested	Yes		No		Approved	Yes		No	
E-thesis Submitted (***mandatory for final theses)***										
Received in the SSC by *(name in capitals):*						Date:				

Inclusion of Published Works

Please note you are only required to complete the Inclusion of Published Works Form if your thesis contains published works under Regulation 6 (9.1.2)

Declaration

This thesis contains one or more multi-author published works. In accordance with Regulation 6 (9.1.2) I hereby declare that the contributions of each author to these publications is as follows:

Citation details	P.D. Hilario Re, S.K. Podilchak, S. Rotenberg, G. Goussetis, and J. Lee, "Circularly Polarized Retrodirective Antenna Array for Wireless Power Transmission," IEEE Transactions on Antennas and Propagation, 2019, (accepted with revisions).
P.D. Hilario Re	Theoretical analysis, simulations, measurements, post-processing and writing of the paper.
S.K. Podilchak	Supervision, guidance, corrections.
S. Rotenberg	Measurements
G. Goussetis and J. Lee	Guidance
Signature:	
Date:	09/09/2019

Citation details	P.D. Hilario Re, D. Comite, and S.K. Podilchak, "Single-Layer Series-Fed Array with Controlled Aperture Distribution for Circularly Polarized Radiation," IEEE Transactions on Antennas and Propagation, 2019, (accepted with revisions).
P.D. Hilario Re	Theoretical analysis, simulations, measurements, post-processing and corrections.
D. Comite	Writing of the paper
S.K. Podilchak	Supervision, guidance, corrections.
Signature:	
Date:	09/09/2019

Citation details	P. Le Bihan, P.D. Hilario Re, D. Comite, S.K. Podilchak, C. Tucker, K. MacColl, Y. Zhaksylyk, M. García-Vigueras, and G. Goussetis, "Dual-Polarized Aperture-Coupled Patches with Application to Retrodirective and Monopulse Arrays," IEEE Access, 2019, (accepted with revisions).
P. Le Bihan	Theoretical analysis, simulations, measurements, post-processing and writing of the paper (80%).
P.D. Hilario Re	Measurements, post-processing, writing of the paper (20%) and corrections.
D. Comite	Corrections
S.K. Podilchak	Supervision, guidance and corrections.
C. Tucker, K. MacColl, Y. Zhaksylyk	Simulations and manufacturing.
Signature:	
Date:	09/09/2019

Contents

List of Figures

List of Tables

Glossary

ACC	Autonomous cruise control
AR	Axial ratio
AUT	Antenna under test
BM	Butler matrix
BMA	Butler matrix antenna
BPF	Band-pass filter
BW	Bandwidth
CP	Circular polarization
CW	Continuous wave
CWS	Collision warning system
DAMS	Diamond antenna measurement studio
DC	Direct current
DUC	Device under charge
EIRP	Effective isotropic radiated power
ESPRIT	Estimation of signal parameters via rotational invariance techniques
ETSI	European telecommunications standards institute
FCC	Federal communications commission
FF	Far-field
FM	Frequency modulation
FMCW	Frequency modulated continuous wave
FOV	Field of view
FSPL	Free space path loss
IC	Integrated circuit
IF	Intermediate frequency
LHCP	Left-handed circular polarization
LNA	Low noise amplifier

LO	Local oscillator
LP	Linear polarization
LRR	Long range radar
MIMO	Multiple input multiple output
ML	Maximum likelihood
MLD	Main lobe direction
MPT	Microwave power transfer
MRR	Medium range radar
MTI	Moving target indication
MUSIC	Multiple signal classification
MVDR	Minimum variance distortionless response
NF	Near-field
PA	Power amplifier
PNA	Programmable network analyzer
RADAR	Radio detection and ranging
RDA	Retrodirective antenna
RF	Radio-frequency
RHCP	Right-handed circular polarization
RX	Receiver
SFA	Series-fed array
SIMO	Single input multiple output
SIW	Substrate integrated waveguide
SLL	Side lobe level
SMT	Surface mount technology
SRR	Short range radar
TE	Transverse electric
TL	Transmission line
TOF	Time of fly
TX	Transmitter
VCO	Voltage controlled oscillator
VSWR	Voltage standing wave ratio
WPT	Wireless power transmission

List of Symbols

ψ_i	Progressive phase relative to the preceding element within an array (rad)
ω	Angular frequency (rad/s)
$v(t)$	Instantaneous voltage (V)
V_{pp}	Peak to peak voltage
λ_0	Wavelength in free-space (m)
λ_g	Guided wavelength (m)
R_1	Boundary distance between reactive near-field and radiative near-field (m)
R_2	Boundary distance between radiative near-field and far-field (m)
D	Maximum linear distance of an antenna aperture (m)
k	Wavenumber (rad/m)
β	Progressive phase lead current excitation in an array element relative to the preceding one (rad)
ε_{eff}	Effective permittivity
ε_{r}	Relative permittivity
$\tan\delta$	Loss tangent
c	Speed of light (m/s)
f	Frequency (Hz)
Z_{in}	Input impedance (Ω)
Z_0	Characteristic impedance of a transmission line (Ω)
S_{ij}	Scattering parameters from port j to port i (dB)
T	Period (s)
R	Range from the radar to the target (m)
f_B	Beat frequency (Hz)

List of publications

Journal Papers

1. **P.D. Hilario Re**, S.K. Podilchak, S. Rotenberg, G. Goussetis, and J. Lee, "Circularly Polarized Retrodirective Antenna Array for Wireless Power Transmission," *IEEE Transactions on Antennas and Propagation*, 2019, (accepted with revisions).

2. C. Alistarh, S.K. Podilchak, **P.D. Hilario Re**, T.M. Ströber, C. Mateo-Segura, Y. Pailhas, M. Sellathurai, G. Goussetis, Y. Petillot, J. Thompson, and J. Lee, "A High Resolution FMCW MIMO Radar System for Automotive Applications," *IEEE Transactions on Microwave Theory and Techniques*, 2019, (to be resubmitted).

3. **P.D. Hilario Re**, D. Comite, and S.K. Podilchak, "Single-Layer Series-Fed Array with Controlled Aperture Distribution for Circularly Polarized Radiation," *IEEE Transactions on Antennas and Propagation*, 2019, (accepted with revisions).

4. P. Le Bihan, **P.D. Hilario Re**, D. Comite, S.K. Podilchak, C. Tucker, K. MacColl, Y. Zhaksylyk, M. García-Vigueras, and G. Goussetis, "Dual-Polarized Aperture-Coupled Patches with Application to Retrodirective and Monopulse Arrays," *IEEE Access*, 2019, (accepted with revisions).

5. D. Comite, W. Fuscaldo, S.K. Podilchak, **P.D. Hilario Re**, V.G. Buendía, P. Burghignoli, P. Baccarelli, and A. Galli, "Microwave Generation of X-waves by Means of a Planar Leaky-Wave Antenna," *Applied Physics Letters*, vol. 113, no. 14, 2018.

6. D. Comite, W. Fuscaldo, S.K. Podilchak, **P.D. Hilario Re**, V.G. Buendía,

P. Burghignoli, P. Baccarelli, and A. Galli, "Radially Periodic Leaky-Wave Antenna for Bessel Beam Generation Over a Wide Frequency Range," *IEEE Transactions on Antennas and Propagation*, vol. 66, no. 6, pp. 2828 - 2843, Jun. 2018.

Journal Papers to be Submitted

1. **P.D. Hilario Re**, S.K. Podilchak, S. Rotenberg, G. Goussetis, and J. Lee, "Millimeter-wave FMCW radar development using SIW butler matrix and processing technique for angular resolution enhancement," *IEEE Transactions on Antennas and Propagation.*

Conferences

1. **P.D. Hilario Re**, C. Alistarh, S.K. Podilchak, G. Goussetis, J. Thompson, and J. Lee, "Millimeter-wave fmcw radar development using siw butler matrix for time domain beam steering," *16th European Radar Conference (Eu-RAD)*, Paris, France, 2019, (accepted).
2. C.A. Alistarh, **P.D. Hilario Re**, T.M. Ströber, S.A. Rotenberg, S.K. Podilchak, C. Mateo-Segura, Y. Pailhas, G. Goussetis, Y. Petillot, J. Thompson, and Jaesup Lee, "Millimetre-Wave FMCW MIMO Radar System Development using Broadband SIW Antennas," *EuCAP 2018*, London, UK, Apr. 2018.
3. P. Le Bihan, Y. Zhaksylyk, **P.D. Hilario Re**, S.K. Podilchak, M. García-Vigueras, and G. Goussetis, "Dual-Circularly Polarized Patch Antenna Using Simple Isolation Techniques and Its Array Application," *EuCAP 2018*, London, UK, Apr. 2018.
4. S. Rotenberg, **P.D. Hilario Re**, S.K. Podilchak, G. Goussetis, and J. Lee, "An Efficient Rectifier for an RDA Wireless Power Transmission System Operating at 2.4 GHz," *URSI General Assembly*, Montreal, Canada, Aug. 2017.
5. **P.D. Hilario Re**, S.K. Podilchak, S. Rotenberg, G. Goussetis, and J. Lee, "Retrodirective Antenna Array for Circularly Polarized Wireless Power Trans-

mission," *EuCAP 2017*, Paris, France, Mar. 2017.

6. **P.D. Hilario Re**, S.K. Podilchak, C. Constantinides, G. Goussetis, and J. Lee, "An Active Retrodirective Antenna Element for Circularly Polarized Wireless Power Transmission," *IEEE Wireless Power Transmission Conference*, Aveiro, Portugal, May 2016.

Chapter 1

Introduction

1.1 Motivation

Antenna array design for radar and far-field (FF) wireless power transmission are, as many other topics, in constant development. Advancements of these topics are generally translated into complex systems and even during the manufacturing, causing an increase in cost for developing the system. Therefore, one of the objectives pursued within this thesis is the aiming for a right balance between performance and simplicity which can minimize the cost but provide good performance using the state-of-the-art technology. Through this thesis, three different yet related topics are examined: wireless power transmission (WPT), antenna design and radar. From these, the commonality of antenna design and device or target tracking radar allows for proper connection and flow between chapters.

1.2 Wireless Power Transmission

Wireless power transmission (WPT) or wireless energy transfer, as its name implies, consists of the transmission of energy from a transmitter to a receiver without the need of physical connection between them. Classically this is done with wires or cables. This concept has been widely used to enable wireless charging, and has employed different techniques to achieve it. All these, can be classified as radiative or non-radiative wireless charging technologies [1] as depicted in Fig. 1.1. The radiative

ones, which embody the focus of this thesis, differentiate between *directive* from *non-directive RF power beamforming*. The first one is based on the power transferred by a propagating electromagnetic wave through directive power beaming where a narrow-beam antenna transmits power in a well-defined direction toward the receiving device [2]. On the other hand, *non-directive RF power beamforming* is based on transceivers which ignore the position of the receiver and, therefore, transmit the power in an omnidirectional beam pattern shape, relying all the challenges on the optimum RF-to-DC power conversion (rectifying efficiency) by the receivers, also called *power harvesters* [3]. Therefore, the available incident power densities are even lower, on the order of micro-watts per cm^2.

The development of radiative and non-radiative WPT occurred in parallel and it has been driven by different needs and desires and at particular moments in time, commencing at the end of the 19th century. The desire to explore and verify electromagnetic theory brought important findings primarily from Nikola Tesla, such as the transmission of microwave signals over a distance of about 48 kilometers [4] or the *Tesla coil* [5], among others. Later on, the development during the 1960s and 70s for military research projects and medical science gave a new boost for WPT to evolve from its early beginnings. For example, resonant inductive coupling was successfuly applied in implantable medical devices [6, 7]. Also during this period, the concept of the solar power satellite was firstly introduced for WPT in 1968 by Peter E. Glaser [8, 9]. Finally, the last push on the development of WPT was given during the beginning of the 21st century, driven primarily by the need of the portable electronic device market, mainly for remote battery charging. For example, in 2007 MIT scientists proposed Witricity technology [10], which by using self-resonant coils

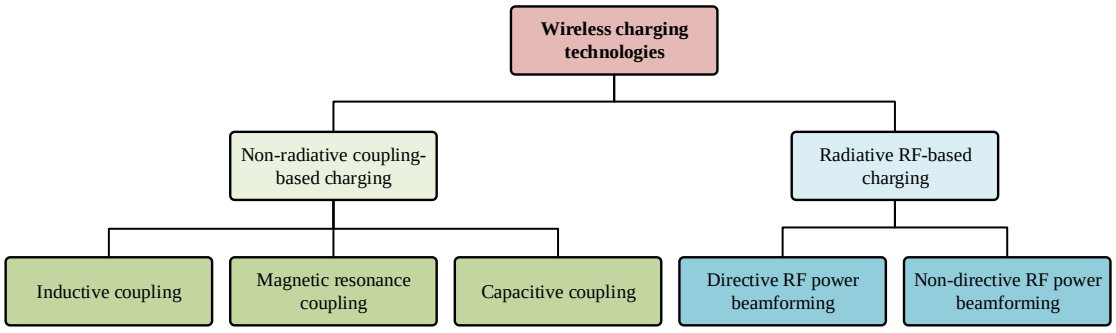

Figure 1.1: Diagram showing the different types of wireless charging technologies classified by radiative or non-radiative.

in a strongly coupled regime, is able to transfer 60 watts with about 40% efficiency over distances in excess of 2 meters (see Fig. 1.2(a)). Moreover, radiative wireless charging systems like Cota [11] in 2007 and Powercast wireless sensor system [12] in 2010, appeared in the market to cover the needs for wireless charging of handheld electronics, which experimental setups are shown in Fig. 1.2(b) and (c), respectively.

In this thesis, *directive RF power beamforming* approaches will be the ones under discussion. Some recent works on these topics are [13] and [14], on which WPT is achieved by a line-of-sight scenario and power focusing on a focal point, respectively. However, for a non-line-of-sight scenario, proper tuning of the complex weights of the array is required as in blind adaptive beamforming (BABF) or Monte-Carlo beamforming (MCBF) [15–17]. Even though these methods help reduce the FSPL, the iterative search for the optimal weight configuration could lead to a local maxima and therefore not be the best solution. Moreover, these algorithms take processing time, not being very efficient for fast moving targets.

This is overcome by the wavefront reversal concept [18]. Thus, a pilot signal can be received by an array and by either time reversing or phase conjugating it, the retransmitted signal will arrive to the original source without the need of any kind of complex algorithm or involved data processing. This is because time reversal and phase conjugation are equivalent operations, given that:

$$F(\omega_0) = \int_{-\infty}^{\infty} f(t) e^{-j\omega_0 t}\, dt \tag{1.2.1}$$

were, F corresponds to the Fourier transform of the signal in time domain $f(t)$, and ω_0 is the angular frequency. Additionally, if we apply time reversal and phase conjugation to both sides of the equation we can prove that both operations are equivalent, as shown below.

$$F^*(\omega_0) = \int_{-\infty}^{\infty} f(t) e^{j\omega_0 t}\, dt = \int_{-\infty}^{\infty} f(-t) e^{-j\omega_0 t}\, dt \tag{1.2.2}$$

By exploiting this concept, a way of achieving tracked WPT happens, also known as retrodirective arrays (RDAs) which can be defined as an array of transceivers that are able to track devices. Such devices send a beacon tone for tracking and by the relative phase difference received at each antenna element in the RDA, beam pointing for the re-radiated signal towards these devices is made possible [19] even

(a)

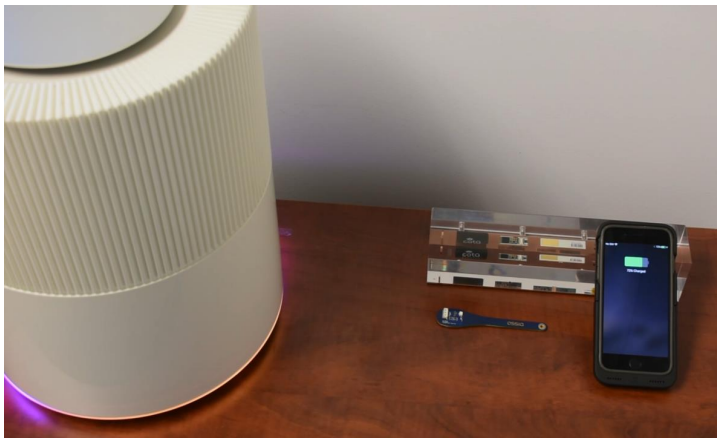

(b)

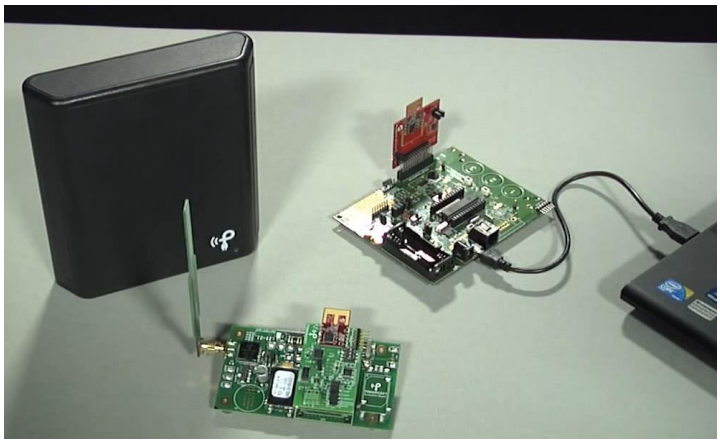

(c)

Figure 1.2: Demos for Witricity [21] (a), Cota [22] (b) and Powercast [23] (c).

on a non-line-of-sight scenario [20] and without any previous knowledge of the device location.

1.2.1 Background of the Problem

A comparison of all the aforementioned emerging commercial technologies shown in Fig. 1.2 can be found in Table 1.1. For Cota and Powercast, tracking of the device under charge (DUC) is achieved by phase conjugation and beamforming, respectively [24]. However, given that tracking is made in the digital domain, time is discretized and therefore it does not happen continuously. Also, every antenna element that is contained in these devices includes some supporting electronic circuitry, making it expensive in cases where the power delivery is high. Additionally, apart from commercially available solutions as mentioned above, the research on WPT in the FF range for small consumer electronics usually involves the use ADC/DACs, requiring a more complex solution (as in [25–27]). Also, in [2], retrodirectivity was achieved by proper adjustment of the phase shifters involving additional processing time. Thus, the research effort in the following chapters will be to overcome by these two problems. In particular, maximizing delivery of energy while finding a compromise in terms of system size, cost, and complexity by building a purely analogue system.

Table 1.1: Comparison between commercially available WPT solutions

Product	**Cota**	**Powercast**	**Witricity**
WPT Mechanism	Directive RF power beamforming	Directive RF power beamforming	Magnetic resonance coupling
No need for line-of-sight	✓	✗	✓
No need for alignment	✓	✓	✗
Tracking	✓	✓	✗
Continuous tracking	✗	✗	N/A

This cost saving, and reduced complexity can be extrapolated to other topics which make use of a low of hardware as it happens in WPT. One of these topics is automotive radar which will be discussed in the next section.

1.3 Automotive Radar

1.3.1 Historical overview

Automotive radar has its first appearance during the early 1970's in an effort to reduce automotive accidents [28]. To do so, potential components of an on-board radar include: speed sensing, radar braking, blind-spot detection and cruise control [28]. Nevertheless, apart from collision avoidance, the development of radars that enable a faster response of inflatable restraint systems for minimizing damage during accidents and hopefully saving lives, had also been investigated [29]. A couple of examples for automotive radar prototypes are shown in Fig. 1.3.

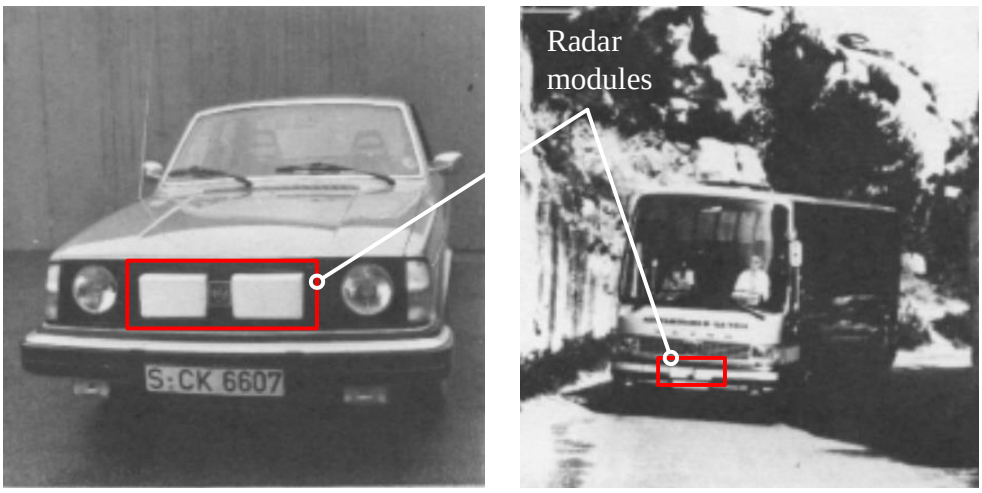

Figure 1.3: Early 70's prototype of a collision avoidance system fitted on an automobile (a) and on a bus (b) [30].

Afterwards, during the 1990s, the massive introduction of similar radar technologies in all kind of vehicles brought many discussions. For example, that collision warning system (CWS) radar made drivers to be "transparent" for their employers, putting their job and salaries on risk. However, this would not stop the installation of 24 GHz CWS radar in more than 4000 buses and trucks in the US. Many of these were monitored along 900 million km of road suggesting that the amount of accidents could be reduced by more than 50% [31]. The first actual 77 GHz automotive radar hardware was produced in 1999 by Mercedes-Benz in the S-class, the autonomous cruise control (ACC) [32], being the starting point of the inclusion of radar sensors in cars from then until today. In Fig. 1.4 it can be seen a car

with a typical arrangement for its sensors. From it, we can distinguish three types of radars regarding their operating range: short range radar (SRR), medium range radar (MRR) and long range radar (LRR), which technical specs are shown in Table 1.2.

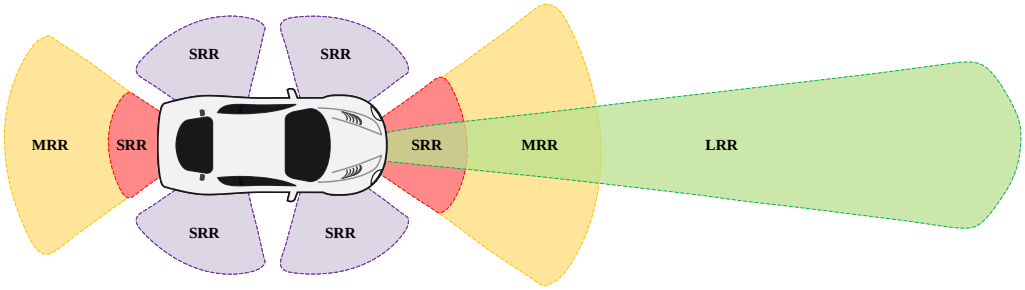

Figure 1.4: Location of radar sensors in a car.

Table 1.2: Sensor classification for automotive radar [33]

Type	**LRR**	**MRR**	**SRR**
Max. EIRP	55 dBm	-9 dBm/MHz	-9 dBm/MHz
Frequency band	76-77 GHz	77-81 GHz	77-81 GHz
Bandwidth	600 MHz	600 MHz	4 GHz
Range (min-max)	10-250 m	1-100 m	0.15-30 m
Range resolution	0.5 m	0.5 m	0.1 m
Velocity resolution	0.6 m/s	0.6 m/s	0.6 m/s
3dB beamwidth in az.	±15°	±40°	±80°
3dB beamwidth in el.	±5°	±5°	±10°

Apart from this classification, radar can also be differentiated regarding their transmitted waveform as it is depicted in Fig. 1.5 and summarized next:

- *Continuous wave (CW) RADAR*: refers to a radar that operates with a continuous signal.
  - *Unmodulated CW RADAR*: used for detecting non-stationary targets, it requires two antennas (one for transmit and one for receive). It only measures the speed of the target, but not the distance.
  - *Frequency modulated continuous wave (FMCW) RADAR*: has the addition of frequency modulation (FM) for the transmit signal, enabling

measurement of the distance apart from the velocity of the target. It also requires two antennas.

- *Pulsed RADAR*: corresponds to the radar that operates with a pulsed signal.
  - *MTI pulse RADAR*: Moving Target Indication (MTI) pulse RADAR, uses a single antenna for transmission and reception with the help of a duplexer. It distinguishes stationary from non-stationary targets by the Doppler effect.
  - *Pulse doppler RADAR*: It also uses an antenna with a duplexer. The antenna will transmit a pulse at a given rate, which must be such that the echo signal is received before the next pulse is transmitted.

From all these, FMCW radar is the most widely used in the automotive industry since 1992 [34] given that is able to measure both range and speed with high resolution [35].

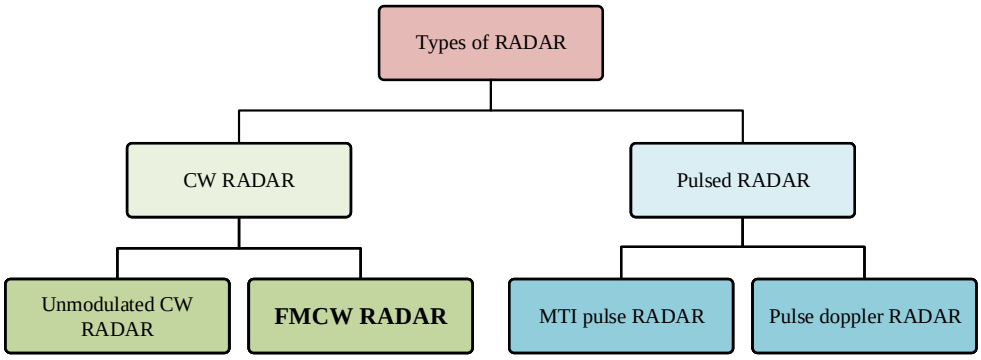

Figure 1.5: Types of RADAR depending on their transmitted signal.

1.3.2 Background of the problem

Previous radar systems generally used microstrip patch antennas for their frontend design, and if a fine resolution is required they mostly implement super-resolution techniques which can be in some cases time consuming and, therefore, accident probability could rise. In the relevant chapter of this thesis, a new radar system is presented involving the use of substrate integrated waveguide (SIW) antennas (which can have an omnidirectional pattern and are known for having lower losses and reduced dispersion at higher frequencies when compared with patch antennas) in combination with a signal post-processing technique that reaches a nice balance

between resolution and processing time. Only recently, other authors have been investigating these types of antennas. Also, the impedance bandwidth can be extended resulting in a better range resolution of the radar system. In particular, this thesis will discuss an SIW system for automotive radar introducing the *power plus* (Pwr_+) post-processing algorithm that enhances the angular resolution while also maintaining a low processing time if compared with other super resolution algorithms such as minimum variance distortionless response (MVDR) beamforming [36] and multiple signal classification (MUSIC) [37]. Generally, these algorithms can offer the high-resolution of radar targets and are based on the eigenvalue decomposition of the signals at a receiving array.

1.4 Document overview

This thesis is composed of 5 chapters, including this introductory chapter.

- Chapter 2 discusses a new retrodirective array (RDA) system for circularly polarised (CP) WPT in which the main objectives are to achieve a low cost which uses subarrays while also working in the analogue domain for continuous tracking of the device under charge (DUC), opening up the possibility to also track very fast moving objects.

- Chapter 3 proposes an alternative subarray design to the one proposed in Chapter 2, in which CP radiation is achieved by just one port and where amplitude distribution of the elements is controlled by transmission line impedance transformers. Moreover, a higher dielectric substrate was chosen to provide more compactness and therefore able to have each subarray closer together to effectively reduce the side lobe level (SLL) that strongly appeared in the earlier prototype from Chapter 2.

- Chapter 4 presents the design of an SIW array and SIW Butler matrix beamformer as well as the Pwr_+ algorithm, which when used in a radar system provides high resolution and beyond the conventional, while saving costs and processing time.

- Chapter 5 summarizes the work carried out in the thesis, proposes some conclusions and future work.

References

[1] X. Lu, P. Wang, D. Niyato, D. I. Kim, and Z. Han, "Wireless charging technologies: Fundamentals, standards, and network applications," *IEEE Communications Surveys Tutorials*, vol. 18, no. 2, pp. 1413–1452, 2016.

[2] J. O. McSpadden, F. E. Little, M. B. Duke, and A. Ignatiev, "An in-space wireless energy transmission experiment," in *IECEC 96. Proceedings of the 31st Intersociety Energy Conversion Engineering Conference*, vol. 1, Aug 1996, pp. 468–473.

[3] J. A. Hagerty, F. B. Helmbrecht, W. H. McCalpin, R. Zane, and Z. B. Popovic, "Recycling ambient microwave energy with broad-band rectenna arrays," *IEEE Transactions on Microwave Theory and Techniques*, vol. 52, no. 3, pp. 1014–1024, March 2004.

[4] N. Tesla, "Apparatus for transmitting electrical energy," U.S. Patent 1 119 732, Dec., 1914.

[5] ——, "Coil for electro-magnets," U.S. Patent 512 340, Jan., 1894.

[6] J. C. Schuder and H. E. Stephenson, "Energy transport to a coil which circumscribes a ferrite core and is implanted within the body," *IEEE Transactions on Biomedical Engineering*, vol. BME-12, no. 3 and 4, pp. 154–163, July 1965.

[7] H. Kim, H. Hirayama, S. Kim, K. J. Han, R. Zhang, and J. Choi, "Review of near-field wireless power and communication for biomedical applications," *IEEE Access*, vol. 5, pp. 21 264–21 285, 2017.

[8] P. E. Glaser, "Power from the sun: Its future," *Science*, vol. 162, no. 3856, pp. 857–861, 1968.

[9] J. O. McSpadden and J. C. Mankins, "Space solar power programs and microwave wireless power transmission technology," *IEEE Microwave Magazine*, vol. 3, no. 4, pp. 46–57, Dec 2002.

[10] A. Kurs, A. Karalis, R. Moffatt, J. D. Joannopoulos, P. Fisher, and M. Soljacic, "Wireless Power Transfer via Strongly Coupled Magnetic Resonances," *Science*, vol. 317, pp. 83–86, 2007.

[11] H. Zeine, "Wireless power transmission system," U.S. Patent 8 446 248, Jun., 2007.

[12] C. E. Greene, "Systems, methods and apparatus for powering devices using RF energy from a mobile transmitter," U.S. Patent 9 107 579, Dec., 2010.

[13] S. Yoshida, N. Hasegawa, and S. Kawasaki, "Experimental demonstration of microwave power transmission and wireless communication within a prototype reusable spacecraft," *IEEE Microwave and Wireless Components Letters*, vol. 25, no. 8, pp. 556–558, Aug 2015.

[14] V. R. Gowda, O. Yurduseven, G. Lipworth, T. Zupan, M. S. Reynolds, and D. R. Smith, "Wireless power transfer in the radiative near field," *IEEE Antennas and Wireless Propagation Letters*, vol. 15, pp. 1865–1868, 2016.

[15] P. S. Yedavalli, T. Riihonen, X. Wang, and J. M. Rabaey, "Far-field rf wireless power transfer with blind adaptive beamforming for internet of things devices," *IEEE Access*, vol. 5, pp. 1743–1752, 2017.

[16] Y. Zhao, X. Li, C. Xu, and X. Wang, "Adaptive beamforming using monte-carlo algorithm for multi-antenna wireless power transfer," in *2017 IEEE 28th Annual International Symposium on Personal, Indoor, and Mobile Radio Communications (PIMRC)*, Oct 2017, pp. 1–5.

[17] Y. Zhao, X. Li, C. Xu, and S. Zhang, "Adaptive random beamforming for mimo wireless power transfer system," in *2018 IEEE Wireless Communications and Networking Conference (WCNC)*, April 2018, pp. 1–6.

[18] C.-G. Sun and J.-L. Li, "Wideband time reversal of microwave signals based on phase conjugating," *Radioengineering*, vol. 27, pp. 1085–1091, 09 2018.

[19] R. Y. Miyamoto and T. Itoh, "Retrodirective arrays for wireless communications," *IEEE Microwave Magazine*, vol. 3, no. 1, pp. 71–79, 2002.

[20] T. Sasaki and N. Shinohara, "Study on multipath retrodirective for microwave power transmission," in *2018 IEEE Wireless Power Transfer Conference (WPTC)*, June 2018, pp. 1–4.

[21] "Witricity, technology overview," http://witricity.com/technology/, accessed: 2019-04-05.

[22] "How does cota work?" https://blog.ossia.com/how-does-cota-work, accessed: 2019-04-05.

[23] "Powercast, faq," https://www.powercastco.com/company/frequently-asked-questions/, accessed: 2019-04-05.

[24] "Ossia's Cota versus other wireless power technologies," Ossia, Tech. Rep., 2018.

[25] S. Lim, K. M. K. H. Leong, and T. Itoh, "Adaptive power controllable retrodirective array system for wireless sensor server applications," *IEEE Transactions on Microwave Theory and Techniques*, vol. 53, no. 12, pp. 3735–3743, Dec 2005.

[26] K. M. K. H. Leong, Yuanxun Wang, and T. Itoh, "A full duplex capable retrodirective array system for high-speed beam tracking and pointing applications," *IEEE Transactions on Microwave Theory and Techniques*, vol. 52, no. 5, pp. 1479–1489, May 2004.

[27] L. H. Hsieh, B. H. Strassner, S. J. Kokel, C. T. Rodenbeck, M. Y. Li, K. Chang, F. E. Little, G. D. Arndt, and P. H. Ngo, "Development of a retrodirective wireless microwave power transmission system," in *IEEE Antennas and Propagation Society International Symposium. Digest. Held in conjunction with: USNC/CNC/URSI North American Radio Sci. Meeting (Cat. No.03CH37450)*, vol. 2, June 2003, pp. 393–396 vol.2.

[28] D. M. Grimes and T. O. Jones, "Automotive radar: A brief review," *Proceedings of the IEEE*, vol. 62, no. 6, pp. 804–822, June 1974.

[29] T. O. Jones, D. M. Grimes, and R. A. Dork, "A critical review of radar as a predictive crash sensor," in *SAE Technical Paper*. SAE International, Feb.

1972. [Online]. Available: https://doi.org/10.4271/720424

[30] E. H. Dll and H. J. Peters, "Collision avoidance system for automobiles," *SAE Transactions*, vol. 87, pp. 1250–1260, 1978. [Online]. Available: http://www.jstor.org/stable/44611097

[31] H. H. Meinel, "Evolving automotive radar from the very beginnings into the future," in *The 8th European Conference on Antennas and Propagation (EuCAP 2014)*, April 2014, pp. 3107–3114.

[32] J. Wenger, "Automotive radar - status and perspectives," in *IEEE Compound Semiconductor Integrated Circuit Symposium, 2005. CSIC '05.*, Oct 2005, pp. 21–24.

[33] J. Hasch, E. Topak, R. Schnabel, T. Zwick, R. Weigel, and C. Waldschmidt, "Millimeter-wave technology for automotive radar sensors in the 77 ghz frequency band," *IEEE Transactions on Microwave Theory and Techniques*, vol. 60, no. 3, pp. 845–860, March 2012.

[34] J. Wenger, "Automotive mm-wave radar: status and trends in system design and technology," in *IEE Colloquium on Automotive Radar and Navigation Techniques (Ref. No. 1998/230)*, Feb 1998, pp. 1–7.

[35] S. M. Patole, M. Torlak, D. Wang, and M. Ali, "Automotive radars: A review of signal processing techniques," *IEEE Signal Processing Magazine*, vol. 34, no. 2, pp. 22–35, March 2017.

[36] C. Vaidyanathan and K. M. Buckley, "Performance analysis of the mvdr spatial spectrum estimator," *IEEE Transactions on Signal Processing*, vol. 43, no. 6, pp. 1427–1437, Jun 1995.

[37] R. Schmidt, "Multiple emitter location and signal parameter estimation," *IEEE Transactions on Antennas and Propagation*, vol. 34, no. 3, pp. 276–280, Mar 1986.

Chapter 2

Retrodirective Antenna Array (RDA) for Circularly Polarized Wireless Power Transmission

2.1 Introduction

The advancement of technology is exponential and a good proof of it can be found in Wireless Power Transmission (WPT). The aim pursued in this research deals with cutting the last wire between the power source and the device-under-charge (DUC) aiming for both flexible mobility and efficient power transfer. By definition, WPT is the transmission of electrical power from a source to a receiving device without any physical contact between them [1, 2]. Such a concept is illustrated in Fig. 2.1, where we can differentiate between a Reactive Near-Field (NF) (Fig. 2.1-a) and a Radiative NF and Far-Field (FF) wireless charger (Fig. 2.1-b). Moreover, different types of WPT systems can be classified regarding their frequency of operation. For example, microwave power transfer (MPT) is related to WPT systems that work at microwave frequencies, which is the focus of this chapter. Also, solar power harvesting and remote powering of unmanned aerial vehicles [3–5] are some of the other previously reported research activities on MPT.

One of the most basic WPT concepts is the resonant inductive coupler, which is a pair of coils having an exact diameter and number of turns for resonance at the

same frequency [6–9]. This concept is illustrated in Fig. 2.1-a, where the transmit base and the receiver device embody separate coils. In order to ensure that resonant inductive coupling occurs, both coils must be at a very close distance, within the reactive NF, and properly aligned (the better the alignment is, the better the power transfer will be) [10]. Such conditions make the positioning of the DUC a big limitation in terms of mobility if efficient power transfer is desired. Applications of this type of NF-WPT include wireless charging of mobile electronics [6,7], electrical vehicles [8], and biomedical devices [9].

The important limitation aforementioned, is overcome by the second type of WPT shown in Fig. 2.1-b, giving to the DUC the freedom to move at longer ranges, even in the FF, but paying the price of lower received power at the DUC which is caused by free space path loss (FSPL). More specifically, such technology that allows this is Retrodirective Antenna Arrays (RDAs), which follows from radar. Also, it has been discussed in the last chapter the other approaches that allow for WPT such as pure line-of-sight transmission (they don't allow for beam tracking), and recursive beamforming algorithms that optimize the transmitted beam for the highest energy transfer. However, the latter are more time consuming and complex. Also, employing RDAs for WPT is a very new topic (most of them have been previously used for communication purposes), as this thesis exploits the fact that RDAs can operate in any of the field regions; i.e. NF or FF [11–13], providing considerable advantages over the traditional resonant wireless chargers. Moreover, another feature apart from free-space mobility, is the added benefit of orientation flexibility by taking advantage of circularly polarized (CP) antennas as in this work, while also offering an improvement in the isolation given that opposite CP polarizations were used in the transmit and receive channels.

Some other works already use RDA technology for WPT, but with some differences with respect to the reported structure in this chapter. For example, in [14], a tracking system using digital beamforming was presented, while in [15] an RDA was also used as a transmitter to enable beam tracking capability, but such work was only focused on how to optimise the number of receiver rectennas that will maximise the overall efficiency and no complete microwave system results were reported. Additionally, apart from WPT, RDAs have been used in many different applications as found in the literature. Some of these include spatial encryption,

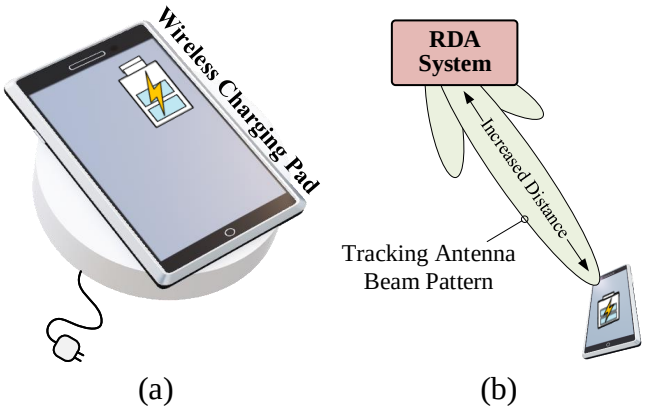

Figure 2.1: Conventional WPT illustrating (a) inductive coupling and (b) the proposed WPT approach using retrodirective antenna (RDA) technology where the device can be tracked and powered in free-space at a significant distance.

radar and microwave imaging [16].

In this chapter the design, fabrication and measurement of a novel RDA system is reported for NF or FF high-power WPT applications, exploiting the use of transmitting sub-arrays to reduce the number of active components needed in the system and therefore reducing the costs. A preliminary tracking study in the NF has also been done with very low transmit powers, using only 2 patch elements for simplicity and for understanding (and with no sub-arrays), given that most of the system characterization will be made in this region. In summary, the developed large scale RDA system (using sub-arrays) exhibits a high transmitted output power (36dBm) by re-amplifying the received beacon tone (6.6 dBm) for an angular range of $-50^o \leq \theta \leq 50^o$ thanks to its self-tracking capabilities. Also, the proposed RDA is rooted in the Pon structure [17] for frequency converted retrodirective operation but avoiding the use of circulators and having independent transmit and receive antennas. This can make the design more planar, low-cost and with less circuit elements for retrodirective operation. Finally, an alternative design based on the Van Atta architecture is proposed by using a novel dual-polarization 2×2 CP antenna array. This antenna array could also be used in a monopulse radar system.

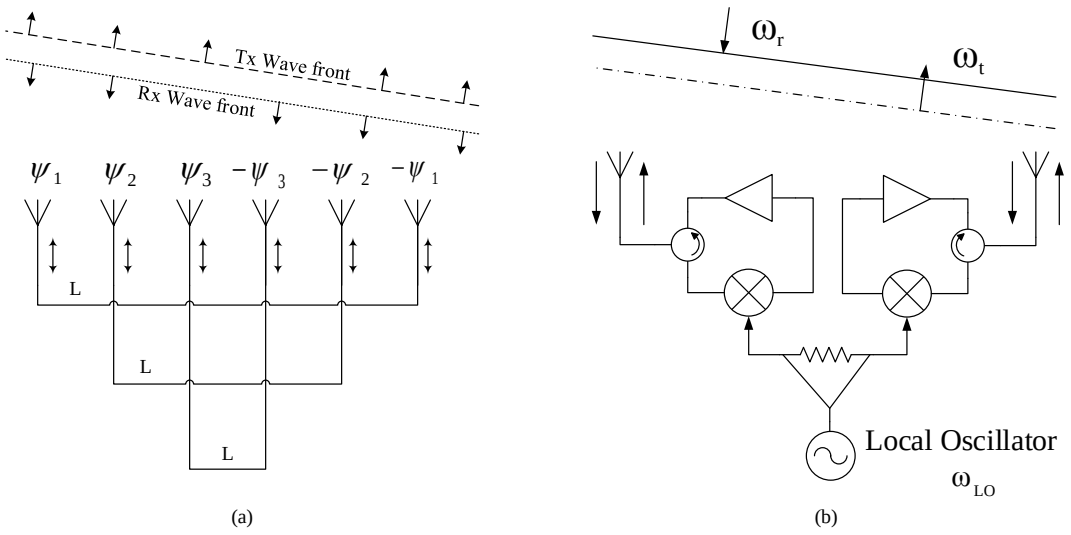

Figure 2.2: Classical Van Atta (a) and Pon (b) RDA structures.

2.2 RDAs and its applications into WPT

Classic RDAs can be defined as an array of transceivers that are able to track devices. Such devices send a beacon tone for tracking and by the relative phase difference received at each antenna element in the RDA (direction of arrival or DOA), re-radiation back to these devices is made possible [18] and without any previous knowledge of the device location. Moreover, these systems can track in any field region, from the radiative NF [11] to the very FF [13], making them very attractive for WPT applications. The use of high gain amplifiers are of vital importance to overcome the FSPL and still deliver power levels that are higher than the power transmitted initially by the beacon signal tone to enable a positive power balance at the DUC.

According to the topology, RDAs can be divided into two main subgroups: Van Atta [19] and Pon [17] structures. The passive Van Atta RDA is defined by an array of elements that are connected symmetrically and with a phase delay between connected pairs of 180^o, normally introduced in the same transmission lines as shown in Fig. 2.2(a), where L corresponds to the length of the transmission line that connects each of the antenna pairs and ψ_i is the progressive phase shift with respect to the previous element. Active Van Atta RDAs also require the use of additional components such as circulators and amplifiers or just bidirectional amplifiers [20]. This important disadvantage can make more conventional Van Atta RDA structures

costly and perhaps not suitable for WPT applications when considering low-cost implementation.

On the other hand, Pon structures use RF mixers to provide retrodirectivity by phase conjugation [16]. This principle is demonstrated by the trigonometric equivalence of the product between the two input signal tones or cosines [17], which are the RF input signal and the local oscillator signal (LO). Gain blocks or amplifiers are also of vital importance within each RDA element if the intended use is for WPT applications, in order to boost the retrodirected power. Even though more planar and low profile designs are generally preferred, spherical [21] and cylindrical [22] Pon RDA structures have been reported in the literature.

The most basic structure is the 2-element Pon-RDA, which is shown in Fig. 2.2(b). The underlying key concept that enables retrodirective operation in Pon-RDAs is the phase conjugation that happens by the RF mixers. The received beacon signal from the DUC at the antenna elements (ω_r) goes directly into the RF port of each mixer. It has to be mentioned that all the mixers share a common LO to ensure a consistent reference. For proper RDA operation, the received signal and the re-radiated one should be at the same frequency, fixing the local oscillator frequency to be two times the frequency of the input signal, this is $\omega_{LO} = 2\omega_{RF}$. In this manner, the output signal will be phase conjugated [17], thereby, an inverted progressive phase difference between antenna elements will be achieved, resulting in a wave-front with the same direction as the received one (ω_t). As this phenomena happens almost instantaneously, or in real-time; i.e. analog signal processing, tracking of the DUC is achieved based on the initial beacon signal. It must be noted that the LO port of the mixers needs to be totally synchronized to obtain a proper phase output on each element and hence proper retrodirective operation.

The expression that demonstrates phase conjugation for RF mixers is obtained as shown in equation (2.2.1).

$$v_{IF}(t) = V_{RF}\cos(\omega_{RF}t + \phi)V_{LO}\cos(\omega_{LO}t) = \\ = \frac{1}{2}V_{RF}V_{LO}(\cos((\omega_{LO} + \omega_{RF})t + \phi) + \cos((\omega_{LO} - \omega_{RF})t - \phi)) \tag{2.2.1}$$

where $v_{IF}(t)$ is the output signal of one of the mixers, V_{RF} and V_{LO} are the input and local oscillator signal amplitudes, respectively, and ϕ corresponds to the

instantaneous phase of the input signal. It is also shown in Eq. (2.2.2) that we get the third harmonic of the RF frequency (upconversion) and it should be filtered out from the output.

$$v_{IF}(t) = \frac{1}{2}V_{RF}V_{LO}(\cos(3\omega_{RF}t + \phi) + \cos(\omega_{RF}t - \phi)). \tag{2.2.2}$$

Such a case corresponds to a scenario with only one incident signal. However, in the case where multiple signals operating at the same frequency arrive to the RDA, the signal received is the total addition of the individual incident signals [23]. In this situation it can be difficult for the RDA to synthesize and re-radiate multiple beams simultaneously. Nevertheless, if the individual incident signals are slightly shifted in frequency to make them different but similar enough to be within the bandwidth of the array, the RDA can simultaneously respond to each individual signal (multi-beam) [23, 24]. Equations that include an input signal with a certain bandwidth (multi-tone) can be found in [25]. Also, the use of RDAs can be particularly advantageous in multipath environments. The principle reason for this is that the retrodirected signal from the RDA, automatically follows the same path as the transmitted signal, even when this path involves multiple reflections, that is, the RDA acts as a spatial temporal matched filter [16, 26, 27].

When developing and implementing a real RDA, some important isolation issues arise when transmit and receive frequencies are identical. Two important points can be identified, in terms of problematic isolation, when considering such common frequencies.

1. The circulator (see Fig. 2.2), whose isolation between non-consecutive ports can be in the range from 20 to 40 dB. And given that the gain of the amplifiers used in the proposed WPT system will also be around that range, we can identify that the retrodirected signal that couples back into the circuit system has a comparable amplitude to the one properly received from the beacon signal originated from the DUC, and therefore, this can cause some interference of the phase distribution that needs to be conjugated for RDA operation. Moreover, apart from altering the required phase, this feedback loop can overload the active components in the system (i.e. amplifiers and mixers) and can cause permanent damage. All this combined with the cost of circulators, as well as their bulkiness, make them not preferred when low-cost

and low-profile implementations are desired.

2. The mixers can also be problematic, because of their existing RF-to-IF leakage, referred to the signal that leaks through from their input port (RF) to their output port (IF), causing the addition of this signal with the mixed one and leading, then, to possible squinting of the direction of the retrodirected beam [28].

One way to perhaps solve this problem, instead of having identical transmit and receive frequencies, they can be slightly different by making the LO tone approximately twice the input frequency ($\omega_{LO} \approx 2\omega_{RF}$) [16].

The spacing between antenna elements also has to be considered, given that side-lobe-level (SLL) increases as the spacing increases. To avoid this, it is preferable to ensure $d \leq \lambda/2$, where d is the distance between radiating elements.

2.3 Discussions of Pon and Van Atta RDAs Working in the NF; preliminary Pon prototype

Initial estimations for the RDA aperture size required to achieve the desired power to be received in the DUC at a given distance, demonstrate that the RDA system will potentially be operating in the NF region. Hence, in order to have some initial confidence that the RDA system will be able to work in the NF as required, an RDA system with lower gain and reduced cost using FR4 material, as well as a simpler antenna design (i.e. two CP patches at transmit and receive) has been built as shown in Fig. 2.3. Transmit and receive antennas within the same chain are collocated for proper RDA operation. Therefore, the tracking plane is perpendicular to the plane containing the antenna Tx and Rx pairs. Thus, each chain, as it can be seen from Fig. 2.3(b), is composed by (in order): Rx Antenna, mixer, driver amplifier, power amplifier and tx antenna.

It should be mentioned that in [29], an analysis and performance comparison between two different RDA topologies operating in the NF were reported. The Pon and Van Atta RDA topologies under study are shown in Fig. 2.4. The main difference between both structures lies in the fact that in the Van Atta array, one

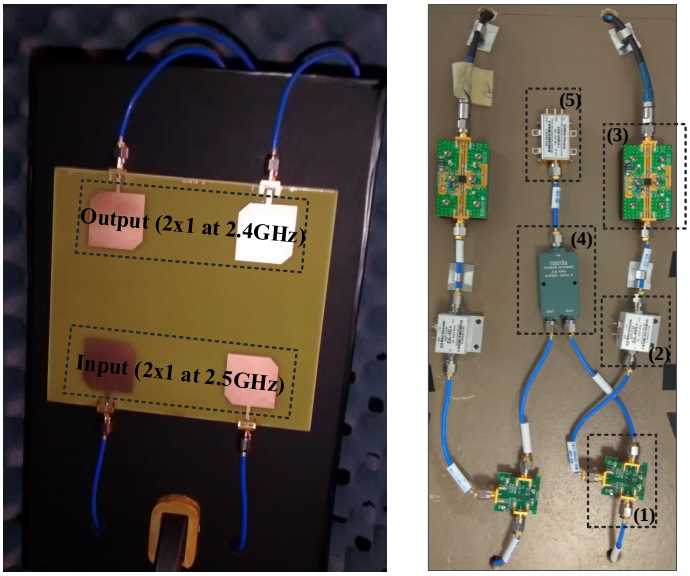

Figure 2.3: Picture of the preliminary Pon RDA prototype built for initial *proof of concept* measurements. Receive and transmit antenna arrays (a) and RF components (b), including mixers (1), amplifiers (2 and 3), power divider (4) and VCO (5).

antenna receives the signal and its pair will retrodirect the signal back to the same direction that the incoming wavefront came from. The heterodyne or Pon array, conversely, receives and retrodirects the signal back with the same antenna element. The radiating element in this structure is a two port dual-pol antenna, using one of the ports to receive in one polarisation and the other one to transmit in the opposite polarisation to achieve an optimal Tx-Rx isolation. This difference between both topologies will be further explained below, in terms of the relevant NF performances.

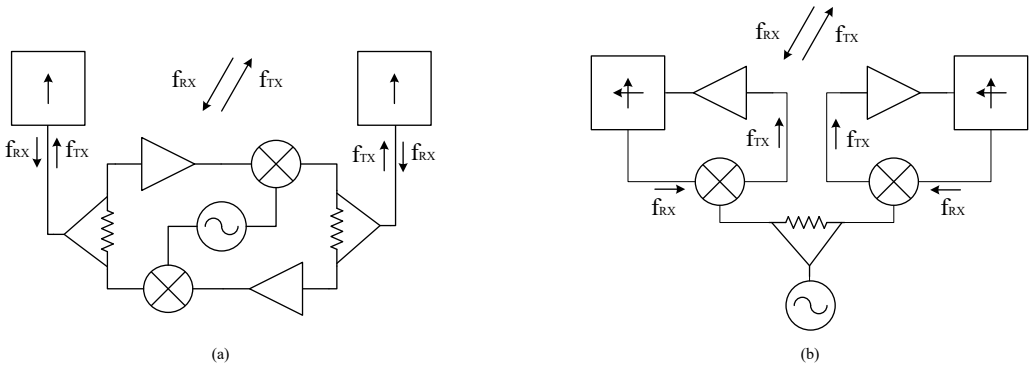

Figure 2.4: LP Van Atta (a) and Dual-Pol Pon (b) structures discussed in [29].

According to [29], the Van Atta array may be more suitable for NF operation

rather than the Pon array because of the propagation path lengths that the signal will need to travel, from the initial beacon to the retrodirected signal back to the origin of the beacon. Moreover, this propagation path will be the same regardless the array element considered as shown in Fig. 2.5. Assuming that the mobile is in the NF region, the contribution of each of the antenna elements within the RDA will be different at any specific angle, except broadside, as the field F1 and F2 shows in Fig. 2.5, which are the field pattern strength at the angle defined by the line-of-sight between the antenna and the DUC antenna. This behaviour is complemented with simulations as shown in Figs. 2.7 and 2.8 following the arrangement set in Fig. 2.6. However, for its use in WPT at which power levels are much higher, Van Atta structure might not be suitable due to its weak isolation between crossed paths, causing unwanted and dangerous feedback loops that could damage the active components as well as phase noise, being such factor determinant in the pointing beam precision. For such a reason, a study of the performance in the near-field of the frequency offset heterodyne RDA (Pon RDA) has been done.

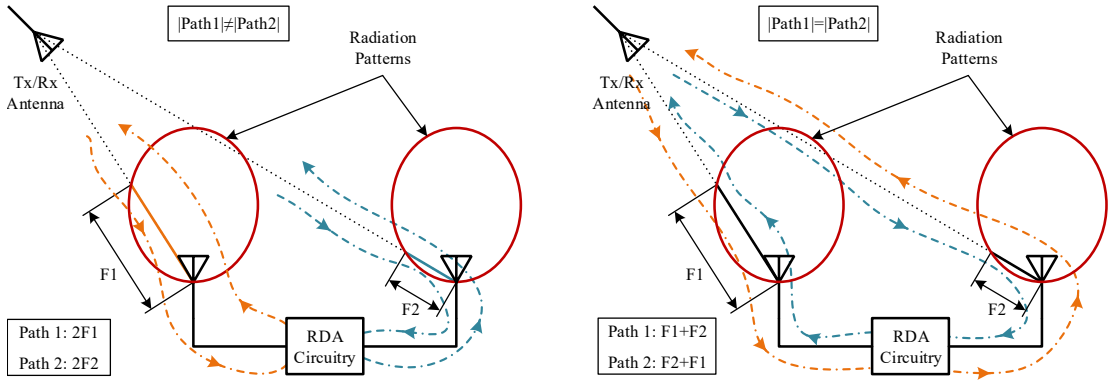

(a) Frequency offset heterodyne RDA

(b) Frequency offset Van Atta RDA

Figure 2.5: Effect of path loss and element patterns in a Pon (a) and Van Atta (b) structures.

Two sets of measurements have been performed at 10 cm and 25 cm, in the reactive and radiative NF regions, respectively. The expressions that defines the boundaries between each field region [30] are:

$$R_1 = \sqrt{\frac{D^3}{\lambda}} \tag{2.3.1}$$

$$R_2 = \frac{2D^2}{\lambda}$$

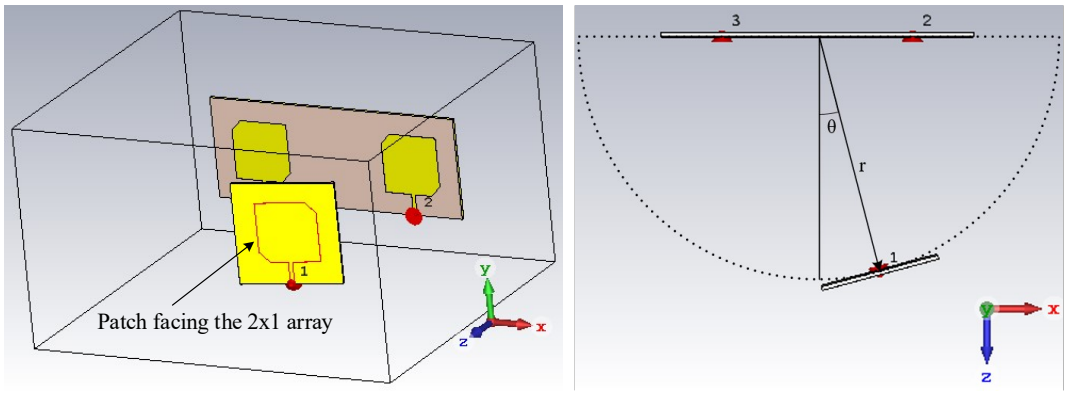

(a) (b)

Figure 2.6: Simulation setup: (a) Perspective and (b) top views.

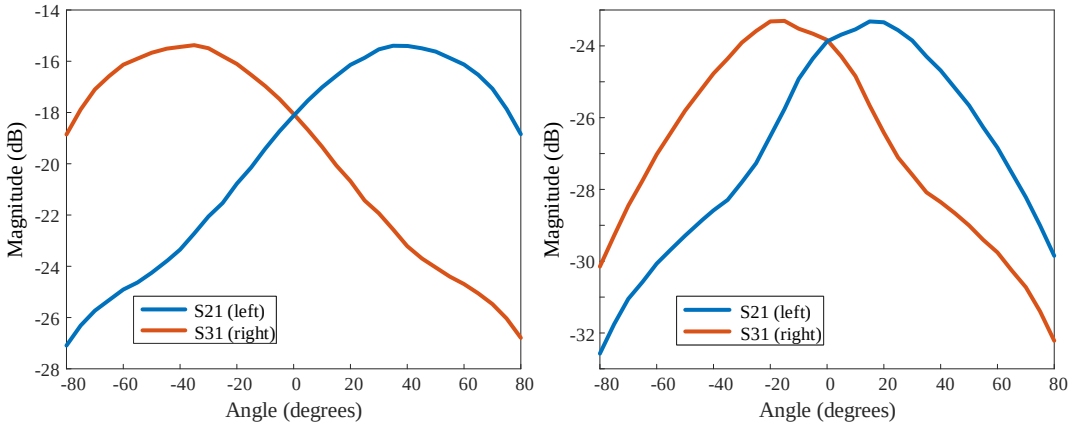

(a) (b)

Figure 2.7: Simulations of the contribution of each antenna element regarding the position (angle) of the Tx/Rx element; (a) Reactive NF at 10cm and (b) Radiative NF at 25cm.

being R_1 the boundary distance between the reactive and radiative NF regions and R_2 the boundary between the radiative NF and the FF regions; D is the maximum linear dimension of the antenna array and λ is the wavelength in free-space.

Fig. 2.7 represents the transmission coefficients from the initial transmitting antenna to the RDA. From there it can be seen that the closer we are to the FF, the contribution of both RDA antennas starts to be very similar. Conversely, at very close distances (i.e. the reactive NF) the left antenna will dominate in terms of received field strength in the negative angles, whereas the right antenna will dominate in the positive ones. This effect is translated into a flat pattern, as it is shown in the red line from Fig. 2.8, where both contributions are added to obtain the shape of the received pattern in the RDA. However, the shorter the distance to

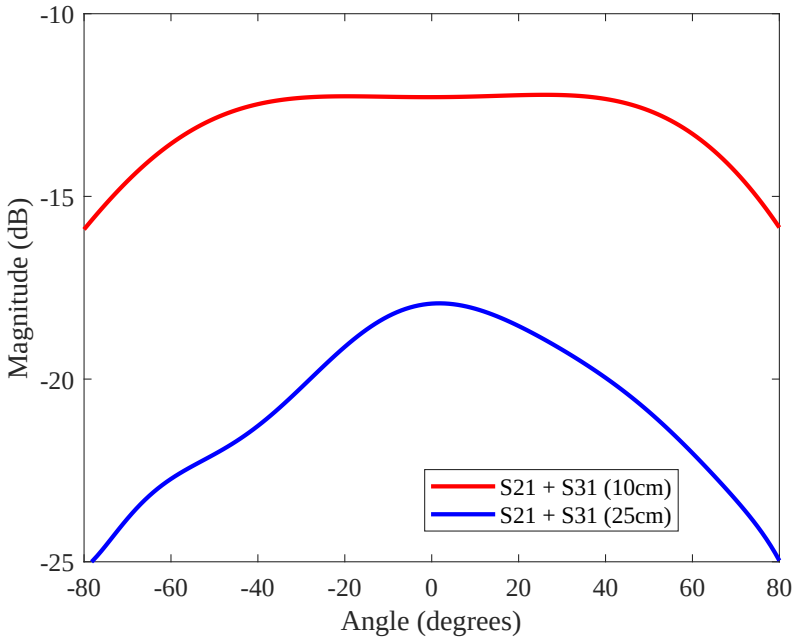

Figure 2.8: Addition of the transmission coefficients from Fig. 2.7.

the RDA, will make the pattern maximums to be further apart and, by consequence, the intersection between them will be so low that its addition will not be enough to result in a flat pattern, so a null will start appearing at broadside [29] (see Fig.2.9).

The simulations shown in Fig. 2.8 and the study from [29] is confirmed with measurements in Fig. 2.9(b), where a reduction in the retrodirected power occurs at angles close to broadside for the shortest distance between the RDA and the DUC.

Results of the bistatic measurements can be found in Fig. 2.10 for the reactive, radiative NF and FF, respectively. It can be noticed in the figure that the tracking capabilities of the proposed design are in agreement between the simulations and measurements. Additionally, bistatic measurements at 10 and 25 cm have been made and compared in this case to simulations in Figs. 2.11 and 2.12. In Fig. 2.11, it can be observed that the measurements and simulations have a similar field pattern. Despite the difficulties to make the measurements with high accuracy (since the mechanical supports were very close together at Tx and Rx), the shape of the measured points follows the expected trend of the main beam and also each of the nulls. On the other hand, for the radiative NF case (Fig. 2.12), the measured points match very well to that of the expected pattern shape. Therefore, the RDA is expected to track better in the radiative NF region than in the reactive one, but

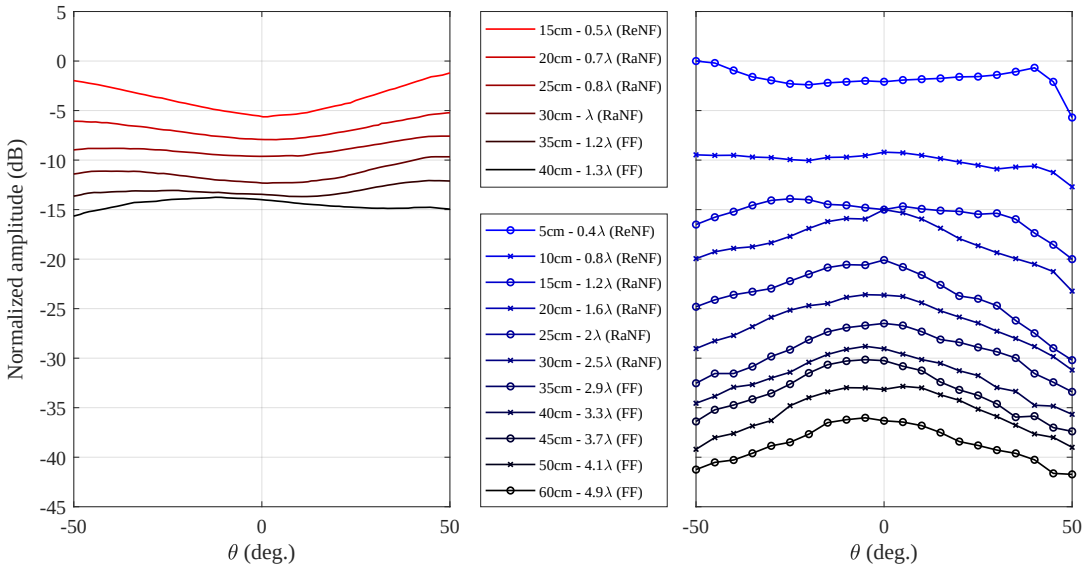

Figure 2.9: Monostatic measurements in the reactive and radiative NF at different distances. Pon RDA from [29] (left), and proposed Pon RDA (right).

still showing that tracking is possible in any of the two regions.

The power received at broadside at different distances has also been measured as shown in Fig. 2.13. The expression obtained from [31] for the path loss is valid either for the NF and the FF, which is:

$$P(d,f) = \frac{G_{TX}G_{RX}}{4}\left(\frac{1}{(kd)^2} - \frac{1}{(kd)^4} + \frac{1}{(kd)^6}\right) \tag{2.3.2}$$

being G_{TX} the gain of the transmitter, G_{RX} the gain in reception, k the wavenumber and d the distance between them. The measured received power follows nicely the trend for the free-space path loss model; i.e. Eq. 2.3.2 [31]. However, there is no agreement with the indoor propagation model [32] which takes into consideration multipath effects. Such disagreement is justified in the fact that the measurements were made inside an anechoic chamber, replicating a free-space environment.

In summary, it has been demonstrated with measurements and simulations that the selection of a Pon RDA follows well theory, measurements, and simulations. In the next section, other considerations about this topology will be discussed.

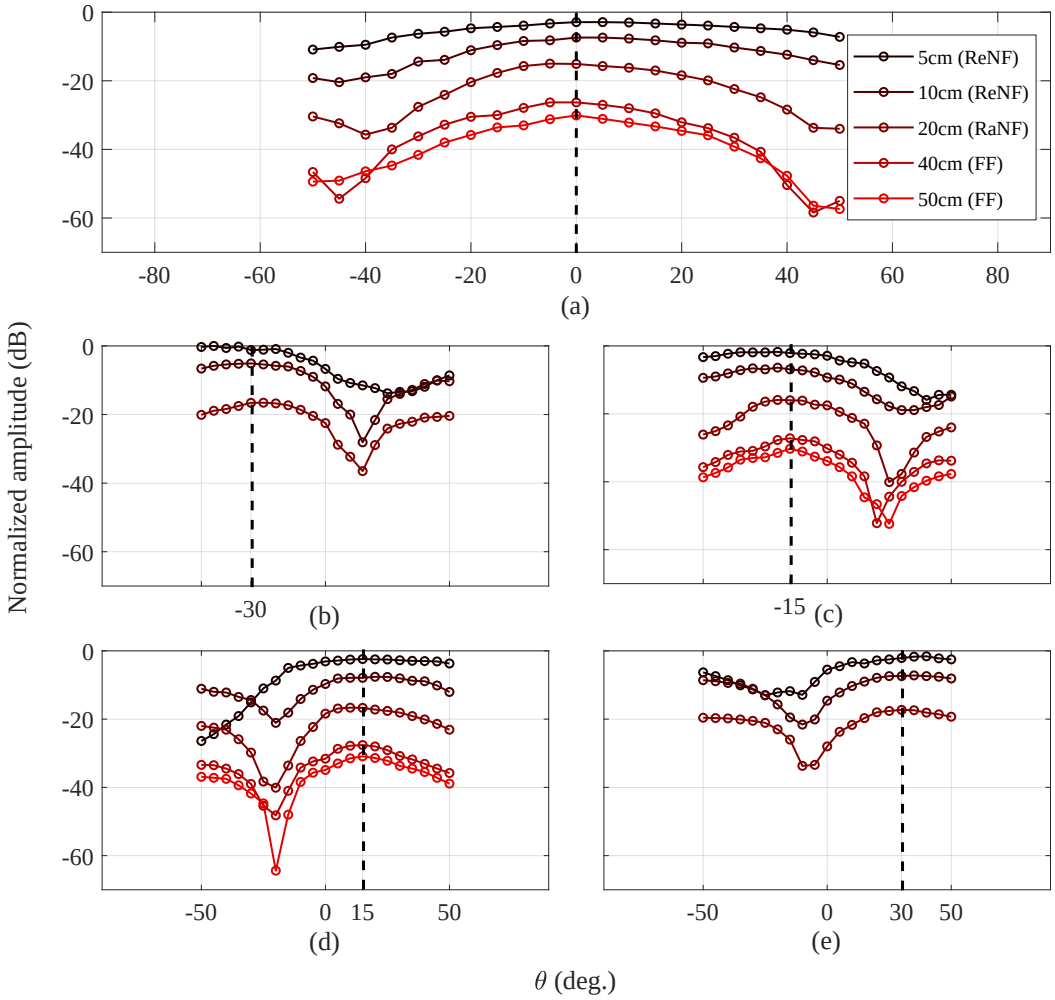

Figure 2.10: Bistatic measurements in the reactive and radiative NF at different angles and distances for the proposed RDA: 0° (a), −30° (b), −15° (c), 15° (d), and 30° (e).

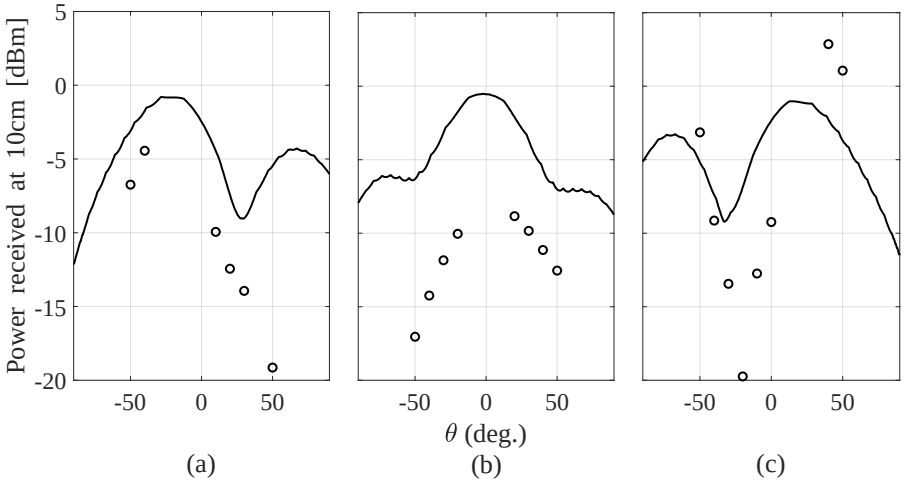

Figure 2.11: Bistatic measurements (circles) and simulations (continuous line) in the reactive NF for a 10 cm range from the RDA: at −20° (a), 0° (b), and 20° (c).

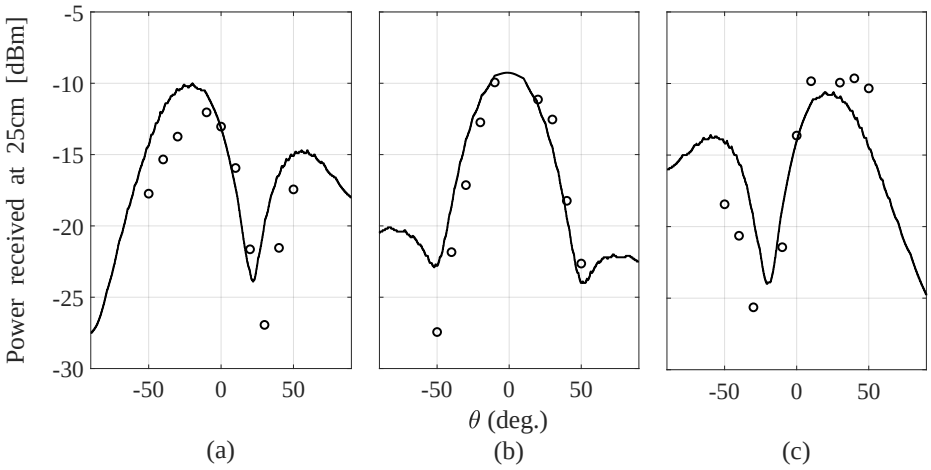

Figure 2.12: Bistatic measurements (circles) and simulations (continuous line) in the radiative NF for a 25 cm distance from the RDA: at $-20°$ (a), $0°$ (b) and $20°$ (c).

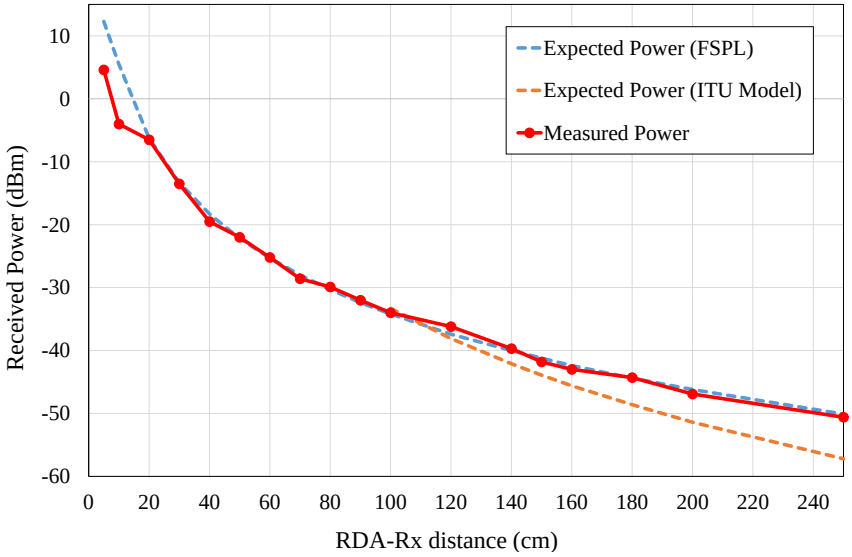

Figure 2.13: Measured received power at different distances from the RDA (broadside) in comparison with the theoretical expected power, the free-space path loss model (FSPL) and the indoor propagation model (P.1238-8).

2.4 Pon RDA Design Considerations; new Pon RDA using Subarrays

What is more challenging when targeting WPT applications in the design of RDAs, is to maintain high levels of received power at the DUC. The total gain of the amplifiers included in the system must compensate for the FSPL while also having an extra amount of gain that enables wireless charging at the DUC. This translates into additional costs given that amplifiers are present on each of the antenna ele-

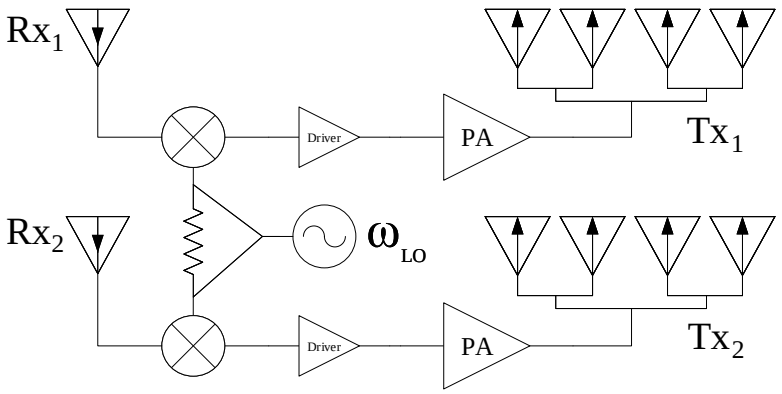

Figure 2.14: Modified Classical Pon RDA structure (showing two RF chains) by removing circulators, using independent transmit and receive antennas and sub-arrays in transmit.

ments that defines the system. Moreover, the same amount of mixers are required increasing the cost even more.

In this section, a new approach is proposed in order to maintain high received power levels while maintaining reasonable costs following a design approach which considers polarization, isolation and reduced circuit complexity. This approach, as shown in Fig. 2.14, has some characteristics that differentiates it from the classical Pon RDA (Fig. 2.15). There are four main concepts and they are described as follows:

1. *The removal of circulators.* By removing these bulky and expensive electronic components (used for isolation between transmit and receive signal paths), the system becomes more planar and low-cost. Moreover, removing the circulators forces the design of independent transmit and receive antennas. If compared to the case where the same radiating element acted as a transmit and receive antenna, isolation can be further improved by designing independent antennas such that they operate at the transmit or receive frequency minimizing electromagnetic coupling between antenna elements.

2. *The use of transmit sub-arrays for the RDA* (see Fig. 2.15(b)). This will boost the transmit gain and also remove the need for a mixer amplifier pair for each antenna. This will reduce the number of active elements considerably, thus reducing circuit costs. However, the trade-off of this is the reduction of the

beam-tracking capability to just one plane ($\phi = 90^o$) as illustrated in Fig. 2.15(b).

3. *Circular polarization (CP)* brings another advantage over more classic approaches. Using CP on both transmit and receive signals gives orientation flexibility in the DUC avoiding any potential polarization mismatches caused by misalignment between the DUC and the RDA.

4. Improvement of the isolation between transmit and receive paths by *using orthogonal polarisations*. The initial transmitted beacon is right-hand circularly polarized (RHCP), whereas the retrodirected beam exhibits left-hand circularly polarization (LHCP). Such a configuration can avoid problems regarding the interference that might exist when the pilot beacon is received in the transmitting antenna of the RDA. It also reduces possible coupling between transmit and receive antennas at the DUC and at the RDA.

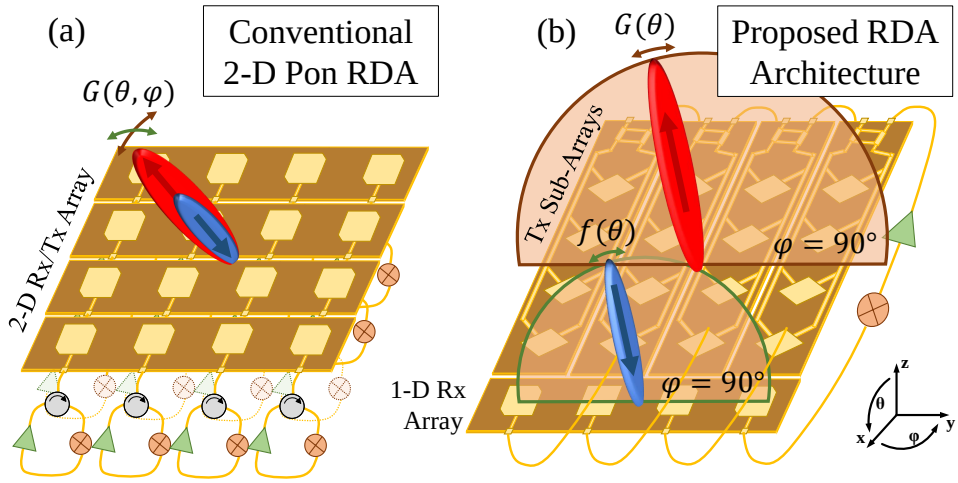

Figure 2.15: Comparison of a conventional CP-RDA, (a), defined by a 2-D planar array of corner-clipped patches and heterodyne mixing (i.e. a Pon architecture where RF amplifiers, circulators and mixers are required at each antenna element) to the proposed RDA, (b), for WPT applications. In both cases, a total of 16-elements (4×4) are shown for the transmitting part of the RDA.

2.4.1 Considerations for Cost and Performance

One of the most important engineering processes that are undertaken in the design of any system is the compromise between cost and performance. More specifically, the RDA system for WPT is a clear example of this. According to the tracking

capabilities of an RDA, they can be sub-divided into two groups: linear RDAs and 2-D RDAs. Linear RDAs (see Fig. 2.16(a)) are referred to those of which antenna elements are distributed in a straight line, and therefore, the phase distribution of the received signal is only in one dimension. The outcome of this is the ability of beam tracking in just the plane containing the antenna elements. On the other hand, planar RDAs (see Fig. 2.16(b)) are those of which antenna elements are distributed in a rectangular matrix, and therefore, the phase distribution of the received signal has two dimensions, allowing the system to track in 3-D space. However, the price to pay in this scenario is much higher in terms of cost (see Table 2.1), given that amplifiers and mixers are required at each antenna element [33]. Depending on the positioning of the DUC one approach would be more suitable than the other. If the DUC moves freely in 3-D space it is obvious that the planar 2-D RDA approach would be more convenient. However, if the DUC moves most of the time along the tracking plane, the linear RDA may be preferred.

It should be mentioned that in Table 2.1, *Array Size* corresponds to the size of the separated receiving and transmitting arrays of the RDA given that this comparison is made for RDAs that do not use circulators as shown in Fig. 2.15(b). The reported values were obtained by considering the simulated realized gain of an individual patch antenna, employed in the proposed design, computed with the array factor for a $\lambda_0/2$ separation between antennas at 2.4/2.5 GHz. Also, *Normalized Performance* in Table 2.1 corresponds to the received RF power at the DUC for a 0.5 m distance between the RDA and the DUC, and normalized, with respect the 2×1 RDA case. Also, the unit value for *Normalized Performance* is 20 mW (13 dBm) and the design goal for our work corresponds to 27 dBm (or a *Normalized Performance* of 15). Moreover, the gains and losses of the active components to compute the overall performance for each of the cases was obtained from the datasheets of the employed circuit components. And finally, *Normalized Cost*, refers to the total cost of the active components needed for each case and normalized with respect to the cost of a reference 2×1 RDA.

This is where the benefits of the proposed sub-array (see Fig. 2.17) can be more appreciated; i.e. when seeking a balance between performance and cost. It is well known that the majority of the cost of the system is related to the active devices (i.e.

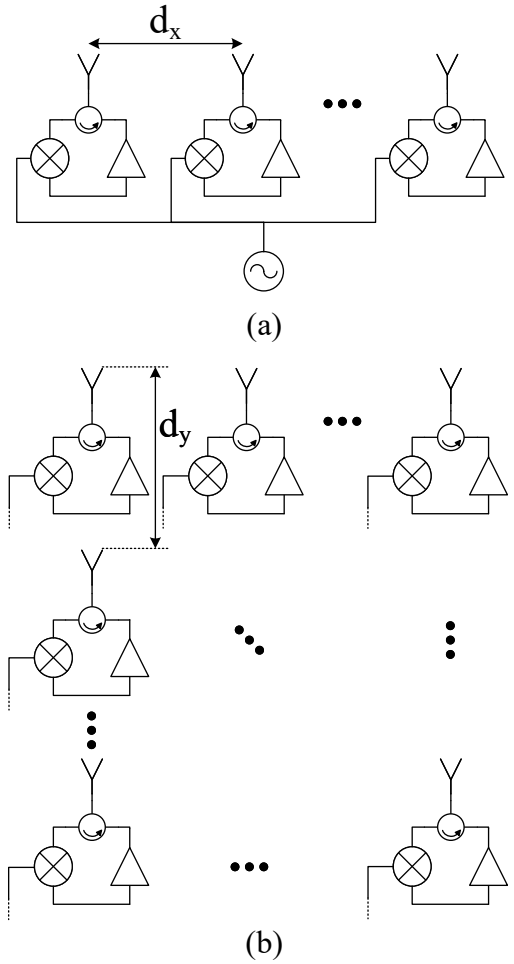

Figure 2.16: Classic 2-D Pon RDA defining an $M \times N$ square array with active circuit elements. Circulators, mixers, and amplifiers are represented at each element.

mixers, amplifiers), making non-viable the development of a planar array in cases where the cost is a limitation. To circumvent this issue, a valid solution would be to use a hybrid between linear and a planar 2-D structure. This is shown in Figure 2.17, where a linear array is proposed with the addition of sub-array elements instead of one radiating element per chain. This arrangement, considered as a linear RDA, will track only in one dimension, but at the same time will reduce the costs almost 4 times in a 4-by-4 system (see Table 2.1).

In Table 2.1, *Array Size* corresponds to the size of the separated receiving and transmitting arrays of the RDA given that this comparison is made for RDAs that do not use circulators as shown in Fig. 2.15(b). The reported values were obtained by considering the simulated realized gain of an individual patch antenna, employed in the proposed design, computed with the array factor for a $\lambda_0/2$ separation between antennas at 2.4/2.5 GHz. Additionally, *Normalized Performance* in Table 2.1

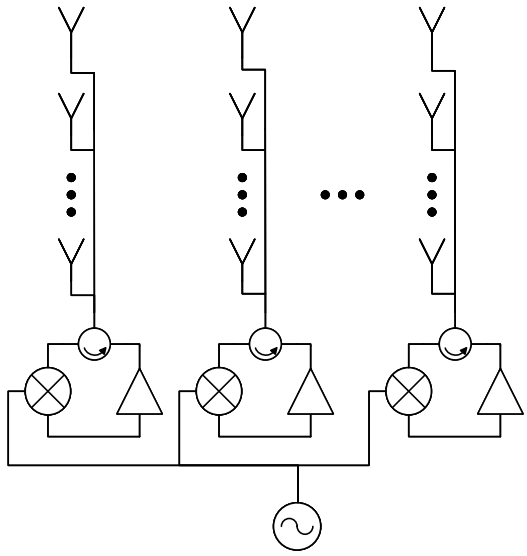

Figure 2.17: Schematic of a classic Pon RDA which uses a series-fed array of antenna elements per each mixer, increasing the overall gain if compared with the classic linear Pon RDA.

corresponds to the received RF power at the DUC for a 0.5 m distance between the RDA and the DUC, and normalized, with respect the 2×1 (IN and OUT) RDA. Also, the unit value for Norm. Perf is 20 mW. It should also be mentioned that our design goal corresponds to 27 dBm (or Norm. Perf. = 15). Moreover, the gains and losses of the active components needed to compute the overall performance for each of the cases was obtained from the datasheets of the employed circuit components (see Fig. 2.19). And finally, *Normalized Cost* refers to the total cost of the active components needed for each case and normalized with respect the 2×1 (IN and OUT) RDA, where the unit value for Norm. Cost is £1300.

Following array theory [30], the phase distribution of a scanning array can be

Table 2.1: Received RF Power and Cost Versus RDA Size

RDA Array Size (IN / OUT)	Normalized Performance	Normalized Cost
2×1 / 2×1	1	1
2×2 / 2×2	4.4	1.9
2×3 / 2×3	9.7	2.7
2×4 / 2×4	17.1	3.5
4×4 / 4×4	66.7	6.9
Proposed work (4×1 / 4×4)	16.7	1.8

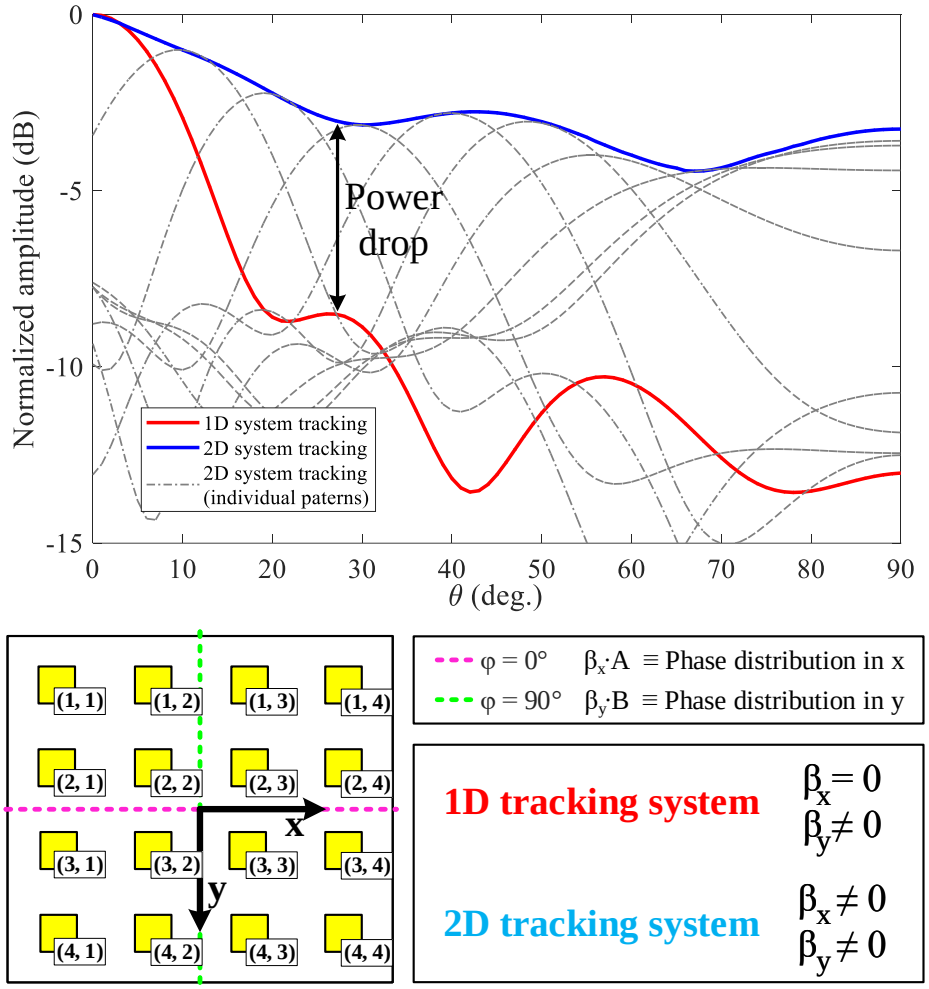

Figure 2.18: Performance comparison at $\phi = 90^o$ (in terms of power lost) between a 1-D and a 2-D tracking system.

defined by

$$\Psi_x = \beta_x A; \quad \Psi_y = \beta_y B$$

where A and B are coefficient matrices

$$A[i,j] = \begin{bmatrix} 0 & 1 & 2 & 3 \\ 0 & 1 & 2 & 3 \\ 0 & 1 & 2 & 3 \\ 0 & 1 & 2 & 3 \end{bmatrix} \quad B[i,j] = \begin{bmatrix} 0 & 0 & 0 & 0 \\ 1 & 1 & 1 & 1 \\ 2 & 2 & 2 & 2 \\ 3 & 3 & 3 & 3 \end{bmatrix}$$

and β_x and β_y are the progressive phase difference between the elements. It has to be mentioned that for the proposed array $\beta_x = 0$ because elements from the same row are connected together. For example, elements from (1,1) to (1,4) are connected in series conforming the first sub-array; from (2,1) to (2,4) are connected in series conforming the second sub-array, and so on.

The power loss impact when using a linear array rather than a planar array is compared in Fig. 2.18 for a 4×4 transmit array system. The aim of this study is to compare the power loss of the proposed design with a classic planar 2-D RDA along the non-tracking plane ($\phi = 0^o$), as illustrated in Figs. 2.15(b) and 2.18. The dimensions of the transmitting arrays are 4×4, employing the square patches used for the final design and spaced $\lambda/2$, as already mentioned in the cost study for table 2.1. In the graph from Fig. 2.18, the red solid line represents the normalised gain of the transmitting array (of the RDA) for each position of the DUC from 0° to 90° along the non-tracking plane ($\phi = 0^o$). As it can be seen, the normalised pattern will stay fixed with its maxima pointing at broadside. Conversely, for the planar 2-D RDA, the tracking is still occurring in that plane as it is shown in the solid blue line since power levels for planar RDA systems are higher than the linear ones. This solid blue line represents all the maximums of each of the patterns conformed by the planar RDA for each position of the DUC (some of the individual patterns are shown in grey dashed lines).

The distance between the two traces, represents the power drop in the non-tracking plane of the proposed RDA in comparison with a planar RDA. From this, depending on how critical the loss of power is, in terms of cost and the application, the proposed system may be preferred. This is because the proposed RDA maintains consistent power values at angles close to broadside. Also, power degradation of only about 5 dB are observed from broadside to $\theta = 30°$. In terms of cost, the planar RDA exhibits full tracking and higher received power, but is almost 4 times the cost of the proposed design (6.9 versus 1.8 of normalised cost), as it is shown in Table 2.1.

2.4.2 Details of the Developed RDA Design

The proposed design is illustrated in Fig. 2.15(a) and the measured prototype is shown in Fig. 2.19(a-b). It is defined by a 4×1 input and a 4×4 output array at 2.5 GHz and 2.4 GHz, respectively. Additionally, the output array is divided in 4×1 sized sub-arrays at each chain (see Fig. 2.19(c)). The removal of circulators involves the use of independent antennas for transmit and receive improving, therefore, isolation. Moreover, the proposed system has been designed to use orthogonal polarisations to increase even more isolation (RHCP for receive and LHCP for transmit) and CP to bring flexible mobility in the positioning of the DUC which is crucial

considering the intended application of mobile charging of commercial electronics.

Ideally the frequency applied to the LO ports within the RDA should be twice the input frequency. However, as it was already mentioned in section 2.2, one important issue that needs to be overcome is the RF-to-IF leakage in the mixers that can cause potential phase noise at the output and, consequently, leading to an associated small beam squint. To circumvent this, there is a small frequency shift in the LO port so the input and output frequencies are slightly different. In our case, the frequencies chosen are located in the ISM band and more specifically in the S-band: firstly, because these frequencies are free to use and secondly because at these frequencies the FSPL is not very high if compared to higher frequencies. The input (RF) frequency is 2.5 GHz, the LO frequency is 4.9 GHz (instead of the theoretical 5 GHz) and the IF frequency therefore is 2.4 GHz, considering that mixers

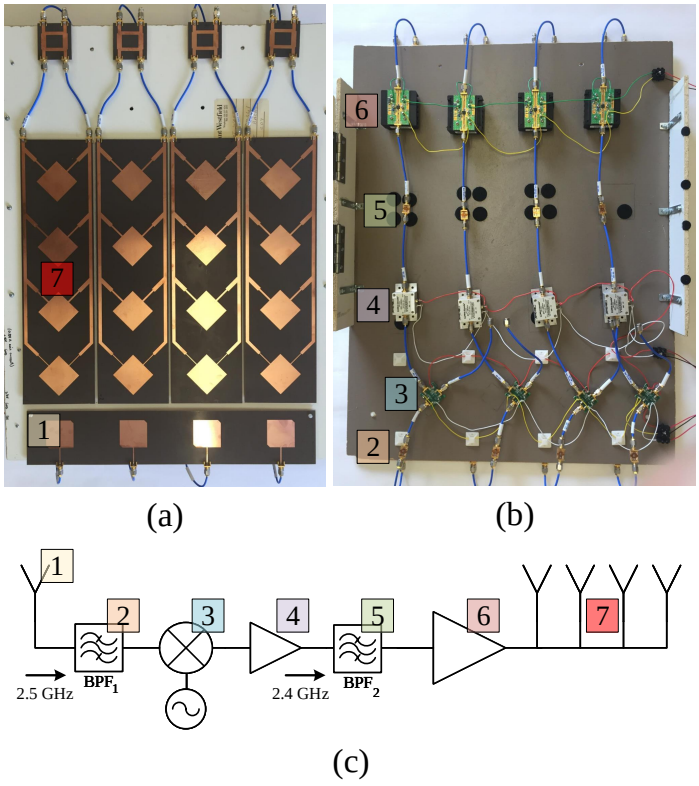

Figure 2.19: Picture of the proposed RDA system. Front (a), back (b) and schematic of one of the four RF chains (c). The components used in the system are: (1) receive 4×1 antenna array, (2) Band Pass Filter from TriQuint 885009 at 2.5 GHz, (3) Mixer from Linear Technology, (4) Driver Amplifier from MiniCircuits ZFL-2500+, (5) Band Pass Filter from TriQuint 885017 at 2.4 GHz, (6) Power Amplifier from TriQuint TQP9111 and (7) transmit 4×4 antenna array.

are working in downconverting mode.

Once phase conjugation has taken place, the signal is ready to be re-radiated back through the transmitting array, so a gain block is installed between the mixers and the array. This high gain block is composed of a driver amplifier and a power amplifier as illustrated in Fig. 2.19(c), being the latter in saturation.

2.4.2.1 Antennas within the Developed RDA

The design of the transmit and receive antenna arrays has been made using Taconic TLY-5 substrate, having a dielectric constant of $\epsilon_r = 2.2$ and a thickness of $h = 1.57\,\text{mm}$. The transmit array, shown in Fig. 2.19(a) element #7, has a series-fed network, as in [34], that connects consecutive patches in columns and with a distance between them of λ, so that they are totally in phase. The amplitude distribution for each element is about $1/2, 1/4, 1/8, 1/8$, of the input power; i.e. approximately 3dB is diverted to each patch. This type of feeding network is preferred over the more conventional corporate style due to the space limitations that require a more compact arrangement to reduce the side-lobe-level (SLL). For the variation of the input impedance on each patch, two independent $\lambda/4$ impedance transformers are placed between the feed lines and the patch. This feeding network is composed of two branches that will feed the orthogonal modes at the adjacent edges of the square patches. Hybrid couplers are connected right before the sub-arrays, in order to apply a phase offset of 90° to each branch to ensure CP operation. Moreover, with the hybrids the transmit polarization can be switched by driving one port or the other, terminating with a $50\,\Omega$ load for the isolated port. In the proposed system, the polarization sense of the 4×4 transmit array is left-hand (LHCP), whereas the 4×1 receive array is righ-hand (RHCP). For the latter, one port per patch and truncated corners on one of the two diagonals has been chosen to ensure CP operation.

Simulated and measured S-Parameters for one of the four 4×1 transmit sub-arrays and the 4×1 receive array are shown in Fig. 2.20(a) and (b), respectively. It can be observed that there is a good agreement between simulations and measurements. For the transmit sub-array, in Fig. 2.20(a), the measured coupling between ports (i.e. $|S_{21}|$) at the transmit frequency ($2.4\,\text{GHz}$) is slightly above the simulations but still below $-20\,\text{dB}$. There is a strong resonant peak around $2.5\,\text{GHz}$ caused

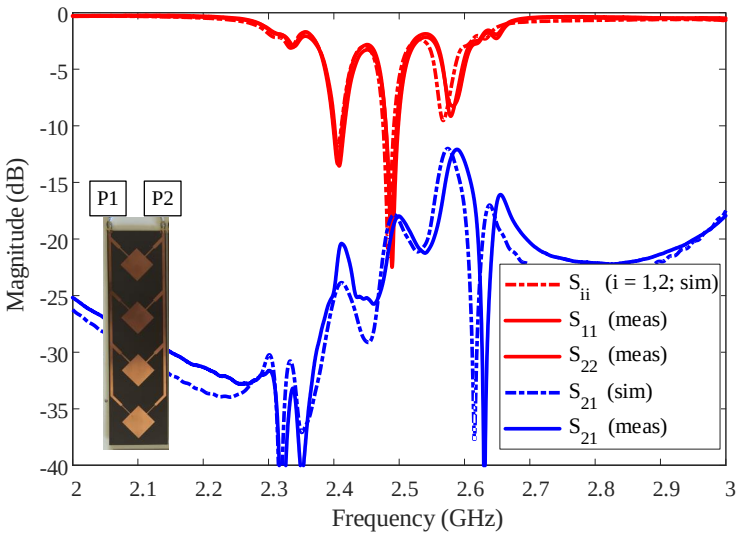

(a)

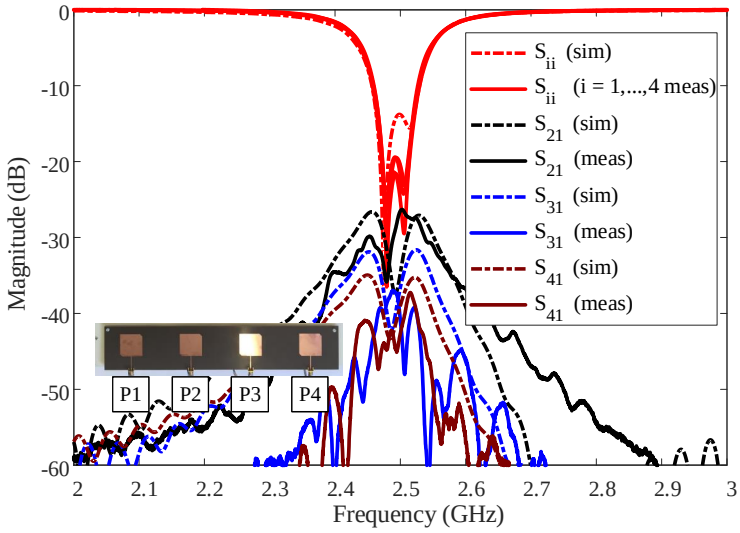

(b)

Figure 2.20: S-Parameters of the 4-by-4 transmit (one sub-array) (a) and 4-by-1 receive (b) arrays within the proposed RDA for operation at 2.4 GHz and 2.5 GHz respectively.

by the spurious feed radiation, which is due to the conventional unbalanced dual-orthogonal feeds used [35]. Nevertheless, any problem that this resonance could cause, is fixed by the sencond BPF in the chain. On the other hand, for the receive array (see Fig. 2.20(b)), there is a very good agreement between the simulations and measurements. The low bandwidth of the patch antenna acts in some way as a BPF itself, accepting the receive signal at 2.5 GHz, while it rejects any 2.4 GHz signal that would be present due to electromagnetic coupling. Additionally, the coupling between the receiving patch antennas is below −25 dB at the operating frequency.

2.4.2.2 Filtering Requirements

The frequency small difference between transmit and receive operational frequencies for the antennas within the RDA can cause coupling problems. This can cause an unwanted and positive feedback loop which can cause permanent damage to the RF active components as further described in this Section. Therefore, bandpass filters are of vital importance in the proposed system. Firstly, in order to filter out any of the retrodirected 2.4 GHz signal that has been coupled back into the system, a band-pass-filter (BPF) *885009* from Triquint that has low insertion losses at 2.5 GHz and high rejection at 2.4 GHz is connected in between the receive antennas and the mixers, as shown in Fig2.19(c), in element #2. Also, as it was previously mentioned, the mixers can leak some of the RF input signal to the mixer output. This signal has not been mixed to the RDA transmitting frequency and, if coupled back, it would not be rejected by the 2.5 GHz BPF given that the frequency is the same as the expected one from the beacon tone. This causes two important issues. Firstly, there would be two 2.5 GHz signals which would cause a beam pointing error. And secondly, the coupled signal can cause an unstable feedback loop. Therefore, an additional BPF (*885017* from Triquint) was introduced between the mixers and the transmitting antenna arrays, as shown in Fig2.19(c) (in element #5). This BPF accepts any 2.4 GHz signal while it rejects any 2.5 GHz signal. The filters used have been mounted on a Taconic substrate in CPW technology given the arrangement of the pins. Moreover, due to the very small dimensions of the commercial filters (9 mm^2 and 1.7 mm^2, respectively), the assembly of the filters has been made with the aid of the *LPKF Protoplace S* (a semi-automatic pick & place system for professional assembling of SMT printed circuit board prototypes). Pin connections and the connectorized filters are shown in Fig. 2.21, whereas insertion and return losses are shown in Figs. 2.22 and 2.23, respectively. It has to be mentioned that coloured lines are the measurements for each of the filters, while the dashed black line is the specification by the manufacturer.

2.4.2.3 Heterodyne Frequency Conversion for the RDA

The *LTC5549* mixer from Linear Technology, shown in Fig. 2.24(a), has been selected among other options because of its low input power requirements. It exhibits

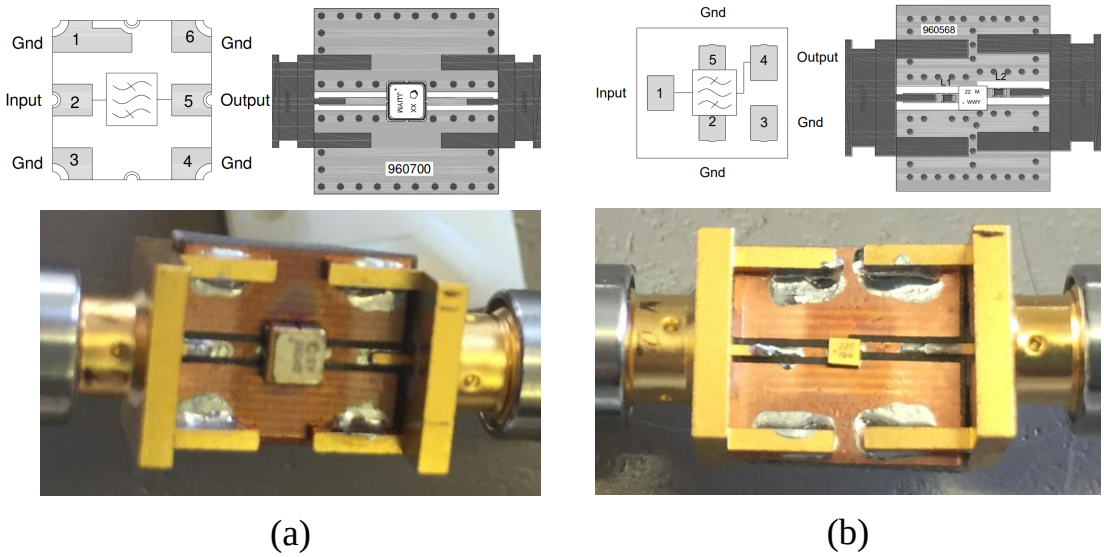

Figure 2.21: Picture of the proposed band-pass filters: (a) the *885009* (element #2 in Fig. 2.19); and (b) the *885017* (element #5 in Fig. 2.19).

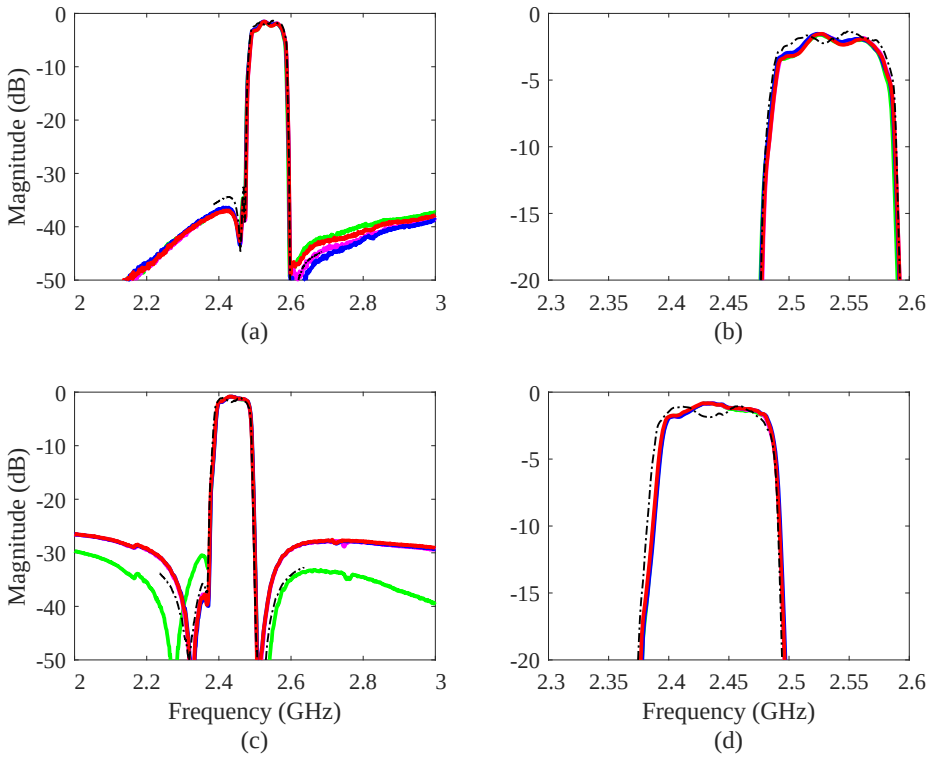

Figure 2.22: Insertion losses of the proposed BPFs: (a) and (b) for the *885009* (element #2 in Fig. 2.19); (c) and (d) for the *885017* (element #5 in Fig. 2.19).

a low conversion loss when compared to other similar mixers. A block schematic of the IC and the measurement of the conversion loss versus RF input power are shown in Fig. 2.24(b) and (c), respectively. It can be seen from the graph, that in the range $[-25, -20]$ of RF input power, the conversion loss variation is just about 0.6 dB, making it very robust for the pursued application. The importance of having

a low variation in the conversion loss lies in the fact that different conversion losses can introduce a small error in the output phase. The smaller this error offset is, the smaller the beam pointing error will be. Additionally, the required LO power is also small given that the IC builds an internal amplifier ("LO AMP" in Fig. 2.24(b)) which is externally biased through the *VCC*, *EN* and *GND* pins as it can be seen in Fig. 2.24(a). The biasing conditions are 3.3 V and 115 mA, and 0 dBm of power for the 4.9 GHz LO tone.

Also, in order to properly apply the LO tone to the four mixers, two stages of Wilkinson power dividers were cascaded to obtain a 1-by-4 power split (see Fig. 2.25). The first stage is a *4324-2* from Narda with 0.35 dB of insertion losses, as shown in the green traces on Fig. 2.26(a). The second and last stage is defined by two *ZN2PD2-50-S+* wilkinson dividers from MiniCircuits. These are more lossy in terms of insertion losses (0.6 dB and 0.75 dB) than the first stage. However, what really matters is the amplitude balance (shown on Fig. 2.26(b)). The blue, red and green lines are the internal amplitude balances which are below 0.05 dB. The black line refers to the external amplitude balance between the dividers of the second stage, in other words, how different is the power split between the two dividers.

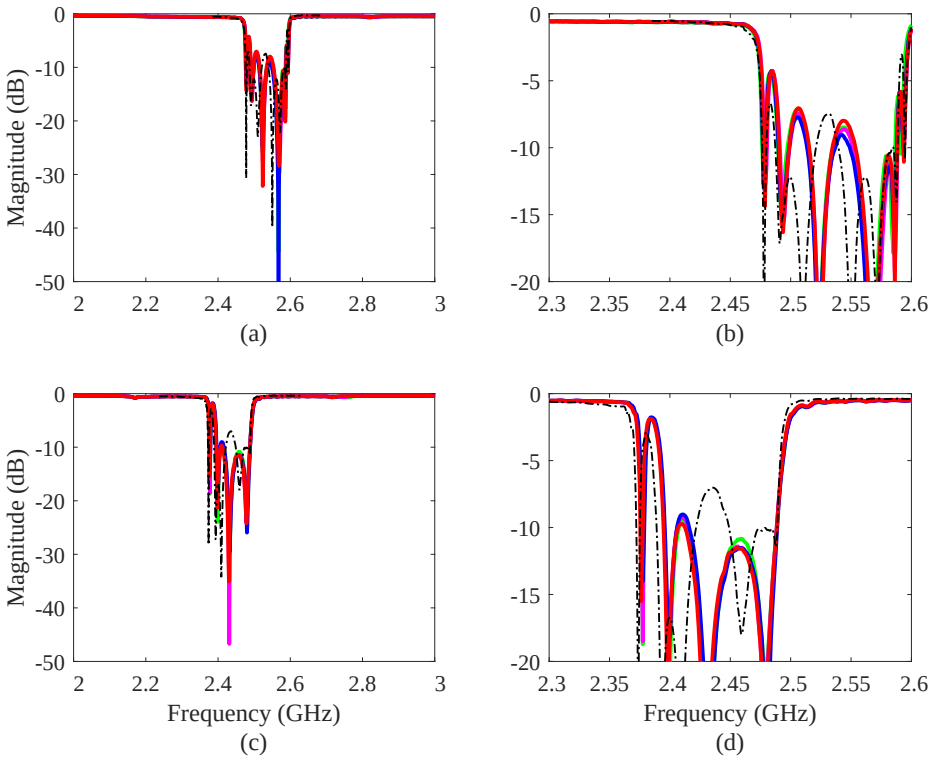

Figure 2.23: Return losses of the proposed BPFs: (a) and (b) for the *885009* (element #2 in Fig. 2.19); (c) and (d) for the *885017* (element #5 in Fig. 2.19).

For the frequency of operation, it shows a difference of around 0.1 dB which can be neglected. With respect to the phase balance (Fig. 2.26(c) and (d)), it can be seen that the differences are very tiny. In conclusion, it can be mentioned that the four mixers have a near perfect amplitude and phase balance for proper RDA operation.

2.4.3 Device under charge: Rectenna

The design of the receiver or DUC, shown in Fig. 2.27, is divided in two parts: transmission and reception.

1. Transmission: A voltage-controlled-oscillator (VCO) set to generate a tone at 2.5 GHz and 6.6 dBm of power is connected to a patch antenna that radiates the beacon tone with RHCP.

2. Reception (rectenna): A 2×1 patch array co-located with the transmitting patch, will be responsible for receiving the retrodirected power at 2.4 GHz.

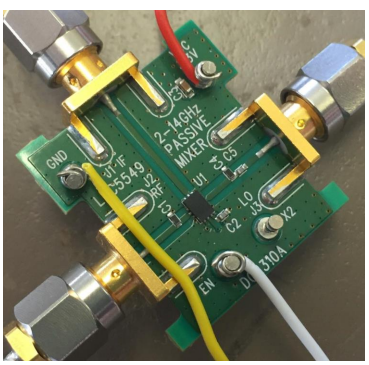

(a)

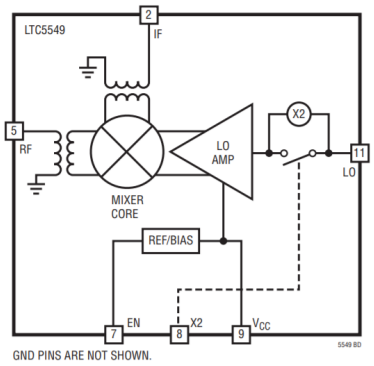

(b)

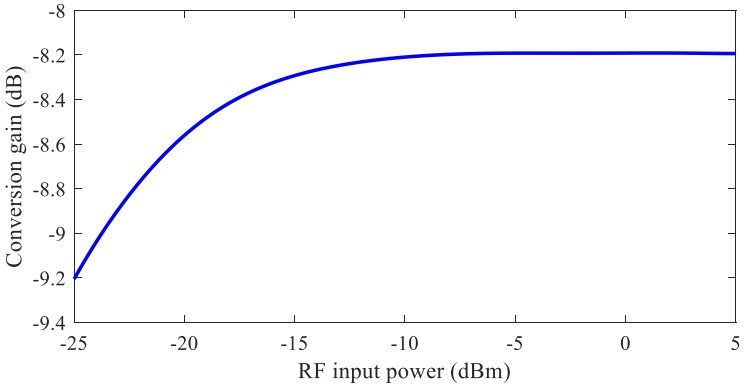

(c)

Figure 2.24: *LTC5549* mixer: (a) picture of one of the four mixers used, (b) IC block diagram [36] and (c) conversion loss measurement over RF input power completed at the Heriot-Watt University microwave lab.

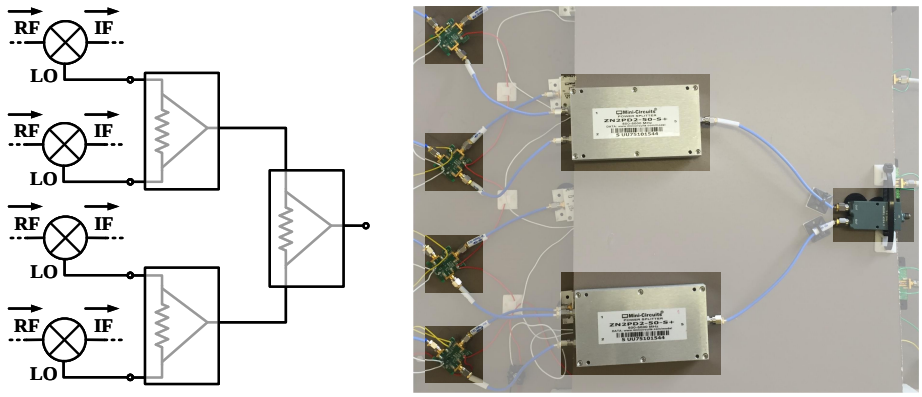

(a) (b)

Figure 2.25: The power split of the 4.9 GHz LO tone was made by cascading two stages of Wilkinson power dividers to obtain a 1-by-4 power split. Schematic (a) and picture (b).

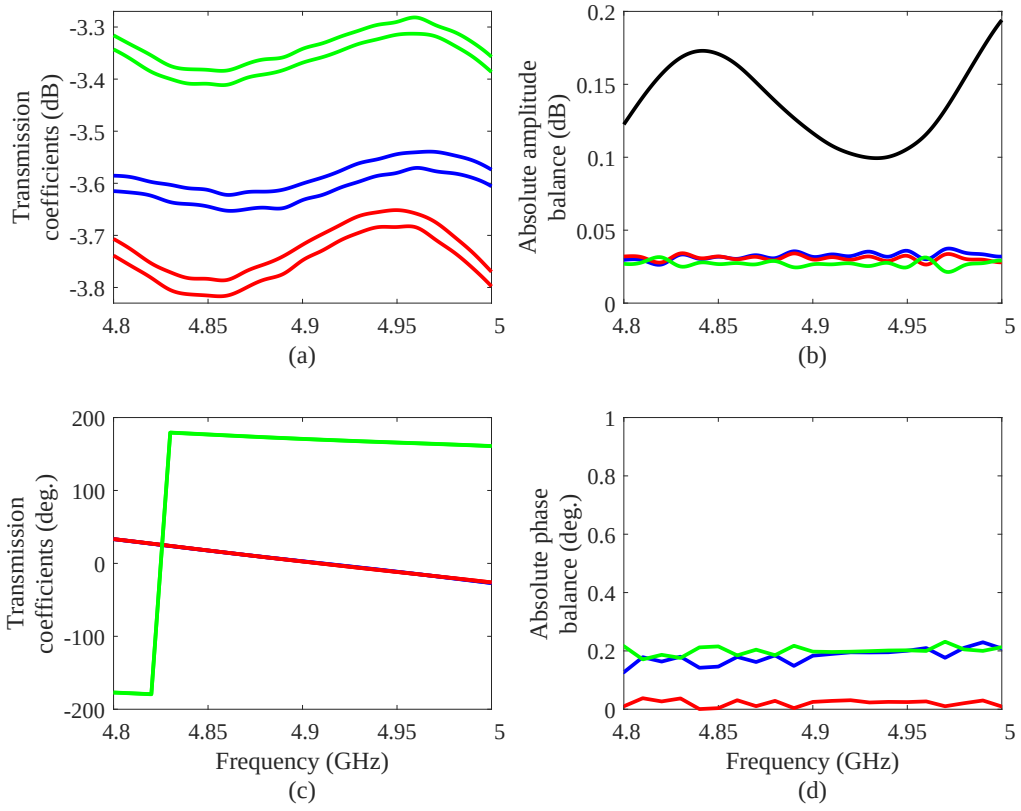

Figure 2.26: Amplitude (a-b) and phase balance (c-d) of the connectorized power split network.

The ports of these antennas are both connected to a Wilkinson power combiner and the output of the latter device, that carries all the received retrodirected power, is connected to the rectifier, which is in charge of converting the RF power into DC.

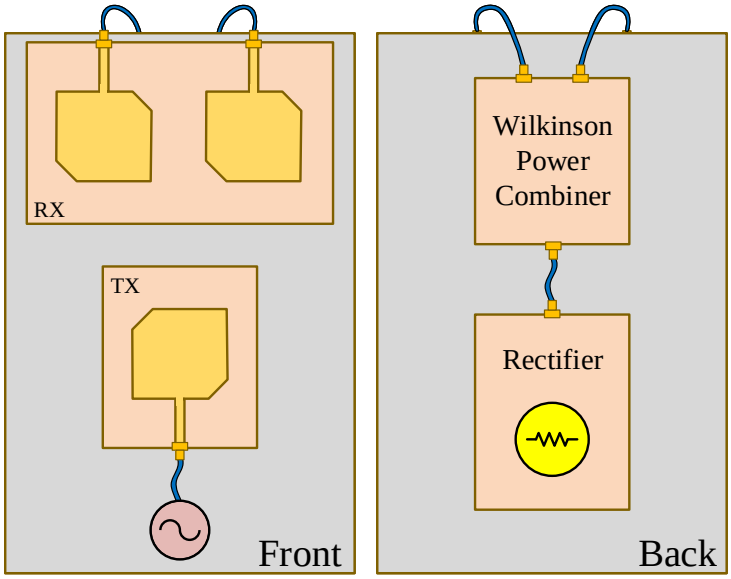

(a)

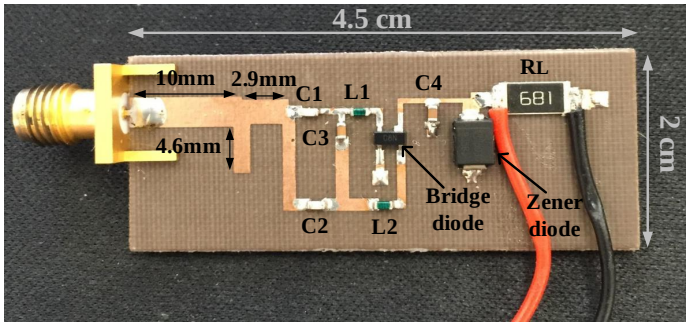

(b)

Figure 2.27: DUC schematic (a), and picture of the rectifier from [37] (b).

The structure of the rectifier, which is not the primary focus of this thesis, is further reported in [37] and comprises five different blocks (see Fig. 2.27). At the input, the matching network formed by an open ended single-stub is used to reduce the return losses at the working frequency band. Right after, a couple of capacitors are used as DC blockers to ensure that any DC power is routed to the rectifying diodes. Then, a T-type low-pass filter is used to reject any high order harmonics. The last two blocks are the rectifying part: first the bridge diode is used to rectify the RF fundamental frequency into DC, and finally, there is a voltage regulator block formed by a shunt capacitor that will filter any RF signal remaining. There is also a Zener diode, whose main purpose is to reduce the ripples of the final DC signal. In this design, the aim was to achieve the best RF-to-DC conversion efficiency with an input power of around 27 dBm, matching the power link budget previously estimated and defined in this chapter to be above 70%. The rectifier has been manufactured

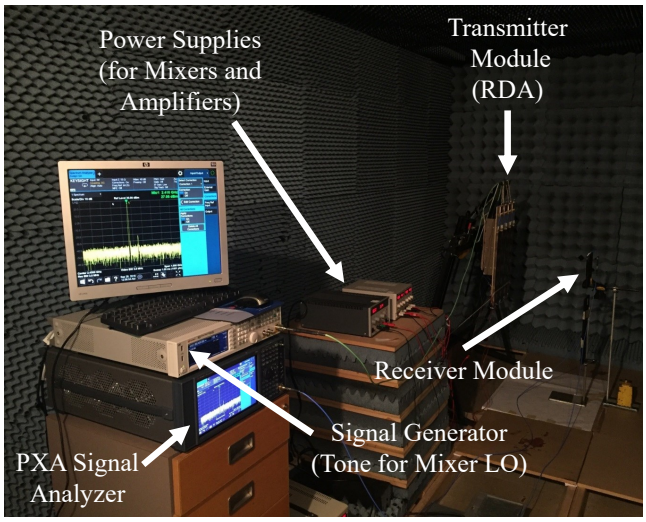

Figure 2.28: Picture of the measurement setup.

over the same type of substrate as the RDA antennas.

2.5 Complete RDA Circuit System Measurements for the Modified Pon with Subarrays

Assessment of the capabilities of the proposed RDA have been tested through bistatic and monostatic measurements in an anechoic chamber. The distance that separates the radiative NF with the FF regions is $R_2 \approx 5.1\,\text{m}$. Additionally, the distance that is the boundary of the reactive NF and the radiative NF is $R_1 \approx 74.3\,\text{cm}$, which means that measurements have been done in the reactive NF region.

The measurement setup is shown in Fig. 2.28. A N5182B MXG Vector Signal Generator from Keysight Technologies has been used to feed the 4.9 GHz LO signal to the mixers; to measure the received RF power at the output of the Wilkinson power combiner, a Keysight N9030B PXA Signal Analyser was used. Moreover, DC power supplies were needed to bias all the active components; i.e. driver amplifiers, power amplifiers, mixers and the VCO that generates the beacon tone at the DUC for self-tracking. The biasing of the RDA was made in series as shown in Fig. 2.19(b). Additionally, with the aid of a small mechanical stand, monostatic and bistatic patterns were measured (see Fig. 2.29(a-b)).

The classic procedure to get monostatic and bistatic patterns is shown in Fig. 2.29. The bistatic pattern corresponds to the radiation pattern of the RDA when

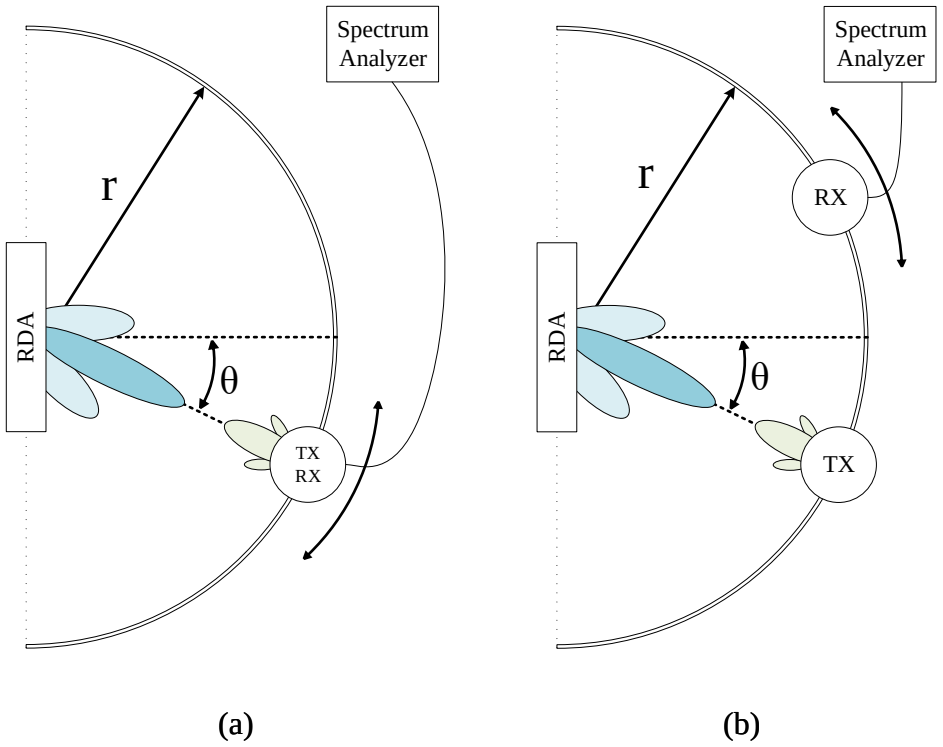

Figure 2.29: Monostatic (a) and Bistatic (b) measurement illustration.

the beacon tone is fixed at a given angle θ. To test if the RDA tracks properly the DUC, several bistatic patterns at different angular positions of the beacon signal are required. The way to measure this is leaving the transmit module of the DUC (VCO and patch antenna) stationary at a given angle, while the receiver module of the DUC rotates around to map the complete pattern for a fixed range. For this system, there are two types of bistatics depending if the measurement is made with or without the rectifier: RF-bistatics and DC-bistatics. As the aim of the measurement was to test the RDA bistatic performance, only RF-bistatics were measured.

On the other hand, the monostatic pattern can be defined as the envelope of the bistatics. This is obtained by rotating the entire DUC (transmit and receive modules co-located) around the RDA. Therefore, the RDA will be continuously pointing and tracking its maxima towards the DUC as it rotates. Thus, the obtained monostatic pattern will sample the power level of the main beam at the peak versus the angle of incidence. For this type of measurement, in order to test also the performance of the rectifier versus angle, both RF-monostatic and DC-monostatic were measured.

Some simulations and measurements of the normalised bistatic patterns are shown in Fig. 2.30. In order to get the simulated bistatic patterns, the proper relative phase

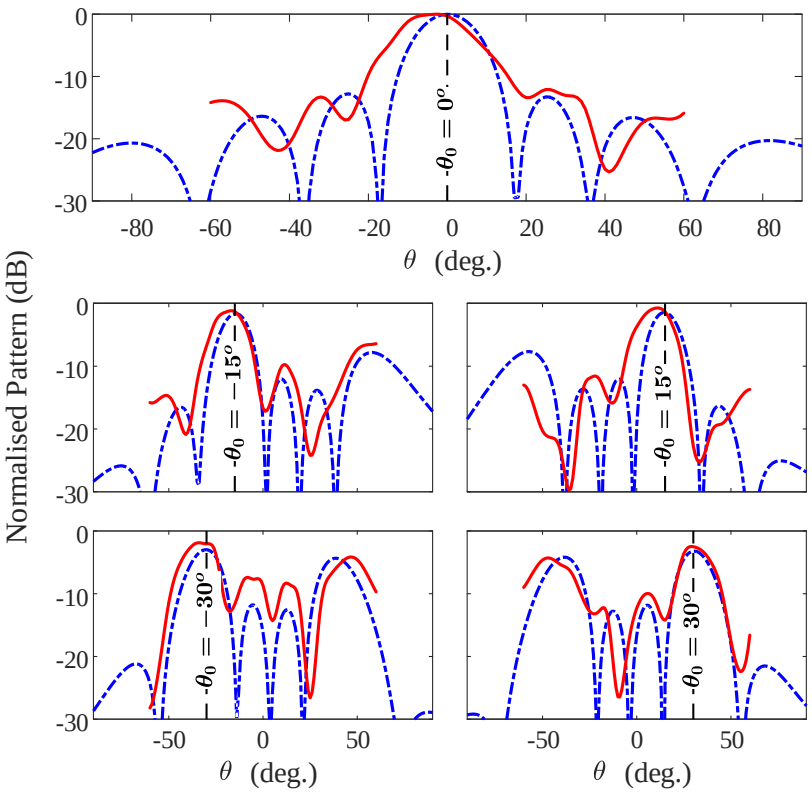

Figure 2.30: Measured (red line) and simulated (blue-dashed line) normalised bistatic patterns at different angles, from top-down and left-right: broadside, ±15° and ±30°.

difference between consecutive elements that makes the beam point to the targeted angle was applied in CST. It has to be mentioned that the reported simulations are the realized gain patterns and therefore are based on FF principles. Conversely, the measurements were made in the reactive NF given the spacing limitations of the chamber. Regardless results still show tracking capability for different pointing angles and can be observed that the agreement between simulations and measurements is acceptable. A small shift in the pattern can be seen, which might be caused by NF coupling effects, the phase noise in the active components, or an uneven power output from the amplifiers. Additionally, the separation of $0.85\lambda_0$ between sub-arrays increased the SLL for bistatics at angles far from broadside. For example, at $\theta = -15^o$ the measured SLL is $-6dB$. This is the minimum possible separation between sub-arrays, given the design of the feed network used for a CP series-fed patch array.

This spacing between sub-arrays could limit the field-of-view (FOV) of the array

which is defined by [38, 39]

$$\theta_{FOV} = \pm \arcsin\left(\frac{\lambda}{2d}\right) \tag{2.5.1}$$

where λ is the wavelength in free space and d is the distance between sub-arrays. For the proposed system, the expected FOV is $\pm 36.4°$ as it is demonstrated in Fig. 2.31, for the $\pm 30°$ cases, where the side lobes increased significantly. An alternative and more compact and complex feed network implementation could have improved the FOV while also reducing the SLL by applying a tapered amplitude distribution, but at the cost of reduced broadside gain. An array for this will be discussed in the next chapter.

Additional bistatic measurements are illustrated in Fig. 2.31. A progressive decay of the power level is observed as the bistatic angle is steered away from broadside. This is mainly due to the high directivity of the individual sub-arrays in the plane orthogonal to the scanning plane. This causes the directivity of the full array to decrease more severely when scanning, which varies proportionally to $\cos\theta$ [40]. Also, a monostatic pattern is shown in the red dashed line which demonstrates proper RDA operation. These results prove that the proposed system is able to operate in any field region, including the reactive NF. This suggests that the developed RDA circuit system is suitable for WPT applications.

Some additional monostatic trials and a DC-monostatic one are shown in Fig.

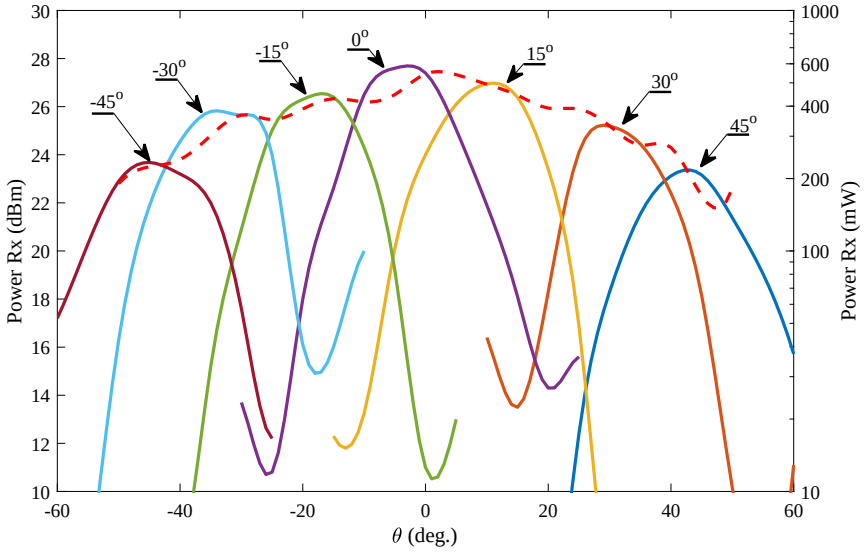

Figure 2.31: Monostatic and bistatic results (at $\pm 45^o, \pm 30^o, \pm 15^o$ and 0^o) for the proposed system. Left axis is in a dBm scale, while the right axis is in milliwatts.

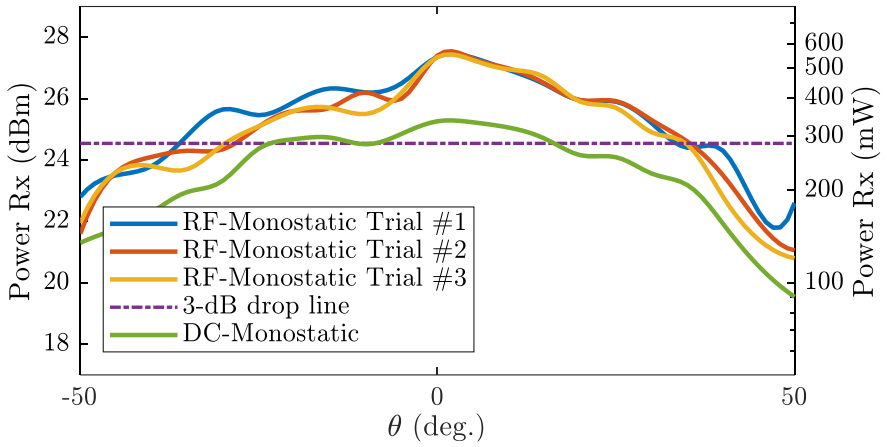

Figure 2.32: RF and DC Monostatic measurements. Left axis is in a dBm scale, while the right axis is in milliwatts (a); Efficiency versus incoming angle (b).

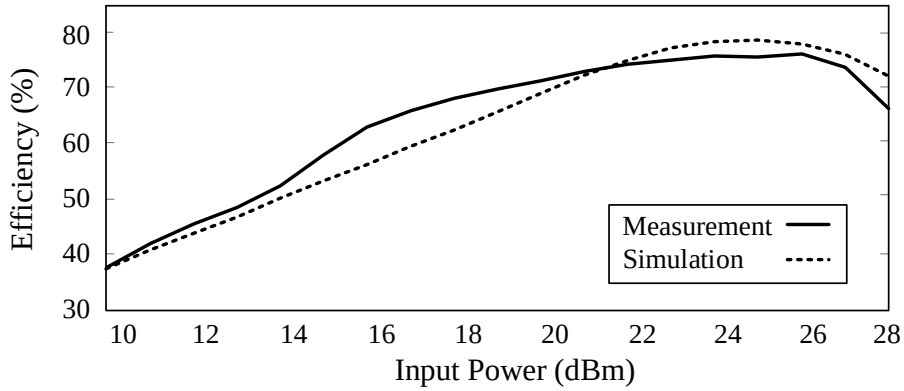

Figure 2.33: Measurements and simulations of the rectifier RF-to-DC efficiency at 2.4 GHz.

2.32. The different trials show repeatability meaning that the system has a stable response over time, and exhibiting 80° of 3-dB beamwidth, approximately. In terms of power balance at the DUC, the initial beacon generated by the DUC has an output power of 6.6 dBm and the DC power received from the RDA is always over 20 dBm over the full measured range $[-50°, -50°]$ which makes a positive power balance of 13 dB, which translated into linear units means that the received power is 20 times higher than the transmitted power. Moreover, from $-20°$ to 20° the received power is above 300 mW, achieving the targeted metric for a 50 cm range. It has to be mentioned that the drop of the DC-monostatic trace with respect the RF-monostatic ones, is caused by the efficiency of the rectifier.

Additionally, measurements to assess the power received versus distance were

made as shown in Fig. 2.34. As already mentioned previously, due to space restrictions in the chamber, these measurements were made in the reactive NF region. The noticeable difference between measured and simulated results can be justified in the fact that simulations were performed by applying an equi-phased distribution for the phases at each element, considering in this way that the receiver is located in the FF. Given that measurements are in the reactive NF, the elements are not equi-phased (see Fig. 2 from [15]). Such results demonstrate that the system is able to operate in any of the field regions.

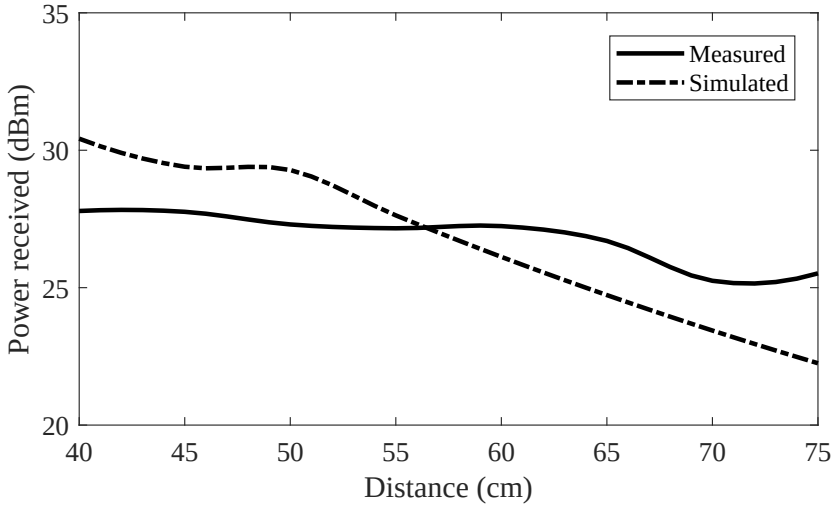

Figure 2.34: Retrodirected received power at broadside, for different ranges.

In Table 2.2, a comparison is made between some other relevant works and the reported RDA system. It has to be mentioned that for [41] it only gives the voltage received and does not show the impedance of the load, not being able to make a fair comparison with the rest of the works. With respect to [42], the receive antenna was placed inside pork tissue, increasing the losses and explaining its high value of losses in dB/m. Also, for this type of comparison, it has to be taken into account that the losses given in dB/m, is a non-linear value that depends on the distance, so it should be considered as an estimation. From this comparison, it is clear that our proposed design has the highest level of RF and DC power received.

Table 2.2: Comparison of the proposed work with others found in the literature

Ref.	Freq. (MHz)	Tx Array Size ($M \times N$)	Tx Architecture	Beam tracking	Distance (m)	Field Range	Tx Power (dBm)	Rx RF Power (dBm)	Rx DC Power (mW)
[41]	462.55	-	Classic Array	No	33.5	FF	36	-	3.3V
[42]	915	1×1	CP Patch	No	0.4	NF	25	-17.5	0.00514
[14]	915	2×2	Dig. Beamforming	Yes	0.5	NF	26	13	10
[15]	2450	16×1	RDA	Yes	1	NF	24	-	10
This work / [37]	2400/2500	4×4	RDA	Yes	0.5	NF, FF	36	27	350

2.6 Van Atta Design For 2-D Tracking

Apart from the proposed Pon design which is used for 1-D tracking, an alternative design based on the Van Atta concept has also been designed, built and tested in order to cover applications that need to have tracking in two planes. The antenna element has been manufactured following the design from [43], where the combination of a dual-polarized antenna with a 90° hybrid coupler forms a CP transceiver. Fig. 2.35 illustrates the antenna element in transmit (a) and receive (b) modes. In transmit mode, one of the inputs of the hybrid coupler is fed, making the signal to have a 3 dB power split at its output with a 90° of phase difference. Therefore, by connecting these outputs to adjacent sides of the patch, the antenna will be CP. On the other hand, in receive mode (b), the signal will be decomposed in both orthog-

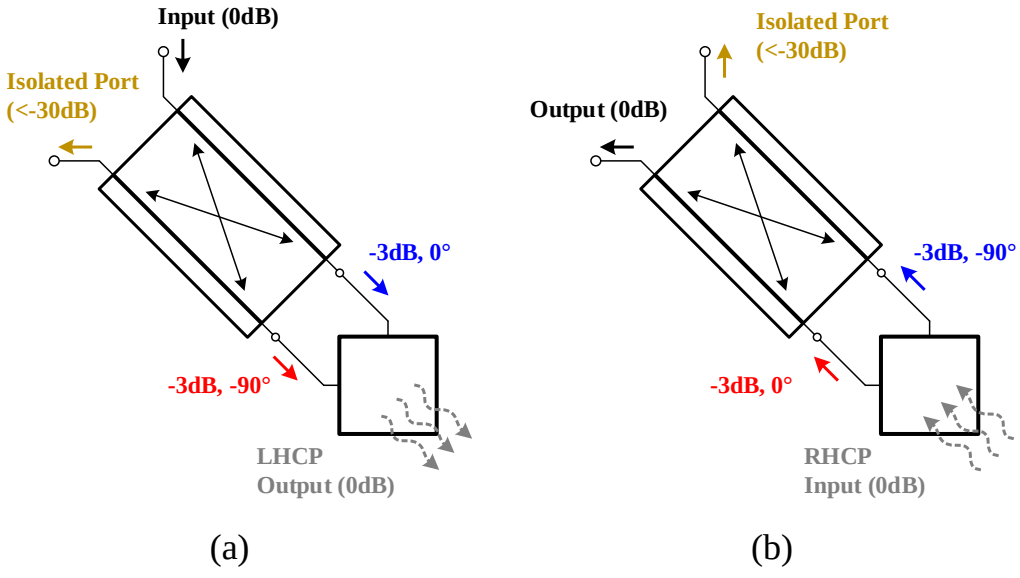

Figure 2.35: Antenna element schematic used in the design of the Van Atta RDA: (a) transmit mode and (b) receive mode with opposite polarizations.

onal components (horizontal and vertical) each of those will be fed into the hybrid coupler. Given that these signals are 90° apart, the hybrid will act as a combiner in this case, guiding all the power through one of the output ports and the other one would be isolated. The isolation ports are very useful for our design because they will be connected to the crossed path as it is shown in Fig. 2.36, enabling, in this way, two crossed paths. This avoids the need of bi-directional amplifiers. Moreover, the transmission lines are introduced to achieve 180° of phase difference between each antenna pair, for proper Van Atta RDA operation.

2.6.1 Antenna Array

The designed antenna array is shown in Fig. 2.37. As it can be seen from Fig. 2.37(b) and (c), the connection between the patches and the hybrids is made by resonant coupling through an H-shaped curved slot in the ground plane. Additionally the patches are elevated, leaving a small air gap that enhances the radiating bandwidth and the matching of the array, achieving values around $-20\,\mathrm{dB}$. Additionally, the squared slots etched in the radiating patches improves the isolation for at least $20\,\mathrm{dB}$. All these results are not reported for brevity.

Also, in order to work as a Van Atta RDA, the connections between patches are as follows: port 1 with port 6, port 2 with port 5, port 3 with port 8 and port 4 with port 7. Measurements and simulations for the radiation pattern of the array can be seen in Fig. 2.38, achieving a very good agreement.

2.6.2 Passive Van Atta RDA

Measurements and simulations of a passive Van Atta (using the array discussed in the last section) have been completed in order to test the tracking capabilities of the system. In Fig. 2.39 the measurement antenna setup is shown (a), the connections made for each element within the array (b) (including microstrip transmission lines to achieve the proper inter-element phase difference), the antenna elements used as the transmit beacon and the receiver (c), and the FF positioner in charge of the automatic rotation and acquisition of the data (d). A simulated and measured monostatic at $2.35\,\mathrm{GHz}$ is shown in Fig. 2.40, showing good agreement, and an even

broader 3-dB beamwidth in the measured trace than the simulated one (around 90°). Moreover, bistatic measurements have been also completed (Fig. 2.41), which show self-beam steering operation.

It should be mentioned that only passive Van-Atta RDA measurements were completed and reported in this thesis. This is because measurements of this RDA were completed using a new FF positioner making the bi-static RDA measurement (i.e. with amplifiers and not passive) not technically possible at the time of writing. Future work can include additional measurements to further illustrate the concept. Regardless, passive measurement results are in agreement with the simulations suggesting that a similar result is possible for a more advanced and active Van-Atta RDA.

2.6.3 Other Applications Including Monopulse Radar

As Fig. 2.37 shows, a sequential physical rotation of 90° had to be applied to the elements within the RDA in order to be able to employ them within the developed 2×2 CP RDA. Due to the fact that the connection between antenna elements is made in diagonal, the sequential rotation does not affect the RDA operation. However, this special arrangement can be exploited in monopulse radar [44] applications.

A monopulse system for target angle and range estimation, as a baseline, typically

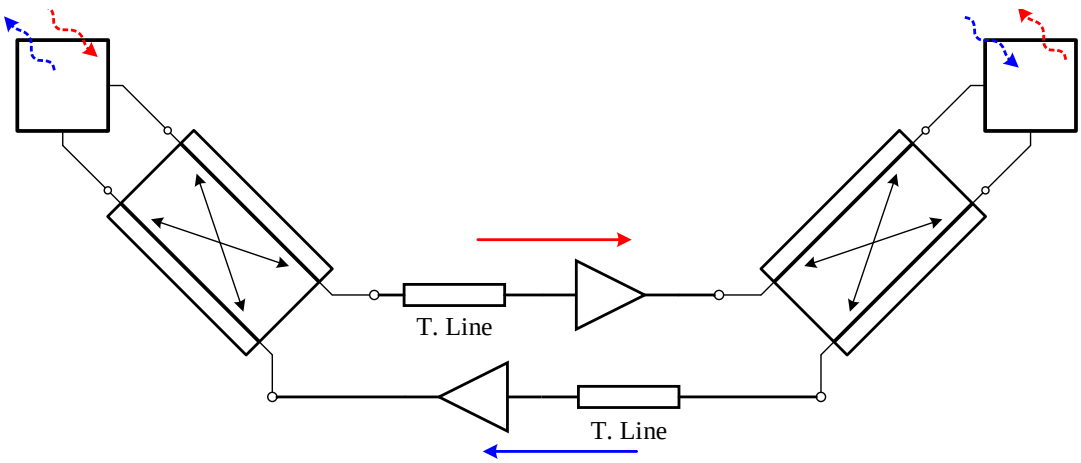

Figure 2.36: Schematic of the connections between one antenna pair considering an active Van Atta RDA where the total insertion phase difference between the incoming and outcoming signal paths (either red or blue paths) is 180°.

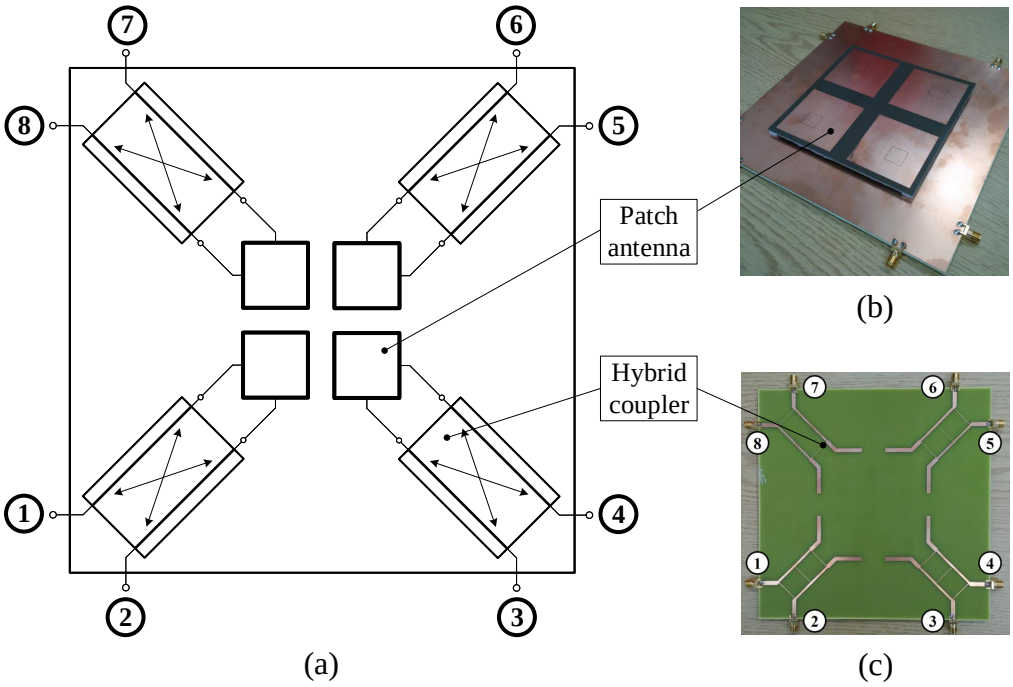

Figure 2.37: Array developed for the proposed Van Atta RDA considering a 2×2 arrangement.

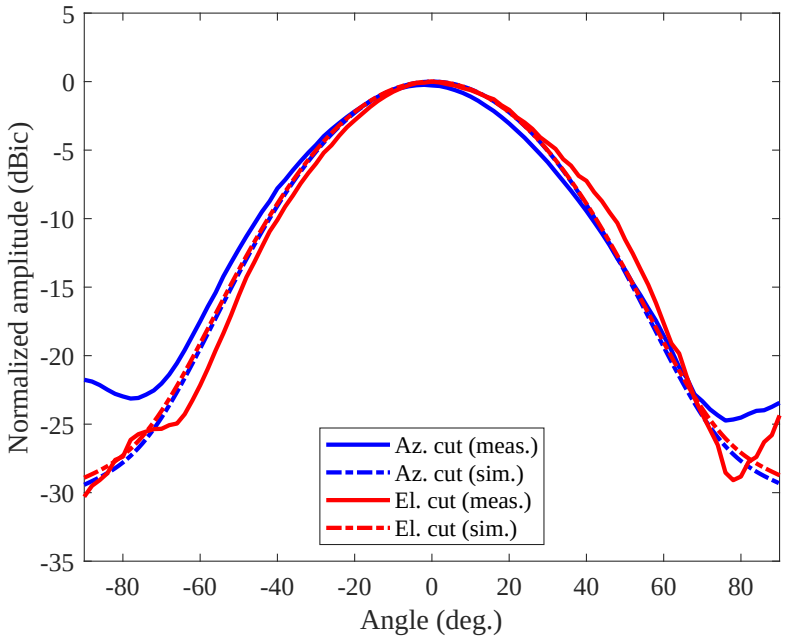

Figure 2.38: Simulated and measured antenna array radiation pattern considering the two principal planes.

consists of a 2×2 planar array (if azimuth and elevation angles are to be determined). Such a name was coined because it clearly expressed the ability to collect from each pulse the information needed for the azimuth and elevation angles, whereas older

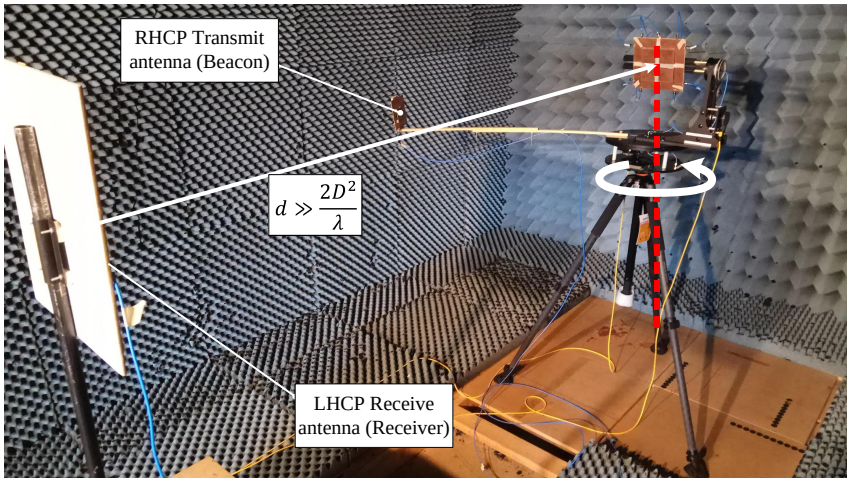

(a)

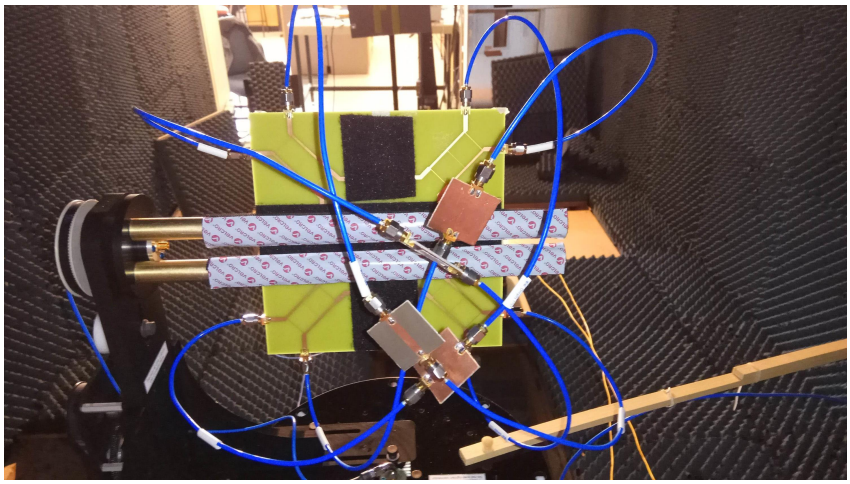

(b)

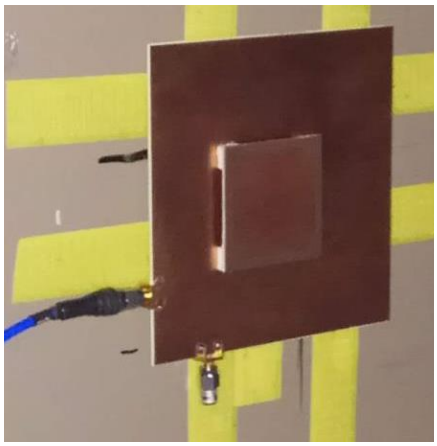

(c)

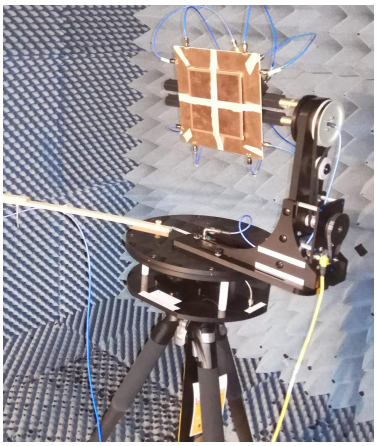

(d)

Figure 2.39: Bistatic measurement setup for the Van Atta RDA (a); connection arrangement to work as a passive Van Atta RDA (b); antenna element used as the beacon transmit antenna and the receive antenna (c); FF positioner used in the measurements (d).

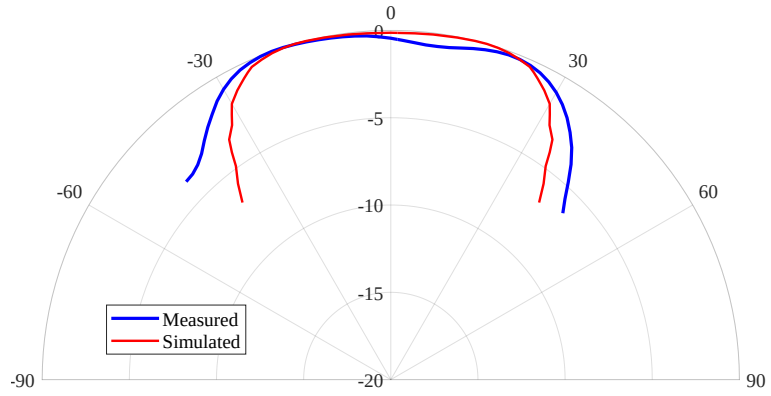

Figure 2.40: Measured and simulated monostatic pattern for the passive Van Atta RDA.

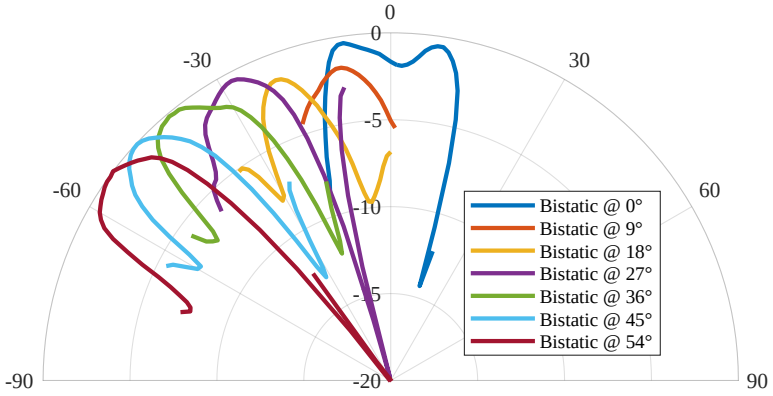

Figure 2.41: Measured bistatic patterns for the proposed Van Atta RDA.

techniques which used sequential lobing required several pulses to obtain the same amount of information [45]. To do so, each of the antenna elements generate a squinted beam as it is shown in Fig. 2.42. An initial thought would be to use the four beams (A, B, C and D) independently, connecting each antenna to individual and identical receivers. However, even if adjusted initially for equal gain and phase, there would be unequal variations happening over time, signal level, environmental conditions and so on. This would cause large drifts in the radar axis (boresight direction), having the need to find an alternative solution for this. Therefore, sum and difference outputs are needed to help reducing the aforementioned drift and having in this way a more stable null axis. Sum and traverse and elevation difference expressions are given by:

$$\Sigma = A + B + C + D \tag{2.6.1}$$

$$\Delta_{\text{tr}} = (C + D) - (A + B) \tag{2.6.2}$$

$$\Delta_{\text{el}} = (A + C) - (B + D) \tag{2.6.3}$$

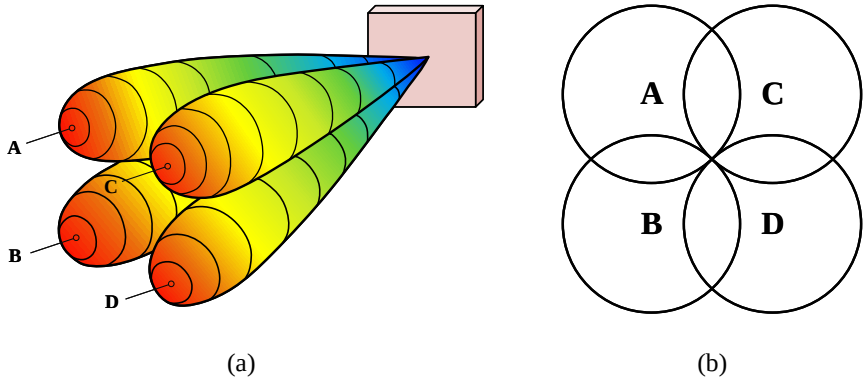

(a) (b)

Figure 2.42: Individual beams generated by each individual element. Perspective (a) and front view (b).

Once these are obtained, it is possible to obtain the a pair of angle coordinates and the range of the measured target. Additionally, the obtained coordinates will feed the servo motors to adjust the antenna position in order to have the axis null towards the target. However, for many cases the servo is too slow to follow the path of the target, on which case the voltage ratios between the differences and the sum are used for error correction and still be able to achieve an accurate angle estimation (for more info see [46]).

As it has been already mentioned, the existing sequential rotation of the antennas (shown in Fig. 2.43(a)) has to be taken into account for the design of the microwave combining network (Fig. 2.43(b)). Regarding the sum beam pattern, this sequential rotation needs to be compensated by introducing a 90° of opposite sequential delay to each antenna element.

In our design, simulated and measured sum and difference beam patterns are shown in Fig. 2.45 in which the agreement achieved is very good.

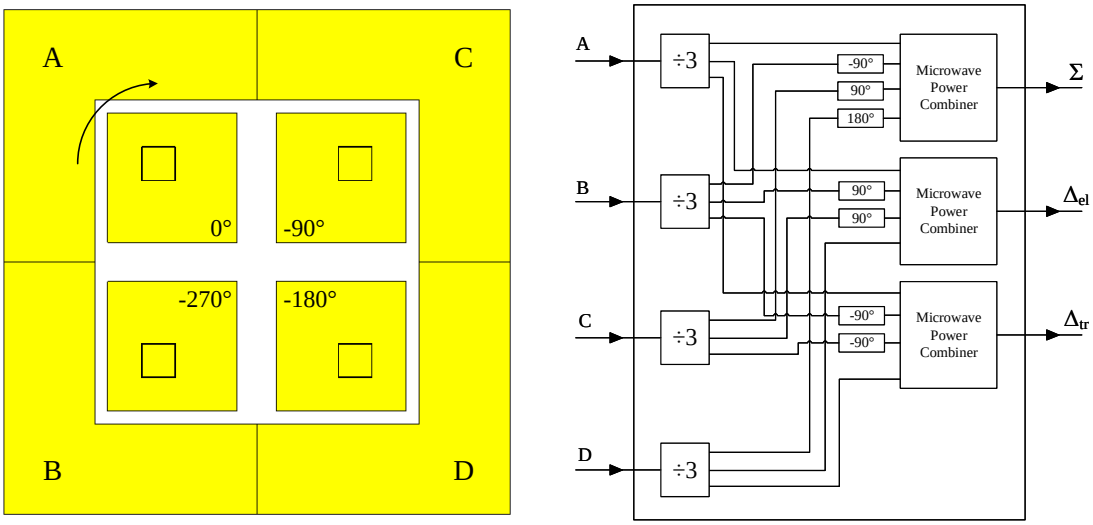

(a) (b)

Figure 2.43: Sequential clockwise phase rotation of the array (a) and the microwave combining network to obtain the needed sum and difference outputs for angle and range estimations (b).

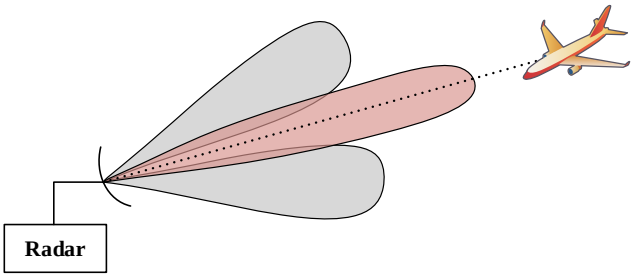

Figure 2.44: Illustration of a monopulse antenna and radar with sum and difference beams.

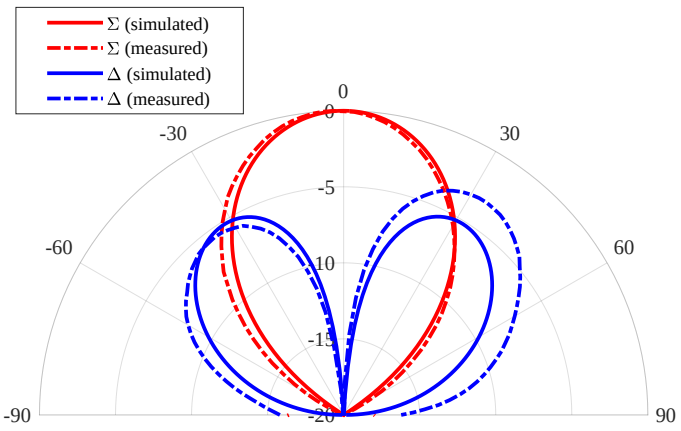

Figure 2.45: Measured and simulated monopulse (sum and difference patterns) using the antenna array from Fig. 2.37.

2.7 Conclusion

Most of the systems for WPT follow the inductive coupling method that has the main disadvantage of mobility limitations. In this chapter, a novel retrodirective system for wireless power transmission which circumvents this problem has been discussed. However, preliminary studies of an earlier Pon RDA prototype have been done in order to test the tracking capabilities either in the reactive NF or in the radiative NF, given that in [29] it had been demonstrated that the performance of a Pon RDA in the reactive NF could generate a null in the monostatic pattern at angles close to broadside.

For the case of the proposed prototype, this null appeared in the reactive NF region but still was able to track properly as the bistatic results show. Moreover, as the cost of the system can be high, a hybrid solution between a 1-D and a 2-D Pon RDA has been proposed by using sub-array elements that can boost the overall system gain. The only problem that this can impose is the loss of scanning in one plane, being still acceptable for applications at which the DUC moves reasonably close to the desired scanning plane. Results also show good agreement between the simulations and measurements, exhibiting up to 350mW of DC power converted from an initial 10mW tone at a distance of 50cm.

These results suggest that the proposed RDA system is a good candidate for mid-range WPT applications working at 2.4/2.5 GHz. It should also be made clear that the design, manufacture and implementation of the RDA was Pascual D. Hilario Re's main task [13], whereas the design, manufacture and implementation of the rectenna was made by Samuel Rotenberg as reported in [37] and [47]. Additionally, a 2×2 Van Atta RDA was also developed by Pascual and presented in this chapter which enables tracking in the full 3-D space. More specifically, the use of two-port antennas in combination with hybrid couplers, enables the isolation between crossed paths and by proper feeding of the antenna array, it could be used for new monopulse radar systems and other new RDA architectures.

References

[1] K. Huang and X. Zhou, "Cutting the last wires for mobile communications by microwave power transfer," *IEEE Communications Magazine*, vol. 53, no. 6, pp. 86–93, 2015.

[2] S. Y. R. Hui, W. Zhong, and C. K. Lee, "A critical review of recent progress in mid-range wireless power transfer," *IEEE Transactions on Power Electronics*, vol. 29, no. 9, pp. 4500–4511, Sept 2014.

[3] B. Strassner and K. Chang, "Microwave Power Transmission: Historical Milestones and System Components," *Proceedings of the IEEE*, vol. 101, no. 6, pp. 1379–1396, 2013.

[4] N. Shinohara and S. Kawasaki, "Recent wireless power transmission technologies in japan for space solar power station/satellite," in *RWS 2009 IEEE Radio and Wireless Symposium, Proceedings*, San Diego, CA, 2009, pp. 13–15.

[5] N. Shinohara, "Power Without Wires," *IEEE Microwave Magazine*, vol. 12, no. 7, pp. S64–S73, 2011.

[6] A. Munir and B. T. Ranum, "Wireless Power Charging System for Mobile Device Based on Magnetic Resonance Coupling," in *The 5th International Conference on Electrical Engineering and Informatics*, Bali, 2015, pp. 221–224.

[7] J. Garnica, R. a. Chinga, and J. Lin, "Wireless power transmission: From far field to near field," *Proceedings of the IEEE*, vol. 101, no. 6, pp. 1321–1331, 2013.

[8] C.-S. Wang, O. H. Stielau, and G. A. Covic, "Design Considerations for a Contactless Electric Vehicle Battery Charger," *IEEE Transactions on Industrial Electronics*, vol. 52, no. 5, pp. 1308–1314, 2005.

[9] P. Li and R. Bashirullah, "A wireless power interface for rechargeable battery operated medical implants," *IEEE Transactions on Circuits and Systems II: Express Briefs*, vol. 54, no. 10, pp. 912–916, Oct 2007.

[10] P. Kildal, *Foundations of Antenna Engineering: A Unified Approach for Line-of-sight and Multipath*, ser. Artech House antennas and electromagnetics analysis library. Artech House Publishers, 2015.

[11] S. L. Karode and V. F. Fusco, "Near field focusing properties of an integrated retrodirective antenna," in *IEE National Conference on Antennas and Propagation,*, April 1999, pp. 45–48.

[12] N. B. Buchanan and V. F. Fusco, "Beam steering using retrodirective array near field characteristics," in *2009 European Microwave Conference (EuMC)*, Sept 2009, pp. 1338–1340.

[13] P. D. H. Re, S. K. Podilchak, S. Rotenberg, G. Goussetis, and J. Lee, "Retrodirective antenna array for circularly polarized wireless power transmission," in *2017 11th European Conference on Antennas and Propagation (EUCAP)*, March 2017, pp. 891–895.

[14] P. S. Yedavalli, T. Riihonen, X. Wang, and J. M. Rabaey, "Far-field rf wireless power transfer with blind adaptive beamforming for internet of things devices," *IEEE Access*, vol. 5, pp. 1743–1752, 2017.

[15] S. T. Khang, D. J. Lee, I. J. Hwang, T. D. Yeo, and J. W. Yu, "Microwave power transfer with optimal number of rectenna arrays for midrange applications," *IEEE Antennas and Wireless Propagation Letters*, vol. 17, no. 1, pp. 155–159, Jan 2018.

[16] N. Buchanan and V. Fusco, "Developments in retrodirective array technology," *IET Microwaves, Antennas & Propagation*, vol. 7, no. 2, pp. 131–140, 2013.

[17] C. Pon, "Retrodirective array using the heterodyne technique," *IEEE Transactions on Antennas and Propagation*, vol. 12, no. 2, pp. 176–180, 1964.

[18] R. Y. Miyamoto and T. Itoh, "Retrodirective arrays for wireless communications," *IEEE Microwave Magazine*, vol. 3, no. 1, pp. 71–79, 2002.

[19] L. V. Atta, "Electromagnetic Reflector," Patent, 1959.

[20] S.-J. Chung, S.-M. Chen, and Y.-C. Lee, "A novel bi-directional amplifier with applications in active van atta retrodirective arrays," *IEEE Transactions on Microwave Theory and Techniques*, vol. 51, no. 2, pp. 542–547, Feb 2003.

[21] E. Rutz-Philipp, "Spherical Retrodirective Array," *IEEE Transactions on Antennas and Propagation*, vol. 12, no. 2, pp. 187–194, 1964.

[22] D. M. K. A. Yo, W. E. Forsyth, and W. A. Shiroma, "A 360 retrodirective self-oscillating mixer array," *IEEE MTT-S International*, vol. 2, pp. 813–816, 2000.

[23] S. L. Karode and V. F. Fusco, "Multiple target tracking using retrodirective antenna arrays," in *IEE National Conference on Antennas and Propagation,*, April 1999, pp. 178–181.

[24] V. F. Fusco, "Response of retrodirective array in the presence of multiple spatially separated sources," *IEEE Transactions on Antennas and Propagation*, vol. 54, no. 4, pp. 1352–1354, April 2006.

[25] C.-G. Sun and J.-L. Li, "Wideband time reversal of microwave signals based on phase conjugating," *Radioengineering*, vol. 27, pp. 1085–1091, 09 2018.

[26] N. B. Buchanan and V. Fusco, "Bit error rate performance enhancement of a retrodirective array over a conventional fixed beam array in a dynamic multipath environment," *IEEE Transactions on Microwave Theory and Techniques*, vol. 58, no. 4, pp. 757–763, April 2010.

[27] B. E. Henty and D. D. Stancil, "Multipath-enabled super-resolution for rf and microwave communication using phase-conjugate arrays," *Phys. Rev. Lett.*, vol. 93, p. 243904, Dec 2004. [Online]. Available: https://link.aps.org/doi/10.1103/PhysRevLett.93.243904

[28] T. Brabetz, V. F. Fusco, and S. Karode, "Balanced subharmonic mixers for retrodirective-array applications," *IEEE Transactions on Microwave Theory and Techniques*, vol. 49, no. 3, pp. 465–469, Mar 2001.

[29] S. L. Karode and V. F. Fusco, "Near field focusing properties of an integrated retrodirective antenna," in *IEE National Conference on Antennas and Propagation,*, April 1999, pp. 45–48.

[30] C. Balanis, *Antenna Theory: Analysis and Design*. Wiley, 2015.

[31] H. G. Schantz, "Near field propagation law a novel fundamental limit to antenna gain versus size," in *2005 IEEE Antennas and Propagation Society International Symposium*, vol. 3A, July 2005, pp. 237–240.

[32] *P.1238 : Propagation data and prediction methods for the planning of indoor radiocommunication systems and radio local area networks in the frequency range 300 MHz to 100 GHz*, ITU-T Std., Rev. 8, jul 2015.

[33] N. Shinohara, "Beam control technologies with a high-efficiency phased array for microwave power transmission in japan," *Proceedings of the IEEE*, vol. 101, no. 6, pp. 1448–1463, June 2013.

[34] G. F. Hamberger, A. Drexler, S. Trummer, U. Siart, and T. F. Eibert, "A planar dual-polarized microstrip 1d-beamforming antenna array for the 24ghz ism-band," in *2016 10th European Conference on Antennas and Propagation (EuCAP)*, April 2016, pp. 1–5.

[35] R. Garg, P. Bhartia, I. Bahl, and A. Ittipiboon, *Microstrip Antenna Design Handbook*. Artech House, 2001, ch. 8, p. 524.

[36] "2ghz to 14ghz microwave mixer with integrated lo frequency doubler," LTC5549, Linear Technology, Sep 2015, rev. A.

[37] S. A. Rotenberg, P. D. H. Re, S. K. Podilchak, G. Goussetis, and J. Lee, "An efficient rectifier for an rda wireless power transmission system operating at 2.4 ghz," in *2017 XXXIInd General Assembly and Scientific Symposium of the International Union of Radio Science (URSI GASS)*, Aug 2017, pp. 1–3.

[38] C. Balanis, *Antenna Theory: Analysis and Design*, 3rd ed. Wiley, 2015, ch. 6, pp. 300–301.

[39] S. Rao, "Mimo radar," Texas Instruments Inc., Texas Instruments, Post Office Box 655303, Dallas, Texas 75265, Tech. Rep., May 2017.

[40] R. Mailloux, *Phased Array Antenna Handbook*, 2nd ed., ser. Antennas and Propagation Library. Artech House, 2005.

[41] C. Cato and S. Lim, "Uhf far-field wireless power transfer for remotely powering wireless sensors," in *2014 IEEE Antennas and Propagation Society International Symposium (APSURSI)*, July 2014, pp. 1337–1338.

[42] C. Liu, Y. Zhang, and X. Liu, "Circularly polarized implantable antenna for 915 mhz ism-band far-field wireless power transmission," *IEEE Antennas and Wireless Propagation Letters*, vol. 17, no. 3, pp. 373–376, March 2018.

[43] X.-Z. Lai, Z.-M. Xie, Q.-Q. Xie, and X.-L. Cen, "A Dual Circularly Polarized RFID Reader Antenna With Wideband Isolation," *IEEE Antennas and Wireless Propagation Letters*, vol. 12, pp. 1630–1633, 2013.

[44] U. Nickel, "Overview of generalized monopulse estimation," *IEEE Aerospace and Electronic Systems Magazine*, vol. 21, no. 6, pp. 27–56, June 2006.

[45] S. Sherman and D. Barton, *Monopulse Principles and Techniques*, 2nd ed., ser. Artech House radar library. Artech House, 2011.

[46] ——, *Monopulse Principles and Techniques*, 2nd ed., ser. Artech House radar library. Artech House, 2011, pp. 6–13.

[47] S. Rotenberg, S. Podilchak, P. H. Re, C. Mateo-Segura, Goussetis, and J. Lee, "Efficient rectenna for wireless power transmission systems," *IEEE Transactions on Microwave Theory and Techniques*, (under review, submitted Nov. 2018).

Chapter 3

Circularly Polarized Series Fed Antenna Array Design

3.1 Introduction

One of the main challenges in the design of low-profile microstrip antenna arrays is to build the feed system in a way that does not interfere with the radiation characteristics of the array. Especially, coupling and size of the feed system, are two important factors to be minimised. In the previous chapter, a 4×4 transmitting array divided into a network of 4×1 sub-arrays was proposed. Each of these, was fed in series by conventional transmission lines on both sides of the row, each of those feeding one of the two orthogonal modes for CP radiation. This series-fed antenna

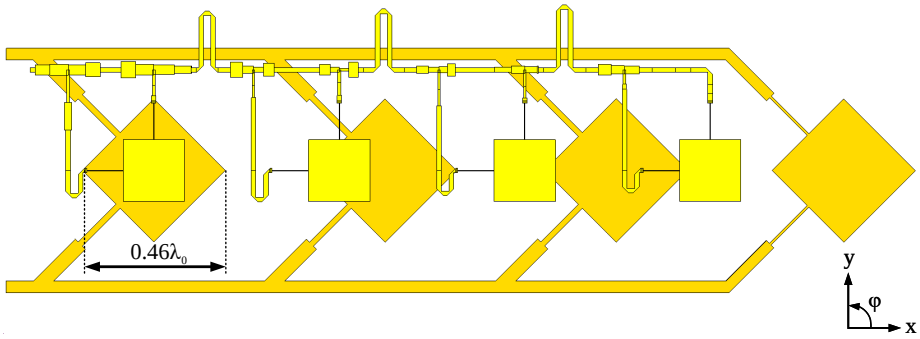

Figure 3.1: New redesign for SLL improvement by the use of meanders and impedance transformes (yellow), compared with the proposed RDA sub-array design from the previous chapter (orange).

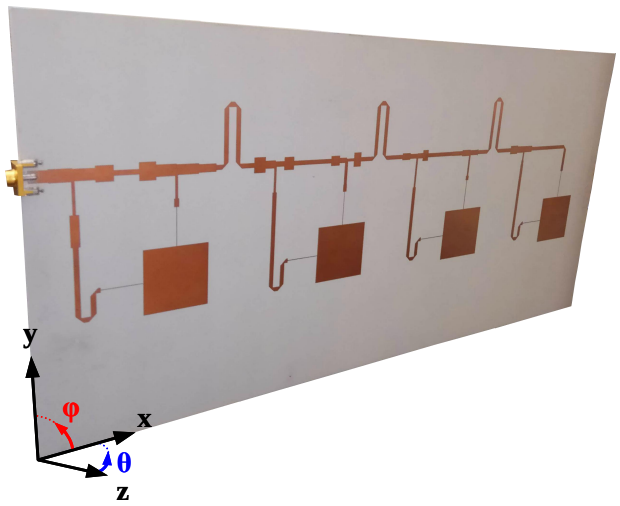

Figure 3.2: Picture of the manufactured series-fed array (SFA).

design is shown in Fig. 3.1 in orange. Given this arrangement, the distance between rows was 0.85λ and by consequence a high sidelobe level (SLL) was obtained from a certain scanning angle (i.e. $|\theta_0| \geq 30°$, being θ_0 the scanning angle and $\phi = 90°$ which is contained within the y-z plane). Moreover, the distance between patches that are in the same row was also large ($0.73\lambda_0$). The need for low SLLs is important for WPT applications, especially when dealing with high levels of transmit power. This is because of the possible health concerns when dealing with radiated fields and the human body. Moreover, side-lobes can be pointing and radiating power towards other unwanted directions which are different from the main beam which could also be steered. This could define a situation for health and safety considerations, in that unwanted power is radiated in the direction of the side-lobes, and this perhaps provides some justification that the optimization of the array (to have low SLLs) is important while also maintaining a decent gain.

Additionally, in terms of polarization, the use of CP antennas within an RDA can become problematic for multipath scenarios, where changes in the polarization sense can occur. For example, when the radiated CP signal hits a wall, ceiling or floor. However, the RDA system has been designed for the direct line of sight case only, as dictated by the funder (Samsung) and our project officer Jaesup Lee. Nevertheless, a possible solution to accommodate such a multipath scenario would be the use of a dual-polarization RDA; i.e. one that can transmit and recieve both vertical and horizontal components as in [1].

In this chapter, an alternative design has been proposed in order to reduce the

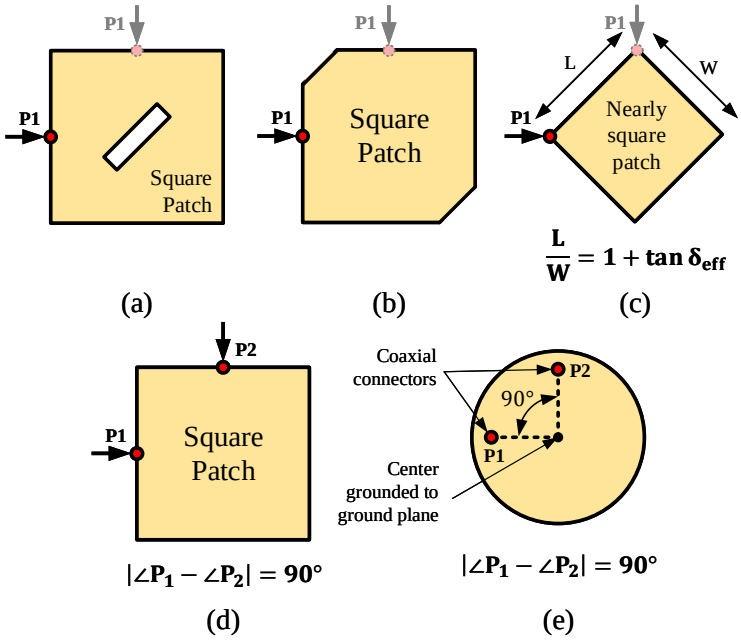

Figure 3.3: Different arrangements for CP considering microstrip patches [2]. Specifically, (a), (b) and (c) just need to have one port to achieve CP. To switch its polarization sense, one just needs to feed to the very next corner/edge. On the other hand, (d) and (e) need to have two ports excited simultaneously with a phase difference of 90°, but generally offer an increased axial ratio performance. To switch its polarization sense, the phase difference between the ports needs to be inverted from $-90°$ to $+90°$ or vice versa.

SLL while maintaining high gain within a single layer design. Also, a comparison with other works found in the literature will be made, demonstrating a better performance in terms of axial ratio (AR) and SLL for the proposed low-profile design.

3.2 Array element design

In the previous chapter, the design having two parallel feed lines was too large causing high SLL, as shown in Fig. 2.30. In the alternative design proposed in this chapter, the aim is to use just one feed line for size reduction while also improving antenna performance. This size difference between both prototypes is shown in Fig. 3.1. A starting point in the design of the CP series-fed array, is selection of the individual radiating element and its feeding.

Some rectangular and circular patch arrangements for circular polarization (CP)

can be seen in Fig. 3.3. For simplicity in the design process, the arrangement shown in Fig. 3.3(d) was chosen as in the previous design (see Fig. 3.4 for the single element and Fig. 3.2 for the full array). Quarter-wave transformers are connected to the edges of the patch providing connectivity to the antenna element with a 90° phase difference between connecting ports for CP radiation. Some simulation results are shown in Figs. 3.5, 3.6, 3.7 and 3.8. As it can be seen in Figs. 3.5 and 3.6, the bandwidth that this type of antenna exhibits is very narrow, being in this case around 3%. However, this bandwidth might be acceptable for certain applications such as radar and the developed RDA for WPT. Additionally, Fig. 3.5 shows a very low axial ratio over frequency, demonstrating this design to be very consistent in terms of CP performance. However, it should be mentioned that this is an ideal simulation since the phase difference between ports is fixed at 90° over the studied frequency range. In a more practical implementation, an exact 90° phase difference will likely not be maintained due to the integration of a feeding circuit. Regardless, gain values above 5 dBic are observed for both radiating elements. The selected PCB substrate was RO3206 from Rogers with $h = 1.27\,\text{mm}$, $\varepsilon_r = 6.15$ and $\tan\delta = 0.0027$. If compared to the dielectric constant of the design proposed in the previous chapter; i.e. $\varepsilon_r = 2.18$, the substrate employed in this chapter has a relative dielectric constant which is almost three times this value.

On the one hand, increasing the relative dielectric constant usually leads to higher losses [3] (i.e. surface waves and material losses), involving therefore, lower radiation efficiencies. This is shown in Fig. 3.6, where the total efficiency (radiation efficiency which includes mismatch and material losses) at the frequency of operation reaches almost 75% against the 87% achieved in the previous design (see Fig. 3.1), which substrate has a dielectric constant of $\varepsilon_r = 2.18$. However, increasing the permittivity of the substrate also helps reducing the physical size of the antenna, as shown in Fig. 3.1, given that the guided wavelength ($\lambda_g = \frac{c}{f\sqrt{\varepsilon_r}}$) will be shorter, and therefore, the distance between array elements can also be shorter having, then, a decrease in the SLL. Moreover, by using an antenna element which radiation pattern presents an important decay with respect to the maxima at the angular position of the side-lobe, the SLL would decrease even more. To compensate for the increased losses due to the increase of the substrate relative permittivity, a thinner material ($1.27\,\text{mm} < 1.57\,\text{mm}$, about 20% thinner) has been chosen if compared to

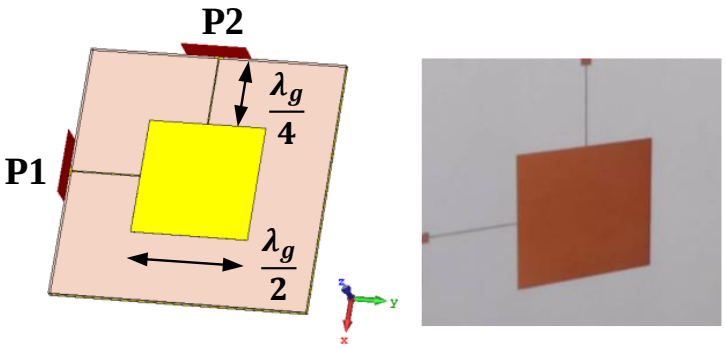

Figure 3.4: CST design of the patch antenna element (left) and picture of the manufactured design (right).

the previous design that was introduced in the previous chapter.

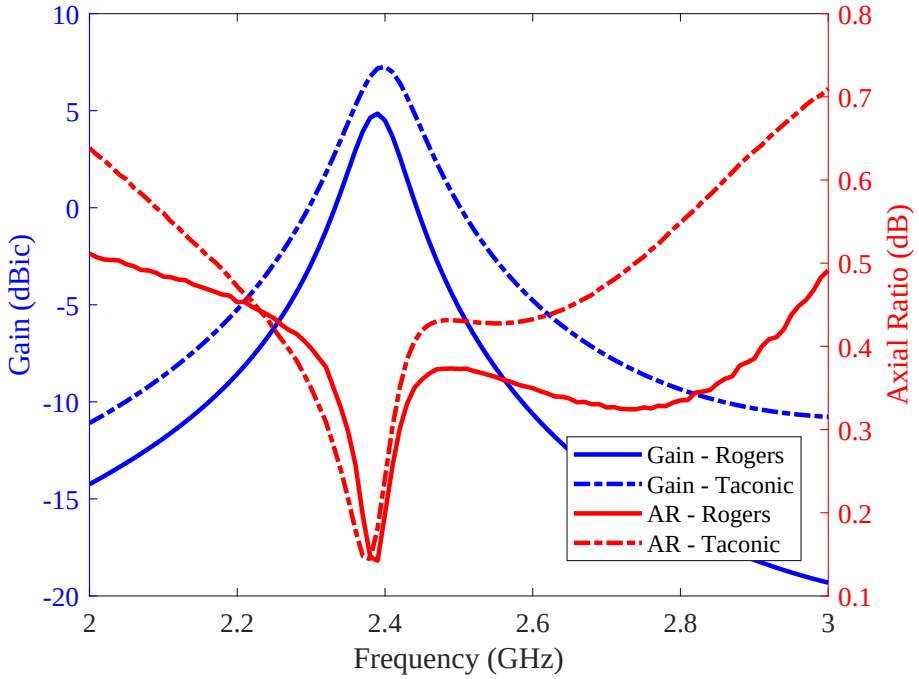

Figure 3.5: Simulated realized gain and axial ratio versus frequency considering radiation at broadside. Rogers substrate: $\varepsilon_r = 6.32$, $h = 1.27\,\text{mm}$ and $\tan\delta = 0.0027$. Taconic substrate: $\varepsilon_r = 2.18$, $h = 1.57\,\text{mm}$ and $\tan\delta = 0.0009$.

The 3-D pattern at 2.39 GHz of the proposed patch antenna is shown in Fig. 3.7, reaching 4.85 dBic at broadside and exhibiting a nice omnidirectional shape. Cuts for the realised gain and the AR at the E and H planes are shown in Fig. 3.8. These cuts demonstrate that the antenna performance in terms of CP versus beam angle, exhibiting a 180° AR beamwidth of less than 3 dB in both principal planes.

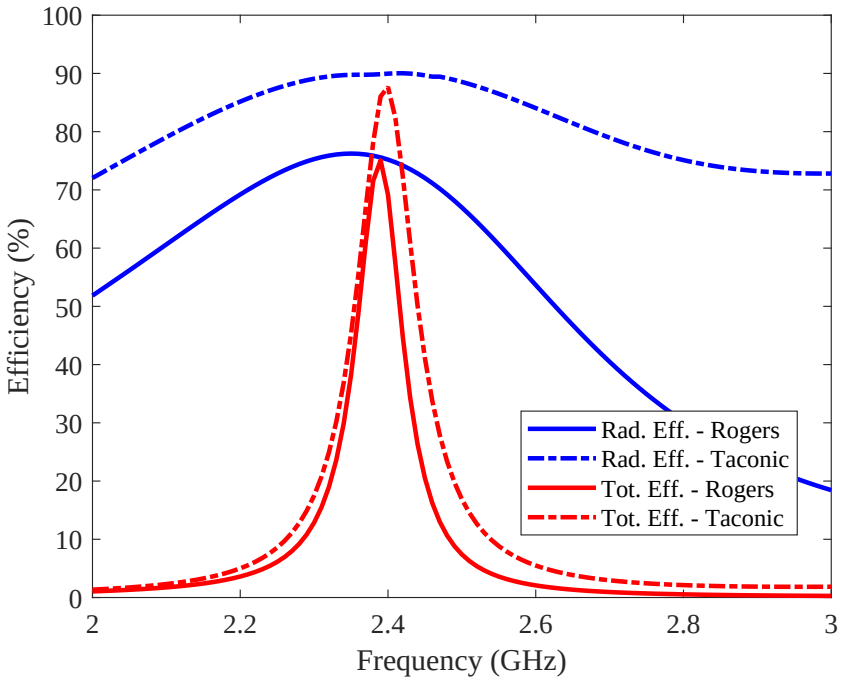

Figure 3.6: Simulated antenna efficiencies over frequency at broadside. Rogers substrate: $\varepsilon_r = 6.32$, $h = 1.27\,\text{mm}$ and $\tan\delta = 0.0027$. Taconic substrate: $\varepsilon_r = 2.18$, $h = 1.57\,\text{mm}$ and $\tan\delta = 0.0009$.

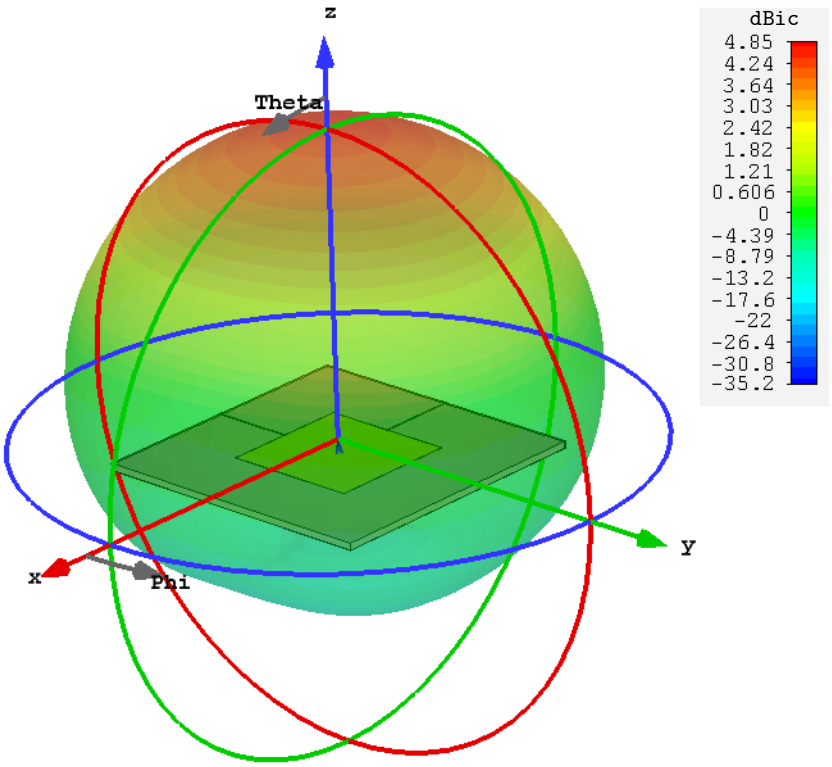

Figure 3.7: Radiation pattern (realized gain) in 3-D for the proposed array element (with Rogers substrate: $\varepsilon_r = 6.32$, $h = 1.27\,\text{mm}$ and $\tan\delta = 0.0027$) at 2.39 GHz.

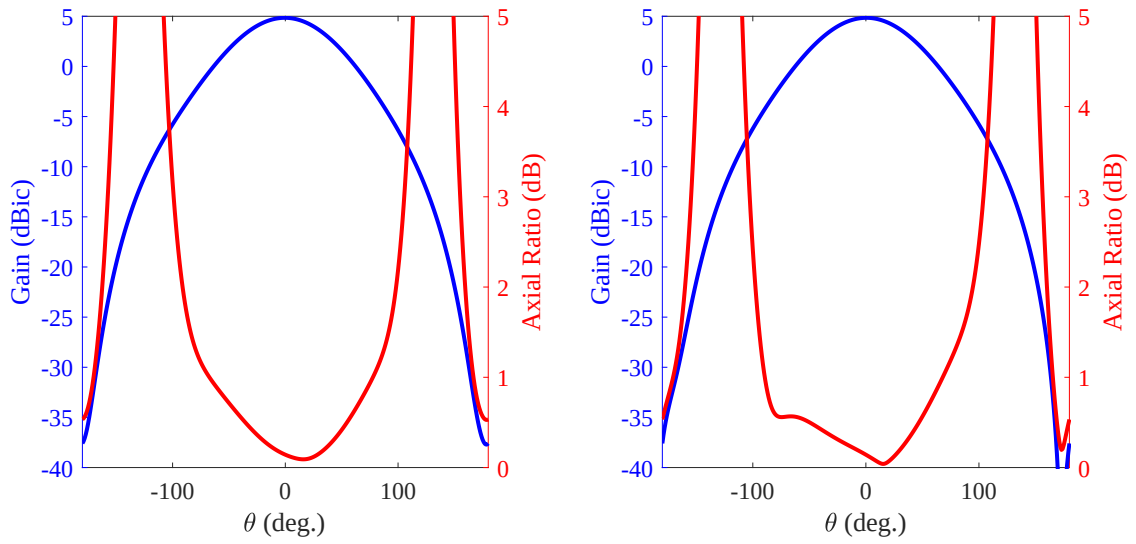

(a) (b)

Figure 3.8: Gain (blue) and axial ratio (red) at 2.39 GHz for $\phi = 0°$ (a) and $\phi = 90°$ (b) for the patch in Fig. 3.7.

3.3 Array feed system design

The proposed array has been designed in a series-fed fashion, for comparison with the network of sub-arrays employed in the RDA for WPT as explained in the previous chapter. In this new design, a common feed line will be used in order to save even more space between rows. Therefore, some amplitude and phasing feeding mechanisms must be applied to properly excite each antenna element. To do so, meanders (for phase control) and impedance transformers (for amplitude control) have been selected and are different for each of the four elements within the sub-array.

In order to achieve this desired amplitude and phase control, transmission lines with different widths and lengths were connected in series (see Fig. 3.1 for the yellow structure). But first, in order to better understand the theory and approach behind this feeding, a simple transmission line is connected to a basic antenna load, Z_A, as in Fig. 3.9(a). Therefore, the impedance that is seen from the input of a transmission line that is connected to the antenna, depending on the transmission line length and its characteristic impedance, is given by the expression 3.3.1,

$$Z_{in}(Z_0, l) = Z_0 \frac{Z_A + jZ_0 \tan \beta l}{Z_0 + jZ_A \tan \beta l} \tag{3.3.1}$$

where Z_{in} is the input impedance in ohms, Z_0 is the characteristic impedance of

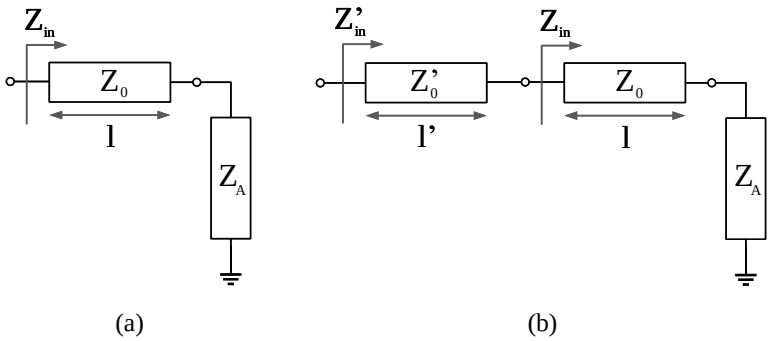

Figure 3.9: The use of additional impedance transformer transmission lines connected to a given load (Z_A) in order to get different input impedances, brings broader variety in the design of the feeding network: (a) one transmission line and (b) two transmission lines.

the transmission line connected to the antenna in ohms, l is its physical length in meters, Z_A the impedance of the antenna in ohms and β is the propagation constant in radians per meter ($\beta = \frac{2\pi}{\lambda_g}$).

The phase offset that a transmission line introduces into a given circuit is easily controlled by changing its length. Additionally, its characteristic impedance can be controlled by changing its width. The expression that relates the characteristic impedance of a microstrip transmission line (Z_0) and its width (W) is shown in equation 3.3.2 [4],

$$Z_0(W) = \begin{cases} \frac{60}{\sqrt{\varepsilon_{eff}}} \ln\left(\frac{8h}{W} + \frac{W}{4h}\right) & when \quad \frac{W}{h} < 1 \\ \frac{120\pi}{\sqrt{\varepsilon_{eff}}\left[\frac{W}{h} + 1.393 + \frac{2}{3}\ln\left(\frac{W}{h} + 1.444\right)\right]} & when \quad \frac{W}{h} \geq 1 \end{cases} \tag{3.3.2}$$

where h is the height of the substrate in meters and ε_{eff} is the effective dielectric constant, which can be interpreted as the dielectric constant of an homogeneous medium that equivalently replaces the air and dielectric regions of the microstrip line [5]. In other words, it can be considered as a relative average between the dielectrics of the air and the substrate with a higher order correction factor [6]. The expression to calculate it is shown in equation 3.3.3 [4],

$$\varepsilon_{eff} = \frac{\varepsilon_r + 1}{2} + \frac{\varepsilon_r - 1}{2} \frac{1}{\sqrt{1 + 12\frac{h}{W}}} \tag{3.3.3}$$

where ε_r relates to the relative dielectric constant of the substrate.

Therefore, by changing the width and length of such transmission line, the power directed to each element can be controlled. Additionally, the use of cascaded transmission lines brings a broader variety of input impedances. When using just one transmission line 3.9(a), the range of possible input impedances, depending on the characteristic impedance of the transmission line and its length, is more limited. On the other hand, if an additional line is cascaded as in Fig. 3.9(b), the degrees of freedom of the possible impedances increase. This is shown in equations 3.3.4 and 3.3.5

$$Z'_{in}(Z'_0, l', Z_{in}) = Z'_0 \frac{Z_{in} + jZ'_0 \tan\beta l'}{Z'_0 + jZ_{in} \tan\beta l'} \tag{3.3.4}$$

and substituting 3.3.1 in 3.3.4,

$$Z'_{in}(Z'_0, l', Z_0, l) = Z'_0 \frac{Z_0 \frac{Z_A + jZ_0 \tan \beta l}{Z_0 + jZ_A \tan \beta l} + jZ'_0 \tan \beta l'}{Z'_0 + jZ_0 \frac{Z_A + jZ_0 \tan \beta l}{Z_0 + jZ_A \tan \beta l} \tan \beta l'} \tag{3.3.5}$$

where Z'_0 and Z'_{in} have been shown in Fig. 3.9(b).

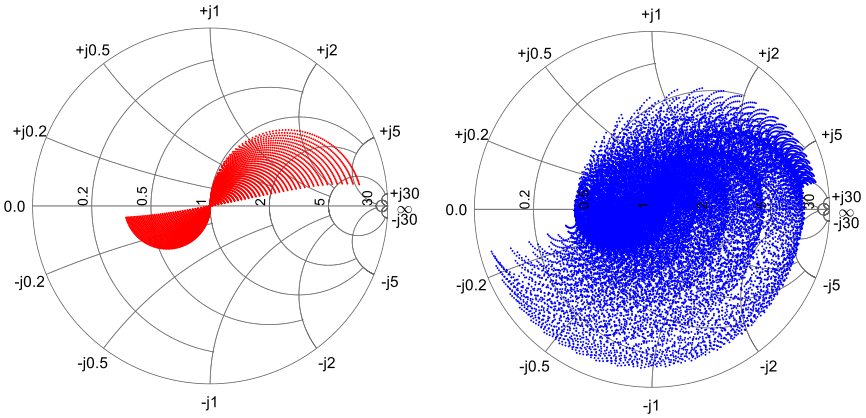

Figure 3.10: Input impedance seen for different lengths and widths of: (a) one transmission line and (b) two transmission lines that are connected to a given load ($Z_A = 50\,\Omega$ for this case). Variations of the length and width of these transmission lines are kept within a limit for a typical transmission line size given the frequency of operation.

In Fig. 3.10, the input impedances for one and two microstrip transmission lines are shown, respectively. The antenna impedance is considered to be $50\,\Omega$ and every point represents the input impedance for different lengths and widths of the transmission line that acts as the impedance transformer. The simple discontinuity in the width of this transmission line allows for the impedance transformation. In this way, if we want to make an analogy using water flow in pipes, every "tee" junction would be considered as a dividing pipe and the transmission lines on each branch would act as valves that control the water flow.

The range for the possible lengths and widths has been limited within typical values for a conventional microstrip line, considering that the frequency of operation is 2.4 GHz. Therefore, the possible range varies from 0.2 mm to 10 mm in width, and from 1 mm to 20 mm in length. Changes in width involves variations mainly

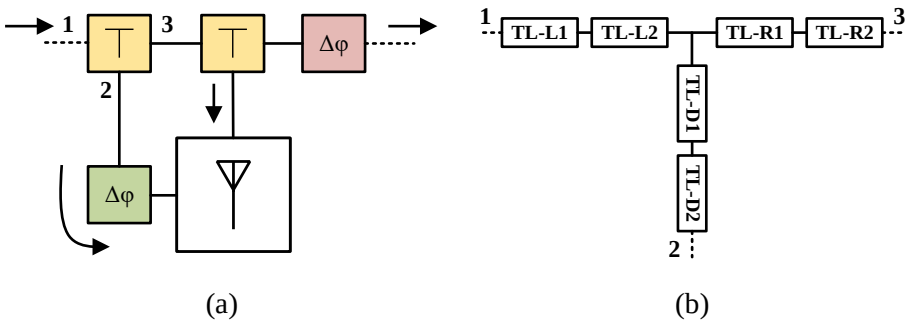

Figure 3.11: Feed system and antenna element of an array unit cell (a) and schematic of the proposed "tee" junction with double transmission lines on each branch (b).

in the characteristic impedance of the line, whereas changes on its length involves variations in the phase. It can be seen in Fig. 3.10 that by introducing an additional transmission line, it is possible to comprise a bigger area of the Smith chart, being easier to achieve a targeted amplitude distribution. A block diagram of the array unit cell and a schematic of the "tee" junction are shown in Fig. 3.11. The procedure to get the exact values for each of the transmission lines in the design is done by working backwards, from the terminating element, to the first one.

Firstly, amplitude balance was adjusted by optimizations in CST and right after, the length of the meanders was adjusted to find the desired phase balance. Finally, by a further optimization in CST, a very small refinement in the transmission lines was made to compensate for the small impedance variations that the changes in the meandered lines could generate. These impedance variations are very small because the width of the meanders' transmission lines remains constant which are the cause for big impedance variations. In this case, changes in length would just involve variations in the phase (moving in circles along the Smith chart) and not the magnitude (radius of the circle in the Smith chart).

Two meanders are needed on each unit cell. The first one (green box), controls the phase difference of the orthogonal modes that will be fed into each antenna element. It has been designed with a length that provides 90° of phase difference between them. The second one (red box), controls the phase difference between antenna elements. They have been designed with a specific length that provides equal phase on each antenna element. The purpose of this meander is to have the antenna elements closer together to avoid an increment of the SLL. A block diagram and a picture of the manufactured 4×1 sub-array are shown in Fig. 3.17. As it

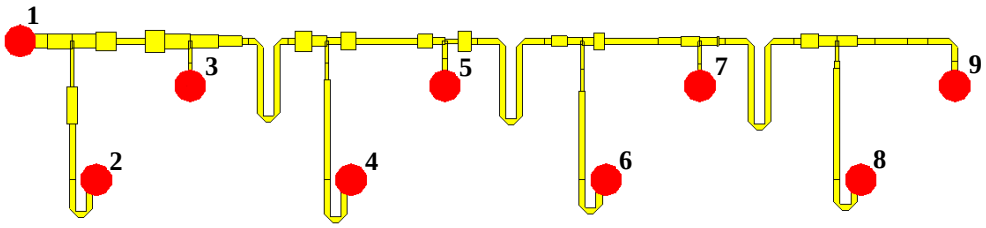

Figure 3.12: Feed system optimised in CST for a series-fed arrangement, CP radiation and uniform amplitude distribution is achieved by the use of meandered transmission lines and impedance transformers.

can be seen in the picture, the meanders responsible for the inter-element phase synchronization ensuring CP radiation are oriented in the $+y$ direction (as it is shown in Fig. 3.17(b)). The initial idea was to orientate them towards the $-y$ direction, as in Fig. 3.12, to make the design more compact but coupling issues arose between the meanders and the closest corner of the square patches degrading the axial ratio. However, if compared to the previous design (as in the last chapter), the spacing between antenna elements is smaller ($0.73\lambda_0 > 0.59\lambda_0$).

Regarding the amplitude distribution, uniform weights have been applied to each port of the array elements. To achieve this, different impedance transformers are located at the "tee" junctions so an equal amount of power is diverted to each of the branches. Fig. 3.12 shows the final optimised version for the feed system. Results in terms of amplitude and phase balances can be seen in Figs. 3.13 and 3.14, respectively. An ideal and uniform power split by eight would mean -9 dB to each port. In Fig. 3.13(b), the amplitude balance in frequencies around 2.4 GHz is within 1 dB, having therefore a worst case scenario of 1 dB of insertion losses. On the other hand, phase balance results shown in Fig. 3.14 exhibit good CP feeding to each of the patches (Fig. 3.14(a)) as well as good inter-element phase synchronization (Fig. 3.14(b)).

A diagram of one antenna element connected to the feed system can be seen in Fig. 3.15. "Left Tee" and "Right Tee" control the power distribution to the input of the antennas and also the power that continues towards the next antenna element. Each of the "*Tees*" are comprised of two independent transmission lines on each branch (L_1, L_2, D_1, D_2, R_1 and R_2). Moreover, the meanders have a constant width, which is W_0, and also include chamfered corners on each of the 90° turns in order to minimize potential reflections. This is because with no chamfering reflections are

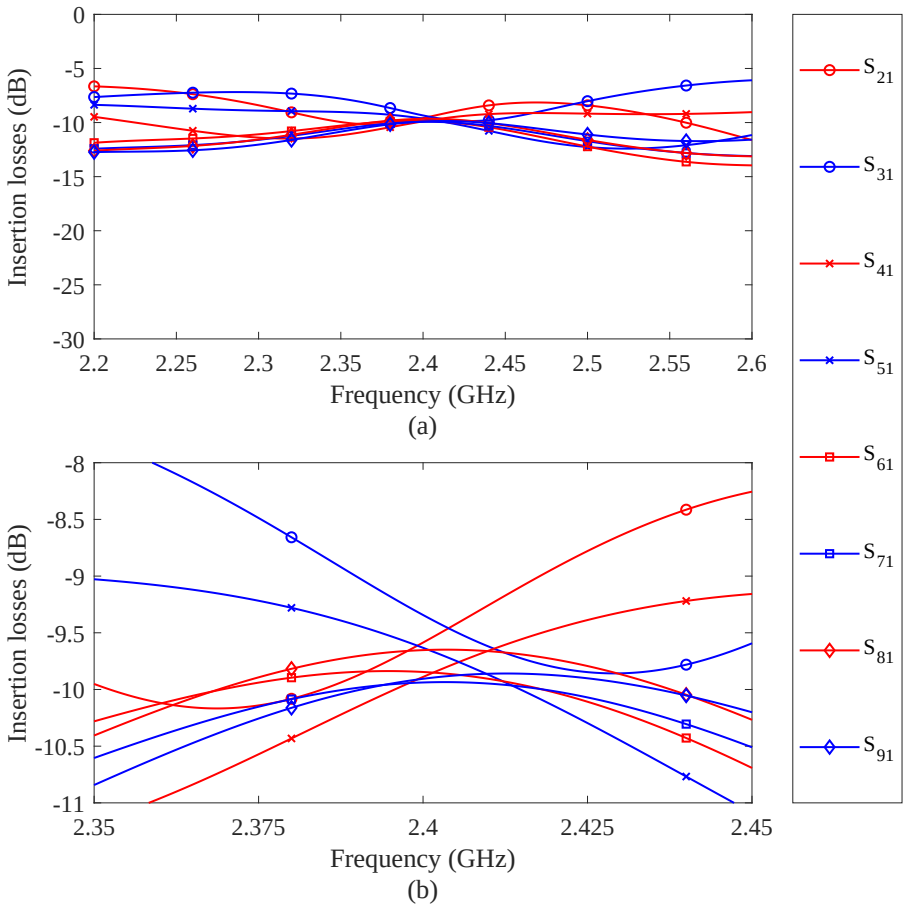

Figure 3.13: Simulated amplitude balance of the optimized feed system shown in Fig. 3.12: (a) S-parameter response and (b) zoomed view around 2.4 GHz.

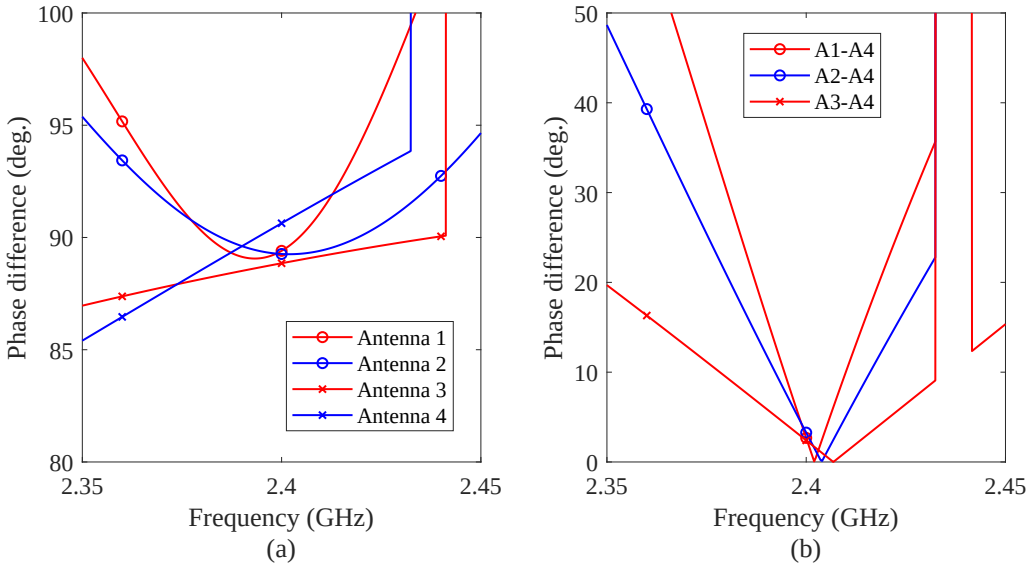

Figure 3.14: Simulated phase balance of the proposed feed system: (a) phase difference between the ports of the same antenna for CP radiation and (b) phase difference between antennas (phase synchronization).

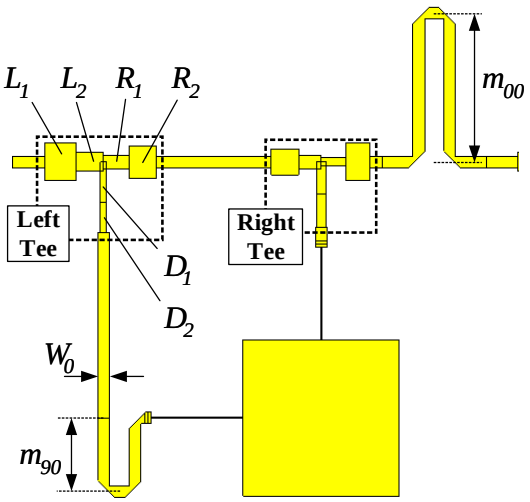

Figure 3.15: Schematic diagram of an antenna element within the series-fed array.

related to the capacitance that arises through additional charge accumulation at the corners of unchamfered microstrip bends, particularly around the outer point of the bend where the electric fields can have high values [7]. Therefore, the chamfered corner technique (see Fig. 3.16) in microstrip bends greatly reduces the effect of this capacitance and hence improves the matching. The expression, adapted from Easter *et al.* [8], that relates the chamfer deepness, b, with the width of the microstrip line, ω, is shown in Eq. 3.3.6,

$$1 - \frac{b}{\sqrt{2}\omega} \approx 0.6 \tag{3.3.6}$$

As it can be seen in Fig. 3.15, m_{90} corresponds to the length of the meander which controls of the phase offset between the antenna ports ensuring CP operation, whereas m_{00} corresponds to the length of the meander for phase synchronization

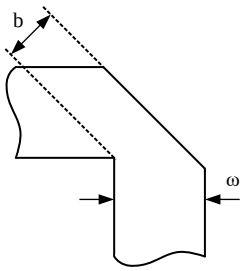

Figure 3.16: Chamfering of the 90° bends for the microstrip lines for matching improvement.

between all the antennas. It has to be mentioned that the length of the horizontal transmission line of all the meanders is fixed to 5 mm, being a compromise between compactness and reducing possible element coupling. All these variables can be found in Table 3.1. Also, by inspecting this Table, it can be seen that there are no values for the "Right Tee" in the last antenna element, given that all the power that reaches this point will go to the top port of the last antenna. Both the schematic and a picture of the manufactured prototype for a 4×1 series-fed sub-array are shown in Fig. 3.17. Moreover, a comparison study has been made in order to quantify the degradation in performance that the feed system introduces. In terms of radiation and total efficiency, it is shown in Fig. 3.18 that the radiation efficiency is degraded by around 8%. Regarding the total efficiency, the degradation due to the feed increases up to 9%. Additional comparisons can be seen in Table 3.2, which demonstrate that the proposed feed system has a low impact in terms of gain, directivity and 3dB beamwidth. Conversely, there is an improvement of 1.2 dB in the SLL.

Table 3.1: Dimensions (in mm) for the feed system (see Figs. 3.12 and 3.15)

	A_1				A_2				A_3				A_4			
	Left Tee		Right Tee		Left Tee		Right Tee		Left Tee		Right Tee		Left Tee		Right Tee	
	L	W	L	W	L	W	L	W	L	W	L	W	L	W	L	W
L_1	5.86	4.01	5.82	6.5	4.93	6	4.36	4.1	4.66	3	6.65	2.03	5.28	4.12	-	-
L_2	6.81	4.46	6.8	4.26	3.89	3.04	2.81	2.14	3.82	2.1	4.89	2.89	4.75	3.21	-	-
R_1	6.5	4	7.83	3.78	3.49	2.09	3.06	1.24	2.9	2.35	4.58	2.38	5.53	3.11	-	-
R_2	5.86	5.5	6.76	3	4.38	5.13	3.77	6	3.24	4.96	0.38	2.93	5	1.8	-	-
D_1	11	1	4.14	1	4.95	1	4	1.5	7	1	5.15	1	4.2	1	-	-
D_2	11	3	4.05	1	4.72	1	5.25	1.5	6.5	1	4.71	1	2	1.5	-	-
m_{90}	10				11.65				9.1				8.1			
m_{00}	20.87				21.6				23.33				-			
W_0	1.83															

Table 3.2: Comparison between the array with and without the series feeding system

Design	Freq. (GHz)	Realized Gain (dBic)	Directivity (dBic)	Rad. Eff. (%)	Tot. Eff. (%)	3dB BW (deg.)	SLL (dB)
Feed	2.37	9.66	12.6	56.9	50.5	22.1	-14
No feed		9.82	12.1	64.7	59.6	21.5	-12.8

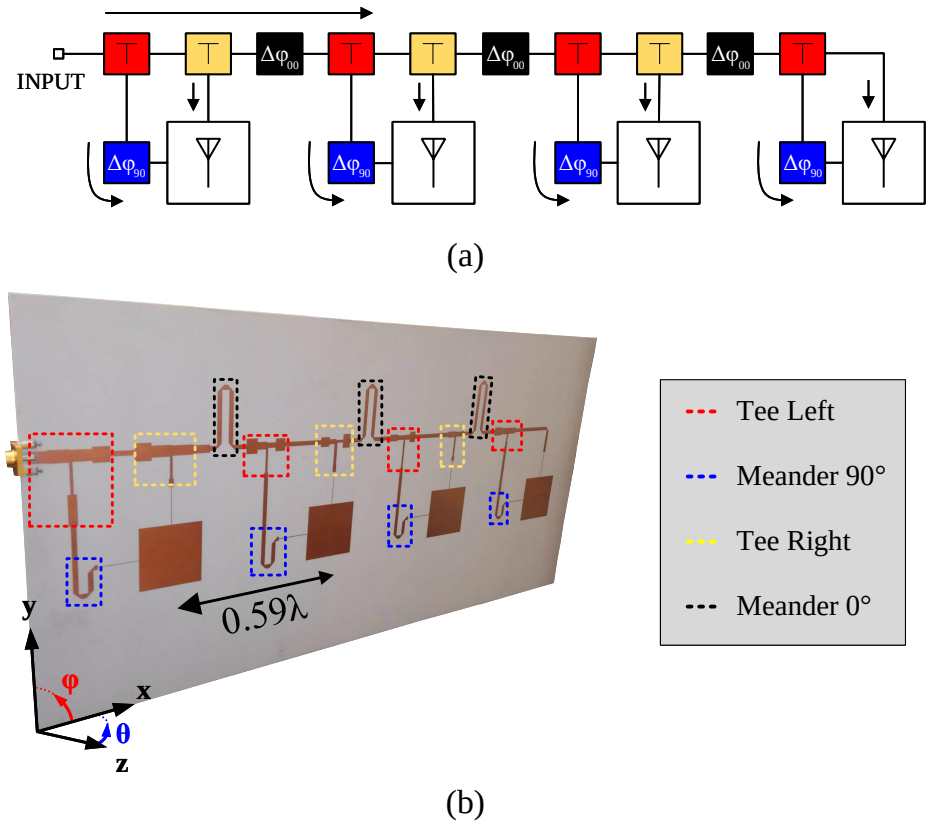

Figure 3.17: Block diagram (a) and picture (b) of the proposed sub-array design.

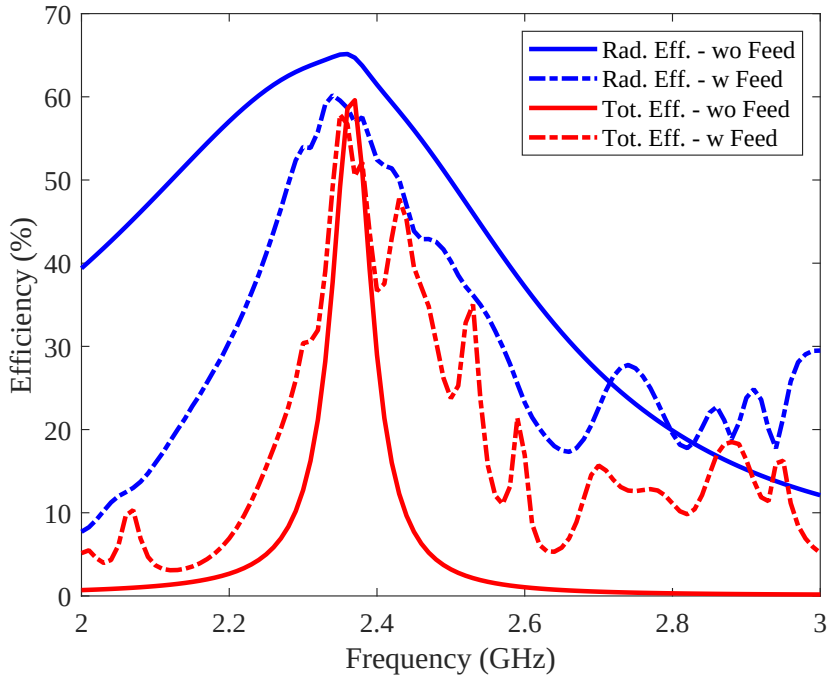

Figure 3.18: Radiation and total efficiencies of the array with and without the feed system.

3.4 Measurement results

Measurements and simulations of the return losses can be seen in Fig. 3.19, showing good agreement. There are additional peak resonances above the frequency of operation, however, only good radiation performance for the first resonance is achieved at about 2.35 GHz in terms of gain and AR. The frequency band of interest is zoomed in Fig. 3.19(b). Gain of the co-pol. and cross-pol. components over frequency are shown in Fig. 3.20, where a small shift in frequency of the cross-pol., due to a change in the dielectric constant, makes the lowest axial ratio shift also to around 2.38 GHz. Measurements of gain versus beam angle (check Appendix A.1) in both cuts ($\phi = 0°$ and $\phi = 90°$) are shown at three different frequencies. Figs. 3.21 and 3.22 correspond to the far-field planes at 2.4 GHz where the performance is not as expected given that in simulations the structure was optimized to work at this frequency. The cause for this is a frequency shift is related to the tolerance in the permittivity of the substrate. This is because after initial measurement of the return losses, new simulations were completed in order to readjust for the actual value of the relative permittivity. Results suggest it to be about 6.3; i.e. $\varepsilon_r \approx 6.3$, which is still within the substrate tolerance fixed by the manufacuter $\varepsilon_r = 6.15 \pm 0.15$. This explains why the maximum gain is at 2.37 GHz instead of 2.4 GHz. Additionally, Figs. 3.23 and 3.24 show good SLL of around -15 dB at 2.37 GHz, whereas Figs. 3.25 and 3.26 exhibit nice cross-pol. levels at 2.38 GHz.

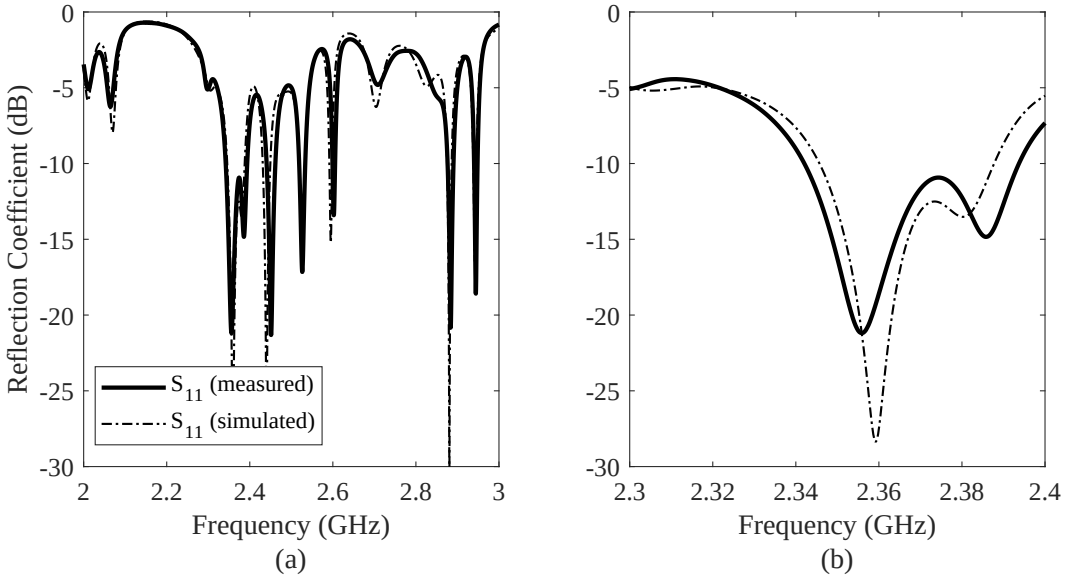

Figure 3.19: Reflection coefficient for the proposed series-fed array.

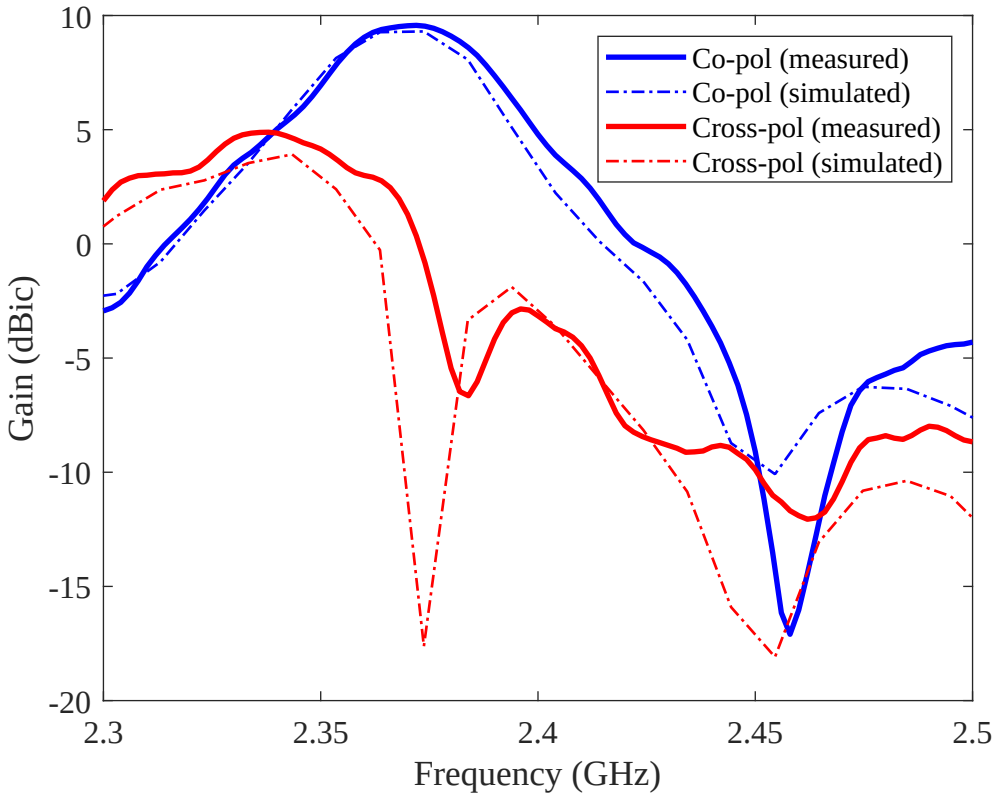

Figure 3.20: Realized gain over frequency for the co- and cross-pol. components for the proposed series-fed array.

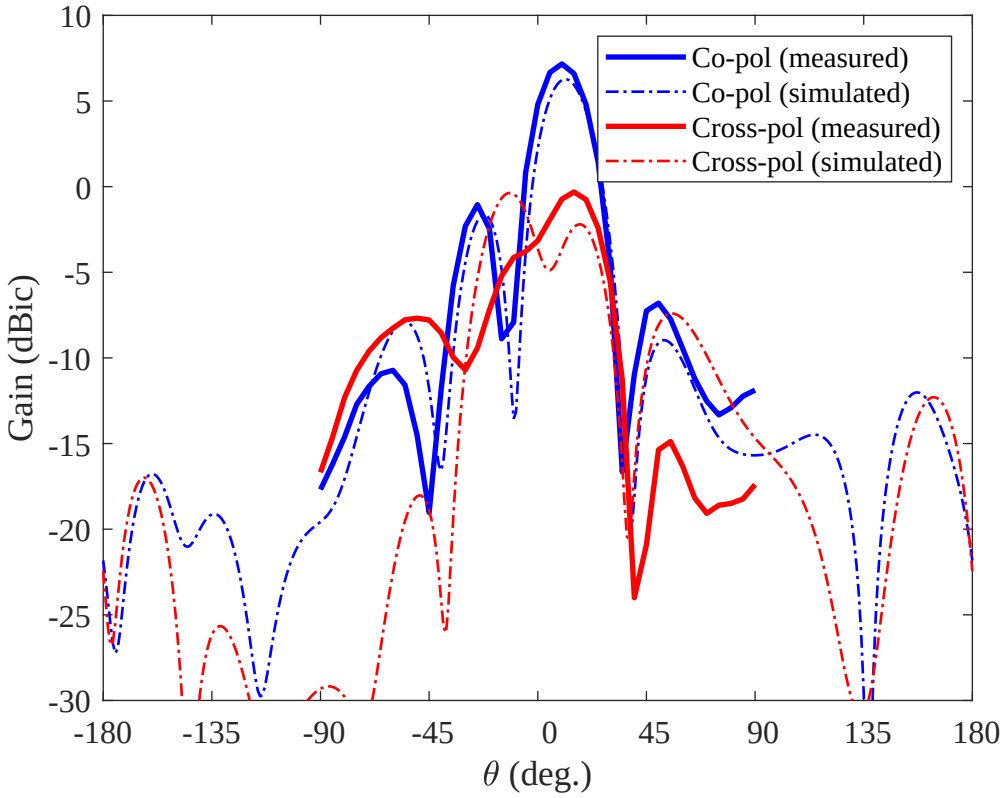

Figure 3.21: Realized gain versus beam angle at 2.4 GHz for $\phi = 0°$.

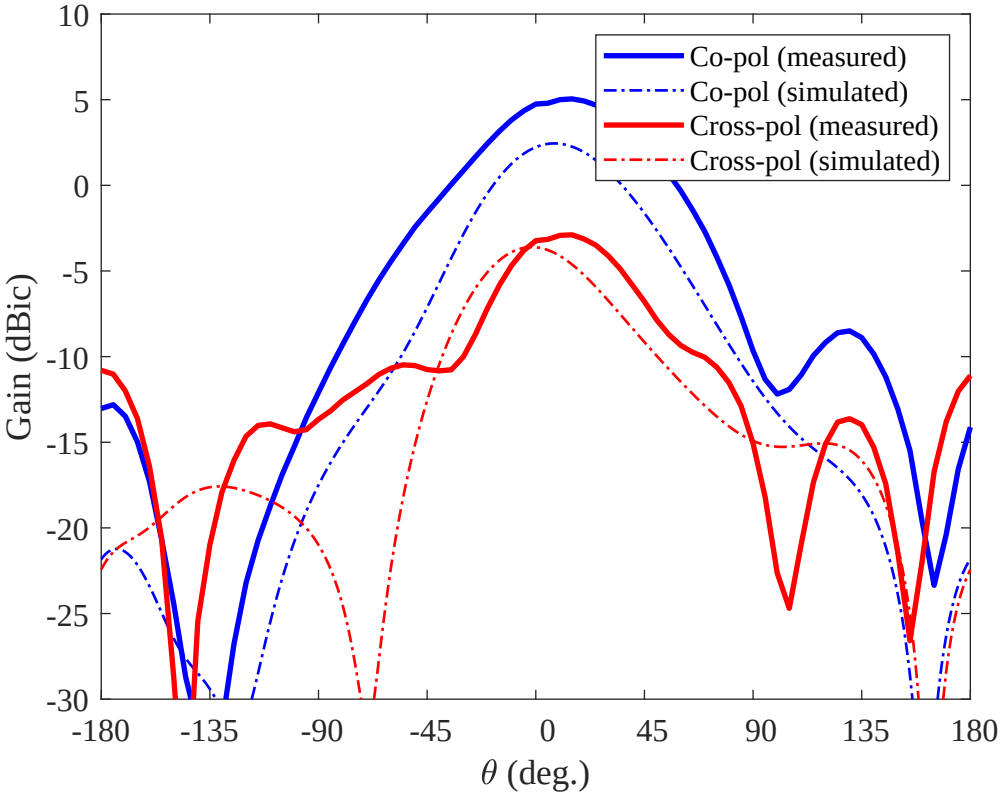

Figure 3.22: Realized gain versus beam angle at 2.4 GHz for $\phi = 90°$.

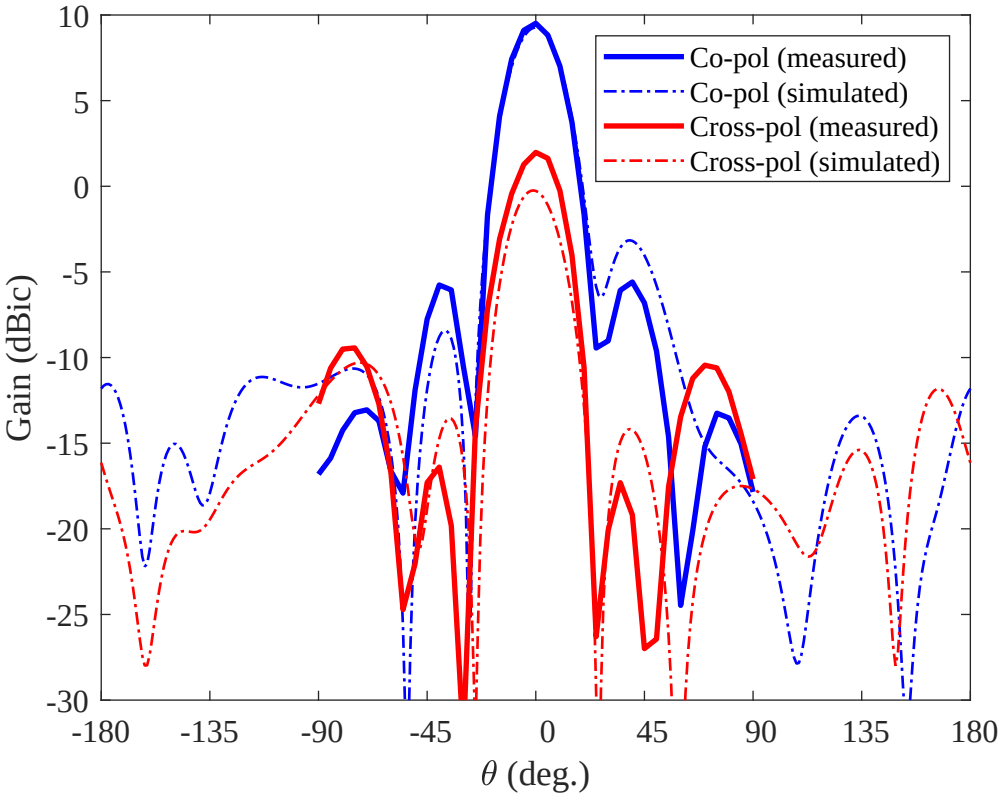

Figure 3.23: Realized gain versus beam angle at 2.37 GHz for $\phi = 0°$.

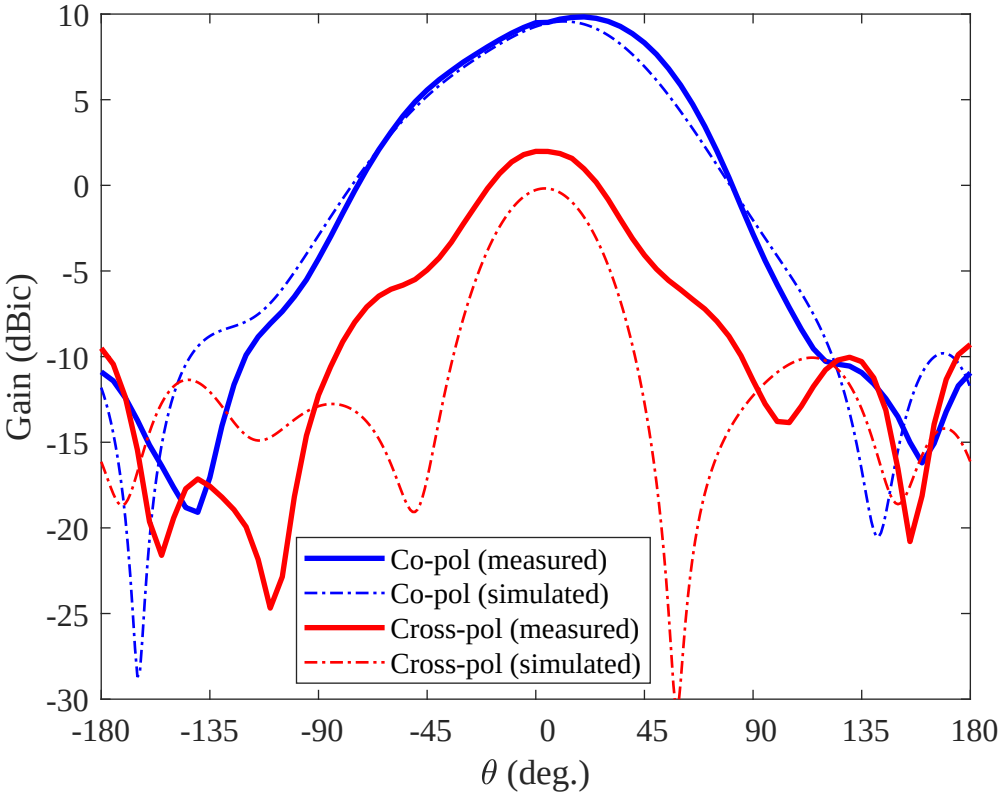

Figure 3.24: Realized gain versus beam angle at 2.37 GHz for $\phi = 90°$.

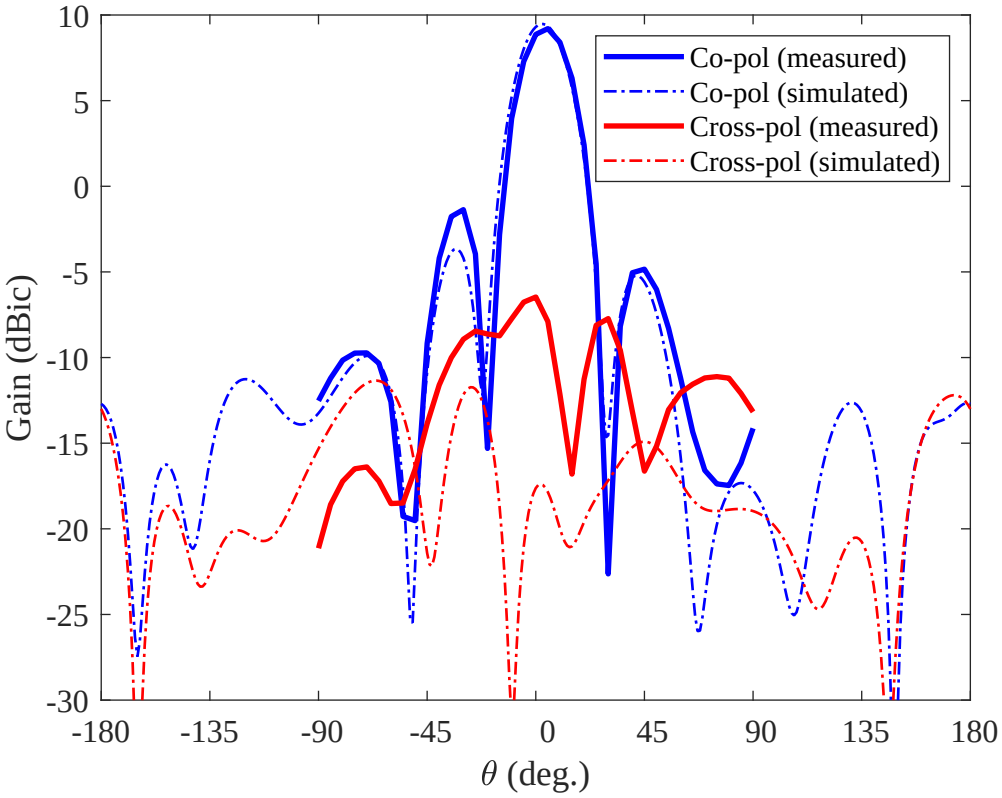

Figure 3.25: Realized gain versus beam angle at 2.38 GHz for $\phi = 0°$.

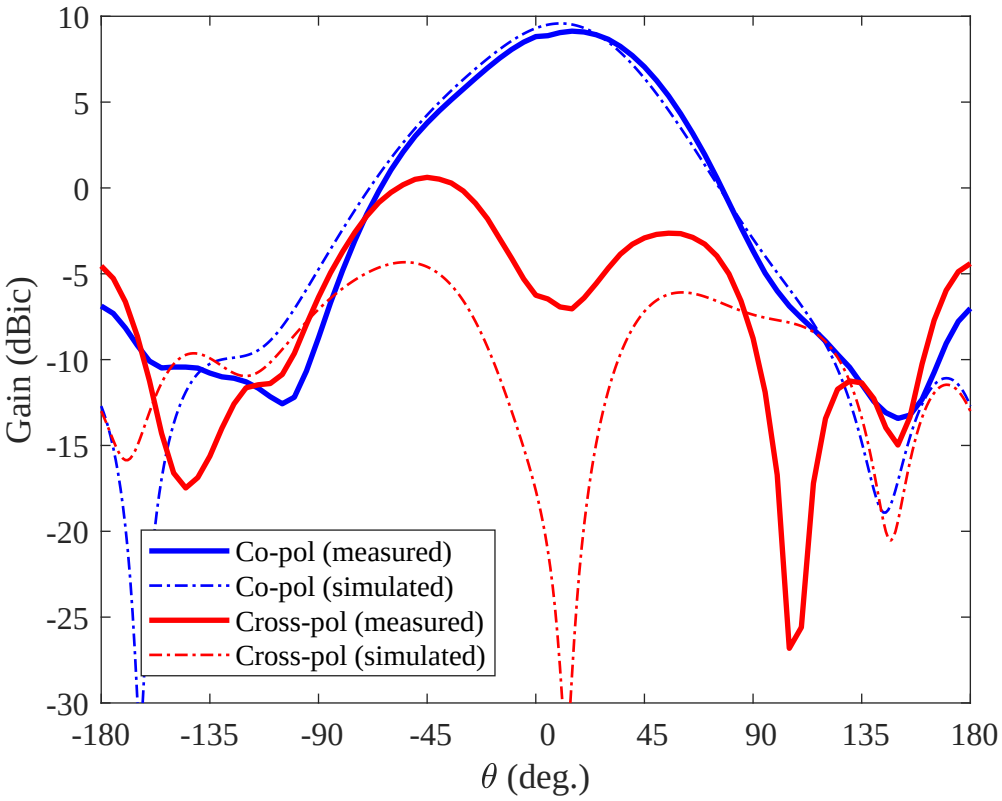

Figure 3.26: Realized gain versus beam angle at 2.38 GHz for $\phi = 90°$.

3.5 Comparison with other work

Thanks to the use of a higher dielectric material plus the use of meanders, the size of the new prototype is around 23 % smaller than the previous from the last chapter (see Fig. 3.1). Additionally, a comparison in terms of gain and SLL between the proposed SFA and the one introduced in the previous chapter is shown in Fig. 3.27. Given that the spacing between elements is shorter and the radiation efficiency of the single-element is lower (see Fig. 3.6), the total gain for the array is reduced by 3 dB. This can be overcome by introducing additional elements to the array. Additionally, the SLL is reduced by 3.5 dB only by the fact of having the elements closer together. Moreover, this can be improved even more by applying, for example, a Dolph-Chebyshev[1] distribution [9] instead of the uniform one. However, such distribution or any other (i.e. binomial[2] [10, 11]), which are mainly made to alleviate the SLL

[1] It can be considered as a mean of improving the pattern, by decreasing the SLL, of linear arrays in which the elements are fed in phase and are symmetrically arranged about the centre of the array. The amplitude distribution across the array is based upon properties of the Chebyshev polynomials.

[2] As in 1, but applying a different amplitude distribution across the array, which is according to the coefficients of the binomial expansion.

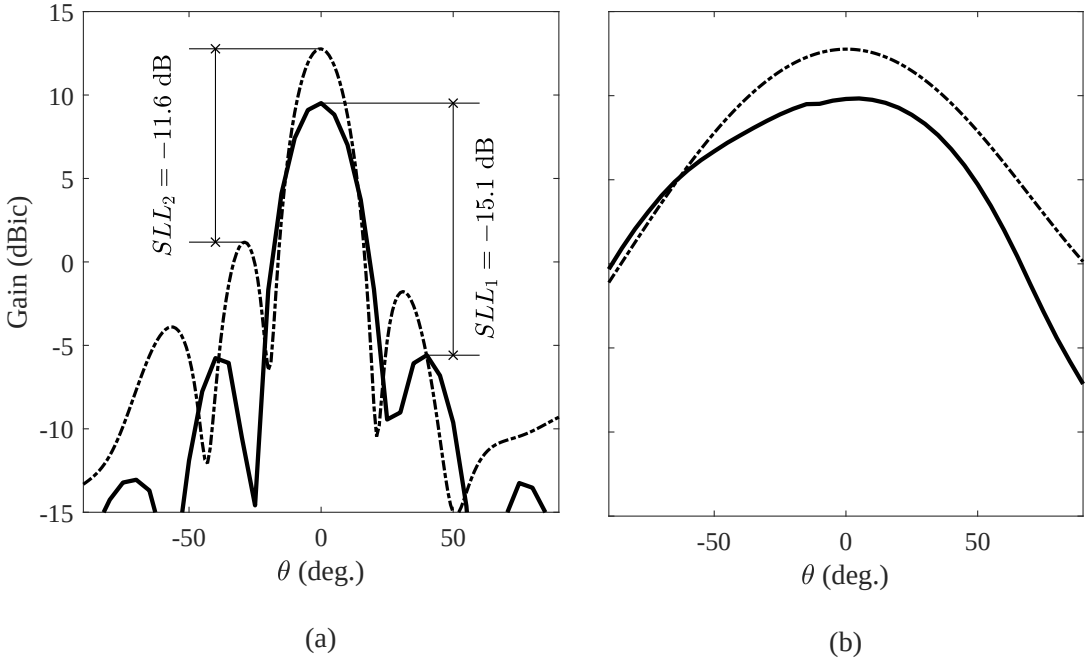

Figure 3.27: Realized gain and SLL comparison between the proposed series-fed array (continuous line) and the previous prototype (dashed line) for $\phi = 0°$ (a) and $\phi = 90°$ (b).

by amplitude tapering, were avoided due to the additional complexity of the feeding network that would be required.

The use of metamaterial transmission lines can also be used in the design of the feeding network as in [12] and [13], achieving a more compact design. However, these designs are LP and therefore no direct comparisons with the proposed design could easily be made. Also, a comparison with other works found in the literature that are CP, can be seen in Table 3.3. Although the bandwidth of the proposed array is very small, there are other features such as the AR and the SLL performance, that make this design suitable for many applications that do not require a broad bandwidth (i.e. WPT, radar or satellite communications). It also has to be mentioned that this SLL has been achieved by having a low-profile design, avoiding in this way complexity in the fabrication process of the array. From this perspective, the proposed design is a good alternative when looking for a simple design while achieving a low SLL.

Table 3.3: Comparison to Other Series-Fed CP Arrays Found in the Literature

	Array Type	Frequency (GHz)	Antenna Length (λ_0)	Element Spacing (λ_0)	Impedance BW (%)	Realized Gain (dBic)	3 dB AR BMW (deg.) $\phi = 0$ / $90°$	AR Minimum (dB)	First SLL (dB)	Single Layer or Multilayer	Aperture Control or Tapering
[14]	1×5	5.6	4.6	0.91	12	12.4	20 / -	2.2	-11	Single	Exponential
[15]	1×12	8	6	0.46	5	12.5	50 / -	3.9	-10.5	Single	Exponential
[16]	1×12	8	6	0.46	5	12	45 / -	1.1	-10.5	Single	Exponential
[17]	1×10	10.5	5	0.5	4	15.94	12.5 / -	2.5	-12.34	Multi	Exponential
[18][1]	1×24	260	11.2	0.42	3.85	15.32	25 / 50	1.27	-12.5	Multi	Exponential
[19]	1×4	17.5	3.4	0.68	7.4	9.36	110 / -	1.6	-13.5	Multi	Exponential
[20]	1×5	3	4	0.67	8.5	-	30 / -	0.2	-22	Single	Chebychev
[21][2]	1×8 SR	10	1.33	0.51	15	11.1	55 / 90	1.2	-11.5	Multi	Exponential
This work	1×4	2.37	2.4	0.59	1.8	9.8	40 / 64	2.3	-15.1	Single	Uniform

[1] Antenna results for [18] are based on simulations only. All other values in this table are defined by the fabricated arrays and measurements.

[2] This work, [21], is a circular array with sequential rotation (SR).

3.6 Conclusion

In this chapter, an alternative series-fed array design is proposed as an alternative to the one introduced in the previous chapter, achieving reduced SLL, mainly by having the antenna elements closer together and by presenting a reduction in the radiation pattern of the array element at the angle where the side-lobe is present. Also, in order to have the antenna elements closer, a substrate with a higher dielectric constant has been selected in combination with the use of meanders to increase the compactness of the design. Moreover, this novel design provides the flexibility of having CP radiation just with one port and also the possibility to apply different amplitude distributions by selecting the proper width and length for each of the impedance transformer sections. The loss of gain can be overcome by introducing additional antenna elements. Moreover, uniform amplitude distribution has been applied, but a Dolph-Chebyshev [9] or binomial [10, 11] distributions are also possible and they would improve even more the SLL. However, uniform distribution is preferred when aiming for simplicity in the design. The proposed feeding network is conformed by different transmission lines and by changing their length and width, they give us a broad variety of impedances that allow us to apply the desired amplitude distribution for radiation at each antenna element within the array. One of the points to be studied for a potential second prototype would be to have the meanders that control the inter-element phasing looking down, as in Fig. 3.12, in a way that does not perturb the axial ratio caused by the coupling, giving therefore more compactness to the design. Finally, a comparison with other works that are also designed in microstrip technology with CP radiation has been made showing a clear advancement (even over some of the multi-layer designs) when looking for a low-profile design and good SLL performance.

References

[1] S. L. Karode and V. F. Fusco, "Novel retrodirective beam formation techniques," in *1997 27th European Microwave Conference*, vol. 1, Sep. 1997, pp. 81–86.

[2] C. Balanis, *Antenna Theory: Analysis and Design*, 3rd ed. Wiley, 2015, ch. 14, pp. 859–864.

[3] D. Pozar, "Considerations for millimeter wave printed antennas," *IEEE Transactions on Antennas and Propagation*, vol. 31, no. 5, pp. 740–747, September 1983.

[4] C. Balanis, *Advanced Engineering Electromagnetics*, 1st ed. Wiley, 1989, ch. 8, p. 450.

[5] D. Pozar, *Microwave Engineering, 4th Edition.* Wiley, 2011.

[6] E. O. Hammerstad, "Equations for microstrip circuit design," in *1975 5th European Microwave Conference*, Sept 1975, pp. 268–272.

[7] T. Edwards, *Foundations for Microwave Circuit Design*, 4th ed. Wiley, 2016, ch. 9, pp. 236–239.

[8] B. Easter, A. Gopinath, and I. M. Stephenson, "Theoretical and experimental methods for evaluating discontinuities in microstrip," *Radio and Electronic Engineer*, vol. 48, no. 1.2, pp. 73–84, January 1978.

[9] C. L. Dolph, "A current distribution for broadside arrays which optimizes the relationship between beam width and side-lobe level," *Proceedings of the IRE*, vol. 34, no. 6, pp. 335–348, June 1946.

[10] S. J. Stone, "Directive antenna array," Patent 1 643 323, September, 1927.

[11] ——, "Antenna array," Patent 1 715 433, June, 1929.

[12] B. Ijaz, S. Roy, M. M. Masud, A. Iftikhar, S. Nariyal, I. Ullah, K. Asirvatham, B. Booth, and B. D. Braaten, "A series-fed microstrip patch array with interconnecting crlh transmission lines for wlan applications," in *2013 7th European Conference on Antennas and Propagation (EuCAP)*, April 2013, pp. 2088–2091.

[13] T. Kokkinos, A. M. Katsounaros, and A. P. Feresidis, "Series-fed microstrip patch arrays employing metamaterial transmission lines: A comparative study," in *The Second European Conference on Antennas and Propagation, EuCAP 2007*, Nov 2007, pp. 1–5.

[14] P. Hallbjorner, I. Skarin, K. From, and A. Rydberg, "Circularly polarized traveling-wave array antenna with novel microstrip patch element," *IEEE Antennas and Wireless Propagation Letters*, vol. 6, pp. 572–574, 2007.

[15] T. R. Cameron, A. T. Sutinjo, and M. Okoniewski, "A circularly polarized broadside scanning patch array," in *Proceedings of the Fourth European Conference on Antennas and Propagation*, April 2010, pp. 1–3.

[16] ——, "A circularly polarized broadside radiating herringbone array design with the leaky-wave approach," *IEEE Antennas and Wireless Propagation Letters*, vol. 9, pp. 826–829, 2010.

[17] J. Xu, M. Wang, H. Huang, and W. Wu, "Circularly polarized patch array fed by slotted waveguide," *IEEE Antennas and Wireless Propagation Letters*, vol. 14, pp. 8–11, 2015.

[18] X. Bai, S. Qu, and C. Chan, "Circularly polarized series-fed patch array for thz applications," in *2016 IEEE International Symposium on Antennas and Propagation (APSURSI)*, June 2016, pp. 595–596.

[19] K. Wei, J. Li, R. Xu, and G. Yang, "Circularly polarized omnidirectional microstrip antenna array," in *2017 IEEE International Symposium on Antennas and Propagation USNC/URSI National Radio Science Meeting*, July 2017, pp. 2315–2316.

[20] K. Ito, K. Itoh, and H. Kogo, "Improved design of series-fed circularly polarised printed linear arrays," in *IEE Proceedings H (Microwaves, Antennas and Propagation)*, vol. 133, no. 6. IET, 1986, pp. 462–466.

[21] Y.-H. Yang, J.-L. Guo, B.-H. Sun, Y.-M. Cai, and G.-N. Zhou, "The design of dual circularly polarized series-fed arrays," *IEEE Transactions on Antennas and Propagation*, vol. 67, no. 1, pp. 574–579, 2019.

Chapter 4

Millimetre-Wave FMCW Radar Enhancement by SIW Butler Matrix Beamforming

4.1 Introduction

Nowadays automotive radar technology is becoming a hot topic for collision avoidance and self-driving cars. The main challenge is to achieve high angular resolution while maintaining low detection processing time. Also, applying multiple-input-multiple-output (MIMO) techniques for radar has been under discussion over many years [1–4]. Although very high resolution can be easily achieved [5], processing time becomes an issue for this kind of application. For example, in [6] high resolution was achieved by employing MIMO in addition to the multiple signal classification (MUSIC) technique. Apart from MUSIC [7, 8], there are other super-high-resolution algorithms such as the minimum variance distortionless response (MVDR) [9], the estimation of signal parameters via rotational invariance techniques (ESPRIT) [10], maximum likelihood (ML) [7] and Capon [11], among others. However, these super-resolution algorithms are slow compared to the classic sum and delay beamformer [12]. In Figs. 4.1 and 4.2 it can be seen how important is to achieve a balance between both characteristics. In first instance, a coarse resolution can generate false targets in the line-of-sight for the trajectory of the car, i.e. when a pedestrian is walking on the sidewalk in a narrow street (Fig. 4.1(a)), or

even when the car is travelling through a tunnel. On the other hand, high resolution can generally require a considerably longer detection time (t_2), which can unfortunately allow for a life threatening situation as shown in Fig. 4.2(a). This chapter presents a radar system that combines the use of a butler matrix; i.e. a passive RF beamforming network in transmission with sum-and-delay beamforming at the receiver. In addition, a new signal postprocessing technique that is termed Pwr_+ is proposed to achieve high angular resolution while maintaining low processing times ($< 50\,\text{ms}$). In this way, false targets and life threatening scenarios can hopefully be avoided (see Figs. 4.1(b) and 4.2(b)) when the demonstrated radar system is implemented for collision avoidance and other automotive radar applications.

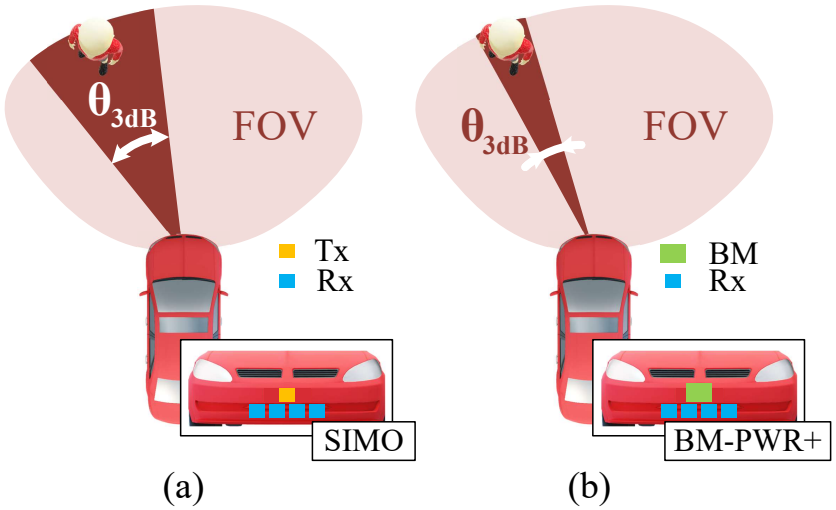

Figure 4.1: Illustrative comparison in terms of the angular resolution for a 1×4 single-input-multiple-output (SIMO) radar (a) and the proposed butler matrix combined with the *power plus* post-processing technique ($BM\text{-}Pwr_+$) (b).

In the recent past, the frequency of operation for the automotive radar industry has been 24 GHz, located in the unlicensed ISM band [13]. However, due to the low bandwidth availability at this frequency band (250 MHz), and spectrum regulations and the standards developed by the European Telecommunications Standards Institute (ETSI) and Federal Communications Commission (FCC), the use of this band will be phased out by 2022. Therefore, the regulating authorities have opened up frequencies for automotive radar in the 77 GHz band, that provides 4 GHz of sweep bandwidth against the 250 MHz that were available previously, enhancing resolution and reducing the size of the system [14]. Despite the aforementioned considerations, the selected frequency band for the developed frequency modulated continuous wave

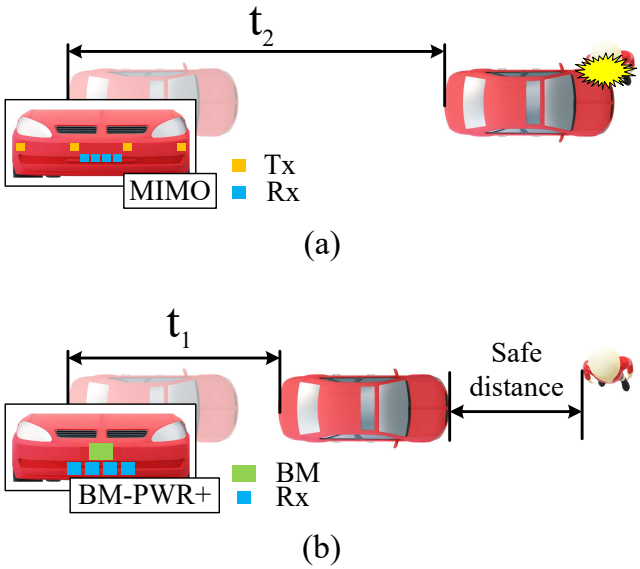

Figure 4.2: Illustrative comparison of the processing time for a 4×4 MIMO radar (a) with the proposed *BM-Pwr*$_+$ radar system (b).

(FMCW) radar in this chapter has been 24 GHz with a 250 MHz bandwidth. This research is justified in the fact that the equipment at these frequencies would be affordable in terms of cost, and the designed antennas, RF beamforming networks, and the supporting electronics could be scaled down in size to operate at 77 GHz.

4.2 General Radar Overview

Radar is widely known as an acronym for RAdio Detection And Ranging, but it has become a common noun over the years, losing its capitalization. It is considered a detection system that uses electromagnetic radio waves to determine the range, angle and/or velocity of objects. There is not an specific inventor for it, actually it has been conceived by an accumulation of the theoretical and practical advancements which grew massively during World War II (WWII) [15].

The basic principle on which radar operates is based on electromagnetic wave reflection. The radar transmitter sends out a signal to the domain of observation and the scattered echo from the target is collected by the receiver and processed to determine the target location. A box diagram is shown in Fig. 4.3 which depicts the most basic parts of a radar. The radar transmitter generates the signal to be radiated to the air by the antenna. In case only one antenna for transmit and

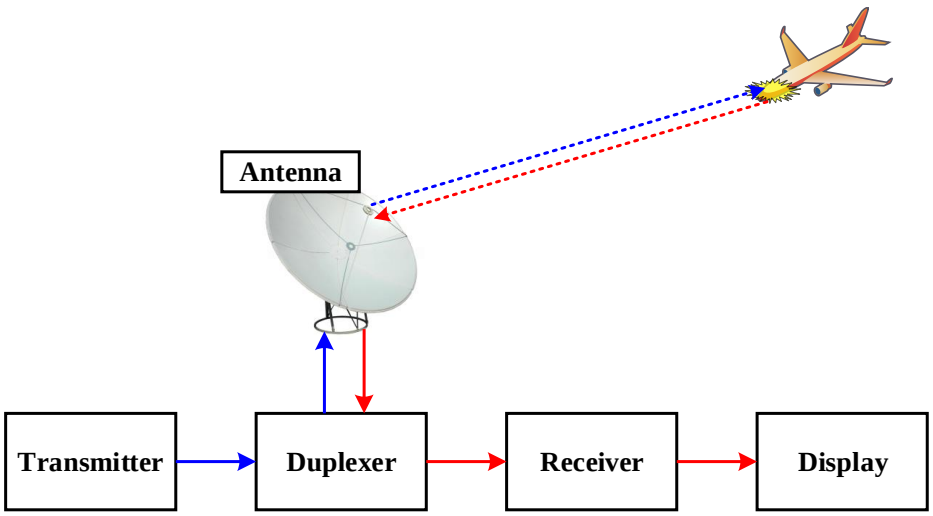

Figure 4.3: Illustration of a basic radar.

receive is used, a duplexer is needed to isolate tx and rx signal paths. The scattered signal from the target is received and processed in the receiver block, in order to obtain information about the target location (range and angle). The antenna will transfer the transmitter signal to the domain of observation. Depending on the radiation characteristics, this antenna sometimes is mechanically rotated, and this helps improve the field-of-view (FOV), which is the angular range that the radar will be able to cover, in case the antenna is not omnidirectional.

4.2.1 FMCW Radar

Pulsed radars are based on the concept of "transmit and listen". However, the wide bandwidth, costs, and high power requirements, and the fact that is not possible for pulsed radars to listen while transmitting makes FMCW more convenient for automotive applications.

FMCW radar, consists of a signal that is being transmitted continuously and periodically varies its frequency with time. Fig. 4.4 shows the waveform for this type of radar, with the corresponding equations that define them [16]:

$$B_{\text{sw}} = f_H - f_L$$

$$F_{\text{chirp}}(t) = \frac{f_L + f_H}{2} - \frac{B_{\text{sw}}}{\pi} \cdot \arctan\left[\cot\left(\frac{t \cdot \pi}{T_s}\right)\right] \tag{4.2.1}$$

$$A_{\text{chirp}}(t) = V_{\text{pp}} \cos\left(2\pi F_{\text{chirp}}(t) \cdot t + \phi_0\right) \tag{4.2.2}$$

where B_{sw} is the bandwidth (in hertz) of the generated chirp, being f_H and f_L its extreme frequencies; $F_{\text{chirp}}(t)$ corresponds to the function with respect to time that defines the chirp; T_{s} relates to the period of the chirp; $A_{\text{chirp}}(t)$ is the amplitude of the FMCW signal versus time; V_{pp} corresponds to the voltage *peak to peak* that the transmitter is able to produce (this is directly proportional to the maximum detectable range) and ϕ_0 relates to the initial phase of the FMCW signal.

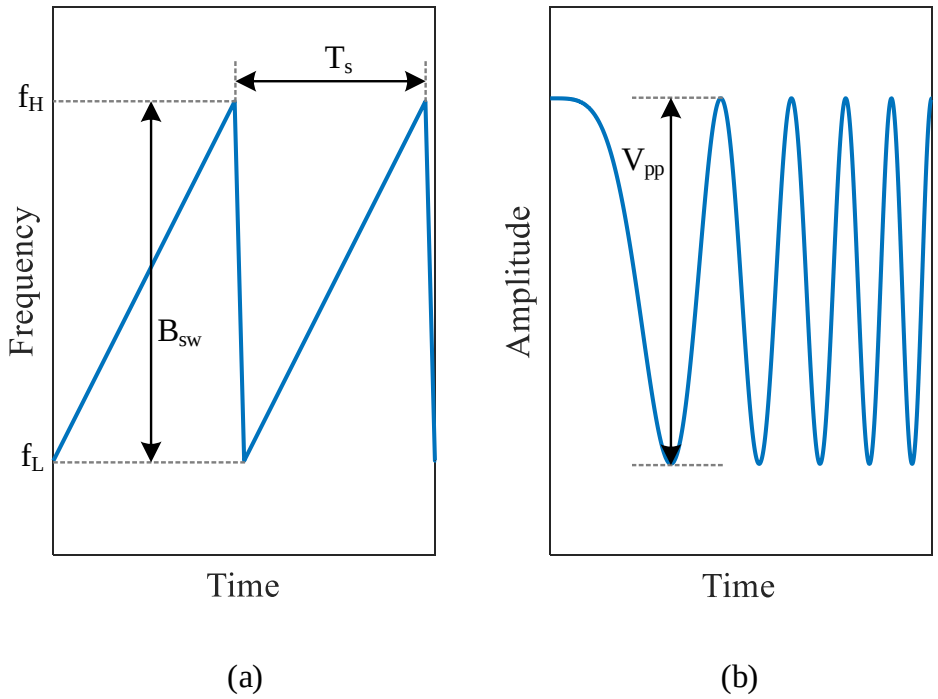

Figure 4.4: FMCW signal: two periods in frequency versus time format (see Eq. 4.2.1) (a), and one period in amplitude versus time format (see Eq. 4.2.2) (b).

The benefit for using frequency modulation for a continuous wave radar is that it is easy to calculate the range to the target, as shown in Fig. 4.5. The transmitted chirp signal (blue) is also feeding the LO port of the receiving mixer. The reflected chirp (red) is received back at the antenna and gets mixed in a downconverting mode with the original one, obtaining at the output of the mixer what is called *the beat frequency*, f_B, which is the frequency difference between the transmit and receive chirp signals. Now the range can be calculated by the use of the following equation [17]:

$$R = \frac{f_{\text{B}} \cdot c \cdot T_{\text{s}}}{2B_{\text{sw}}} \tag{4.2.3}$$

where R represents the distance from the radar to the target (in meters) and c is the speed of the light (in m/s).

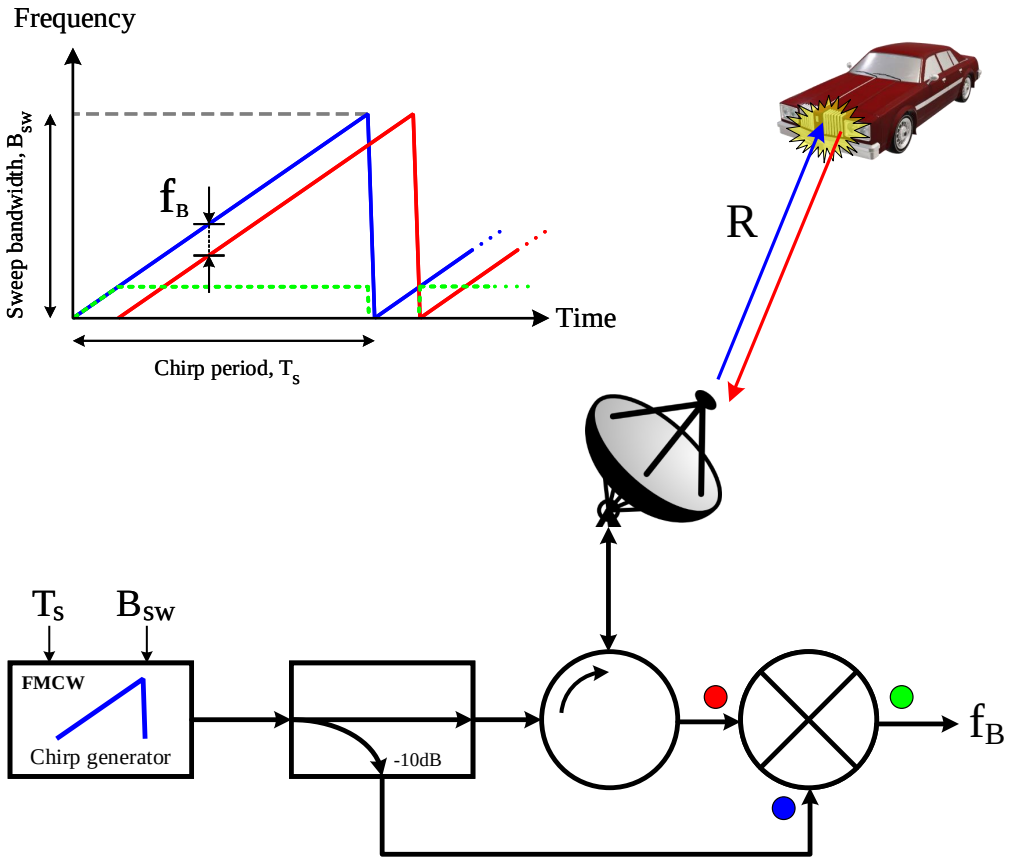

Figure 4.5: Range estimation on an FMCW radar, where f_B is related to the range, R by Eq. 4.2.3. A directional coupler is shown in the figure with a coupling of 10 dB.

4.2.2 Angle Estimation Basics

In order to get all the information about the target location, apart from the range, the angular position with respect to the radar also needs to be calculated. The most basic scenario that permits this calculation is shown in Fig. 4.6, where one transmit and two receive antennas are needed. This is also known as a one transmitter (1-tx) and two receivers (2-rx) *Single-Input-Multiple-Output* (SIMO) radar.

Therefore, as it has been already widely stated in the literature, the simplest case for a non-mechanical-motion-radar is a SIMO radar, formed by 1-tx and 2-rx, enabling the electronic phase scanning. For the case illustrated in Fig. 4.6, the incoming wavefront that has been reflected from a target arrives first to the receiver on the left given the angle of incidence, θ. For the second receiver, the wavefront will have to travel an additional $d \sin\theta$, which corresponds to a phase shift with

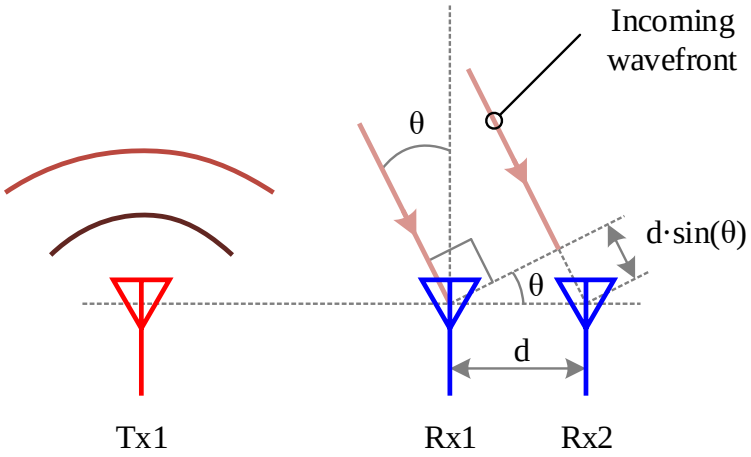

Figure 4.6: Angle estimation by using one transmit (1-tx) and two receive (2-rx) antennas (SIMO).

respect the first receiver of $\beta = (2\pi/\lambda)d\sin\theta$. By obtaining this progressive phase difference between receivers, it is possible to easily determine the angle of incidence of the reflected wave from the target with the following expression [18]:

$$\theta = \arcsin\left(\frac{\beta\lambda}{2\pi d}\right) \tag{4.2.4}$$

However, working with such a low number of receivers has its limitations: a coarse angular resolution which can be defined as the 3dB beamwidth of the receiver array. The simplest way to increase the angular resolution is increasing the number of receivers and/or increasing the distance between receivers, but also at the cost of grating lobes which limit the angular range or field-of-view for the radar. The expression that relates angular resolution with the number of receivers and the distance between them is the following [19],

$$\theta_{\text{RES}} = \arcsin\left(\frac{\lambda}{Nd}\right) \tag{4.2.5}$$

where λ is the wavelength of the signal, N is the number of receiving elements and d is the distance between them. Following such a rule for resolution enhancement, and this will increase the number of RF chains which will increase the costs of the improved radar. For example, if the number of receivers is incremented, this will increase the number of LNAs, mixers, IF-Filters and ADCs needed per receiver, increasing cost. Also, if the distance between receivers is increased, the corresponding

FOV would decrease by the appearance of grating lobes. Thus, the expression to obtain the FOV is derived from Eq. 4.2.4, considering that the extreme cases for the phase difference are π and $-\pi$, $\theta_{\text{FOV}} = \pm \arcsin\left(\lambda/2d\right)$.

4.2.3 MIMO radar

MIMO appears to overcome all these issues of poor resolution and high costs if a higher number of receivers is pursued. By increasing the number of transmitters a final virtual receiver array is synthesized with the rule $N_{\text{tx}} \times N_{\text{rx}}$. In terms of angular resolution, a 2×4 MIMO radar would achieve the same performance as a 1×8 SIMO radar, both depicted in Fig. 4.7. The simple idea behind MIMO radar is shown in Fig. 4.7(a), where the key concept lies in the spacing between both transmitters, which is N (the number of receivers) times the distance between consecutive receivers, Nd. Both transmitters are set to transmit sequentially in time, so that when the first one sends the radar signal and hits a given target, which is located at a given angular position with respect the radar (θ), the scattered signal induces a wavefront in return as the light red lines show in Fig. 4.7. The received signal sets the phase distribution $(0, \beta, 2\beta, 3\beta)$. Once the received signal has been stored, the second transmitter sends the radar signal (dark blue line). If compared to the first radar signal sent (dark red line), it exists a phase offset of 4β. This offset will contribute to the second half of the virtual receiving array $(4\beta, 5\beta, 6\beta, 7\beta)$. Once the returned signals for both halves of the array have been collected, the array is processed as one eight-element receiver array. Additionally, having the transmitters and receivers collocated would make the physical dimensions of the radar more compact. This would reduce the costs while maintaining high resolution, but the problem now arises on the processing time. Schematic examples of SIMO and MIMO radars are shown in Fig. 4.8(a-b), respectively.

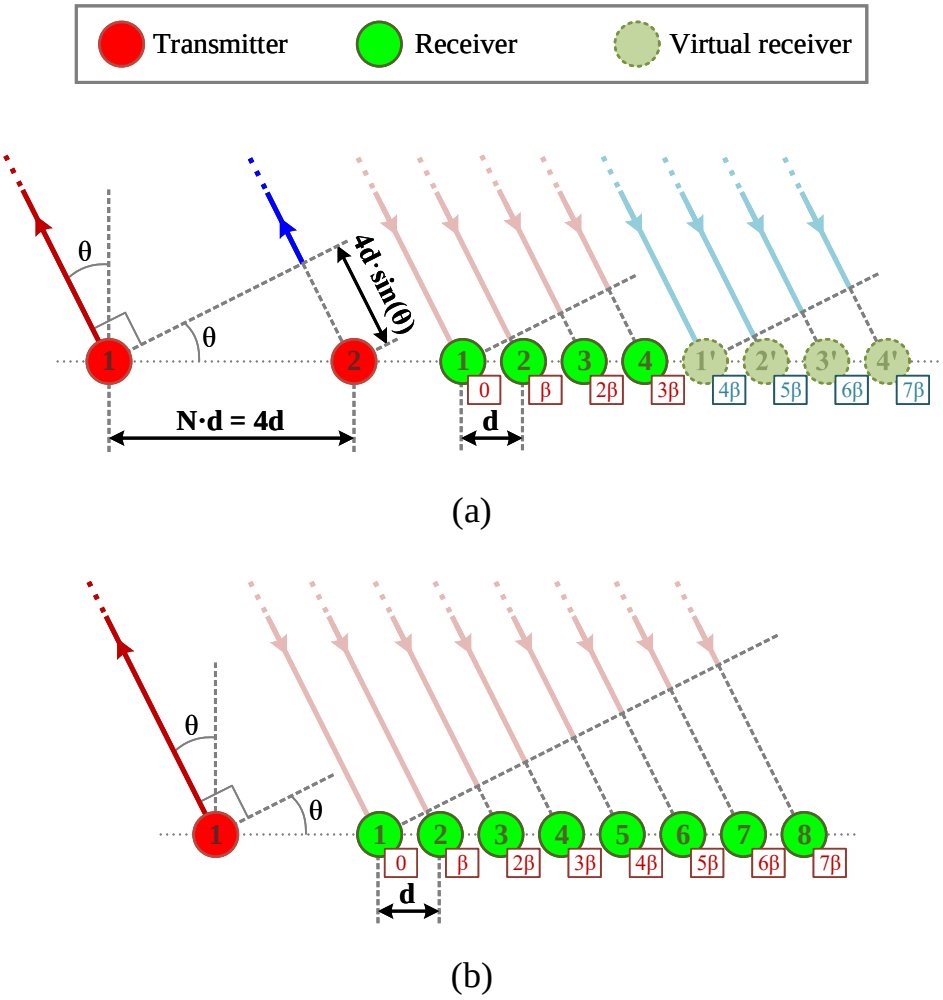

Figure 4.7: A 2×4 MIMO radar (a) and a 1×8 SIMO radar (b).

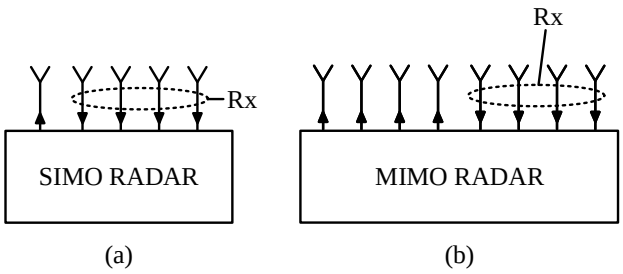

Figure 4.8: Illustration of conventional 1×4 SIMO (a) and 4×4 MIMO (b) radars.

4.3 Passive Beamforming Techniques

In addition to high angular resolution, a broad FOV is also an important requirement for automotive applications. By the use of fixed beamforming techniques the targeted FOV can easily be achieved by the premise of "*divide and conquer*". Therefore, an array of antennas in transmit will be considered as one transmitter, given that beamforming is not possible just with one antenna element. Such antenna ar-

rays, will be working on a finite number of discrete states determined by the phase distribution applied to each element. In this chapter, the proposed design is based on the *butler matrix* (BM) concept but there are others, such as the *blass matrix* [20], the *wullenweber array* [21] or using lens antennas.

4.3.1 Butler Matrix

The butler matrix (BM), firstly introduced by J. Butler and R. Howe in 1961 [22] and reaffirmed with a sistematic design procedure in 1964 by H. J. Moody [23], is considered a passive feeding network for antenna arrays that provides uniform amplitude distribution and constant phase difference between elements. It consists of N input and N output ports, being a requirement to be a power of 2 ($N = 2^n$; $n = 2, 3, ...$). The schematic for a 4×4 BM is depicted in Fig. 4.9, which shows the three types of components used: delay lines, crossovers and 90° hybrid couplers. Moreover, it is also possible to use 180° hybrids instead, that would involve a fewer number of delay lines required but its positions and magnitudes follow a more complicated patern [24]. Once N and n are determined, the number of phase shifters and hybrids can be easily obtained as shown in Table 4.1.

On the other hand, depending on which port is excited, the resulting weights applied to the array will induce a main lobe that will point towards a specific direc-

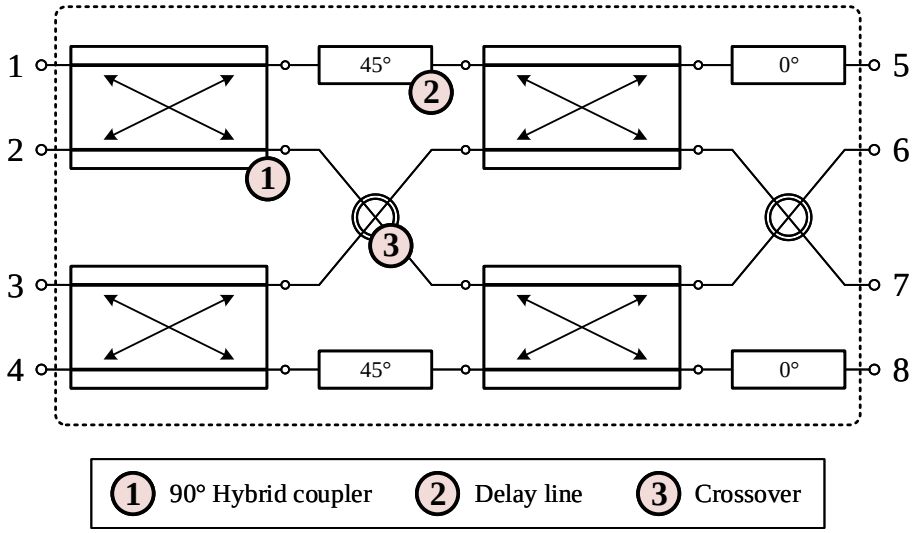

Figure 4.9: Schematic of a 4×4 BM.

Table 4.1: Number of hybrids and delay lines required for a $N \times N$ BM

Component	Rows	Columns	Total
Hybrid coupler	$N/2$	n	$n \cdot N/2$
Delay line	$N/2$	$n-1$	$(n-1) \cdot N/2$

tion (see Fig. 4.10). The output phase differences between consecutive ports and the corresponding direction of the induced main beams for a 4×4 BM are shown in Table 4.2. Regarding the delay lines connected at the top and bottom and in between the hybrids, they require a specific delay which is determined by N [23].

$$\phi_{\mathrm{dl}} = 90^\circ - \frac{1}{N}180^\circ = 45^\circ$$

However, the expressions to obtain this required phase delay for other N cases are different (i.e., when considering a BM with more than 4 input and output ports). For more details on more advanced BM design approaches see [23].

Table 4.2: Phase outputs on a butler matrix

Excited Port	[1]Output Phase (β)	[2]Beam Direction (θ_0)
1	+45	14.5°
2	-135	−48.6°
3	+135	48.6°
4	-45	−14.5°

[1] Phase difference between consecutive output ports (i.e. 5-6, 6-7 and 7-8).

[2] The expression that relates β and θ_0 is: $\theta_0 = \arcsin\left(\frac{\beta\lambda}{2\pi d}\right)$. For this table a spacing of $d = 0.5\lambda$ and a frequency of 24 GHz have been considered for the array.

4.3.2 Beamformer Design using Substrate Integrated Waveguide Technology

In order to make a proper selection of the technology to be used in the radar system that will conform the BM and the receiver antenna array, very basic technology has been considered in the first instance. Guided wave propagation in the microwave region is preferably obtained by using microstrip lines or metallic waveguides.

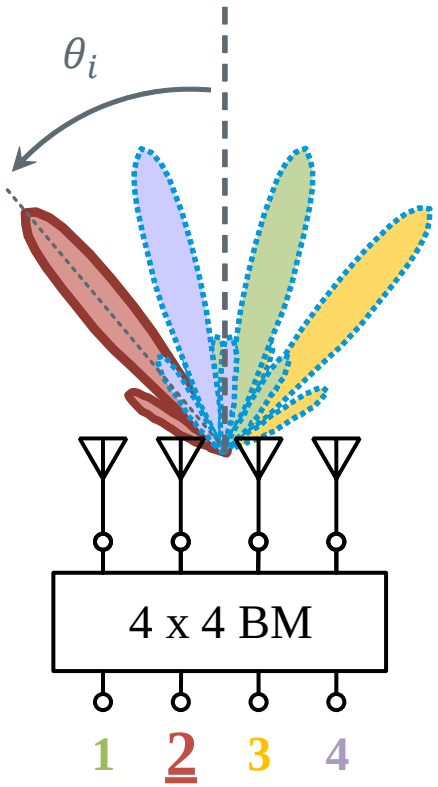

Figure 4.10: Linear array of 4 antennas connected to the output of a 4×4 BM and the resulting FF beams depending on the driven port.

In the case of microstrip, it is light, compact and has a very low fabrication cost. However, coupling losses can occur between adjacent lines. On the other hand, metallic waveguides provide low losses and outstanding isolation. The weak points for this technology are that they are bulky, expensive and they have difficulties with active component integration.

This is where substrate integrated waveguide (SIW) technology can provide some benefits over the previously mentioned technologies [25]. Actually it can be considered as a hybrid between microstrip and waveguide, actually taking the strengths of both. A very simple schematic is depicted in Fig. 4.11(a). SIW can be considered as a transmission line that implements rectangular waveguides in planar form. For instance, the SIW transmission line shown in Fig. 4.11(a), can be translated into a metallic waveguide with dimensions $a = w_{\text{eff}}$ and $b = h$, where h corresponds to the thickness of the substrate and w_{eff} depends on the parameters chosen in the SIW transmission line. The expression that relates these parameters is as follows [26],

$$w_{\text{eff}} = w - 1.08\frac{d^2}{s} + 0.1\frac{d^2}{w} \tag{4.3.1}$$

where w relates to the distance between the rows of metallic vias, d is the diameter of the via, and s corresponds to the distance, center-to-center, between adjacent vias. Additionally, in terms of the mode propagation only a TE_{m0} mode can exist, given that these modes are the only ones in which surface currents can flow parallel to the metallic vias. For other modes, by counterpart, the surface currents are cut by the gaps between vias preventing them from propagating [26]. Therefore, the cut-off frequency for the mode TE_{m0} in SIW structures is given by

$$f_{m0} = \frac{m \cdot c}{2w_{\text{eff}}\sqrt{\varepsilon_{\text{r}}}} \tag{4.3.2}$$

where c corresponds to the speed of light and ε_{r} the relative dielectric constant of the substrate. Therefore, the substrate height (b) will not affect the cut-off frequency for each of the propagating TE modes.

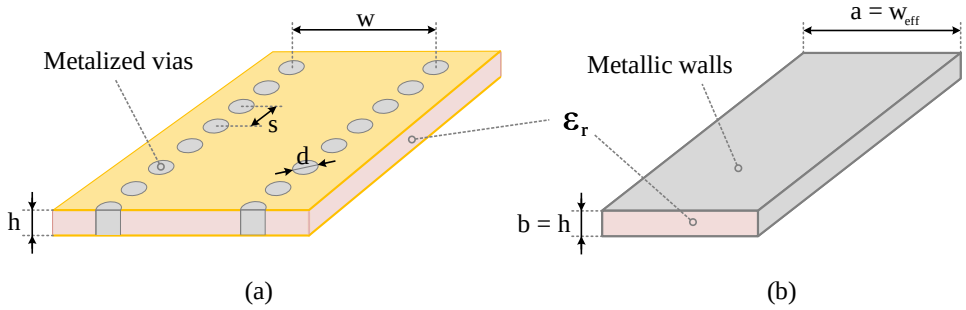

Figure 4.11: Section of an SIW transmission line (a), and its equivalent dielectric-loaded waveguide (b).

4.3.3 SIW Design Parameters

The expression for the propagation constant of the fundamental mode versus frequency is given by [27]

$$\beta_{\text{SIW}}(f) = \sqrt{\left(\frac{2\pi f \cdot \sqrt{\varepsilon_r}}{c}\right)^2 - \left(\frac{\pi}{w_{\text{eff}}}\right)^2} \tag{4.3.3}$$

In fact, by making both terms equal in eq. 4.3.3 the expression for the cut-off frequency shown in eq. 4.3.2 can be obtained.

On the other hand, as it has already been mentioned at the beginning of the chapter, the frequency range that the radar will be working at, is the ISM band which goes from 24 GHz to 24.25 GHz, with a center frequency of 24.125 GHz. Therefore, w_{eff} needs to be such that the SIW supports the fundamental mode TE_{10} for this frequency band. A very useful rule of thumb states that *"the accepted operating limits of waveguides, approximately are from* 125% *to* 189% *of the lower cut-off frequency"* [28]. Considering this and eq. 4.3.2, for a $w_{\text{eff}} = 5.984\,\text{mm}$, the corresponding cut-off frequency of the fundamental mode TE_{10} is 16.9 GHz as it is shown in Fig. 4.12. Following this rule of thumb, the SIW with the aforementioned effective width involves an accepted operating frequency range of $[21.125, 31.941]\,\text{GHz}$, which contains the targeted radar operating bandwidth.

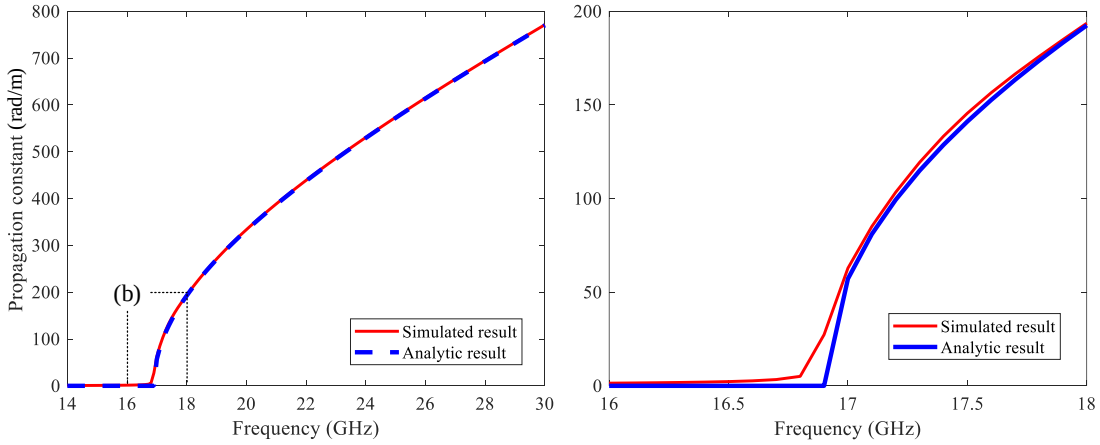

Figure 4.12: Propagation constant (β) for the fundamental mode TE_{10} (a) and zoomed around the cut-off frequency (b). Simulations in CST are shown in red while analytic results (eq. 4.3.3) are shown in blue.

Once w_{eff} is determined, the next step is to select one value for the ratios $s/d\,(=2)$ and $d/w\,(=0.08)$ such that they meet the requirement of $s/d \leq 2$ and $d/w \leq 0.2$, respectively [26]. Therefore, the diameter of the via can be obtained from a modified expression of eq. 4.3.1.

$$d = \frac{w_{\text{eff}}}{\left(\frac{d}{w}\right)^{-1} - 1.08\left(\frac{s}{d}\right)^{-1} + 0.1\frac{d}{w}} = 0.5\,\text{mm} \tag{4.3.4}$$

Finally, the width w and spacing between vias s can now be obtained

$$w = \frac{d}{0.08} = 6.25\,\text{mm} \qquad\qquad s = 2d = 1\,\text{mm}$$

4.4 Antenna Array Design

In [29], Elliott introduced an improved design procedure for small waveguide slot array antennas. However, for cases where the size of the waveguide width, a, is much bigger in comparison to its height, b, internal high order mode coupling increases significantly which was not taken into account in [29]. Therefore, in 1986, the publication of [30] included an updated revision that modelled these effects. Given that in SIWs $a \gg b$, the method demonstrated in [30] can be extrapolated for its use in this very popular technology. A simple schematic shown in Fig. 4.13 depicts the appearance of the two main types of SIW slot array antennas: travelling-wave [31] (a) and standing-wave [32] (b).

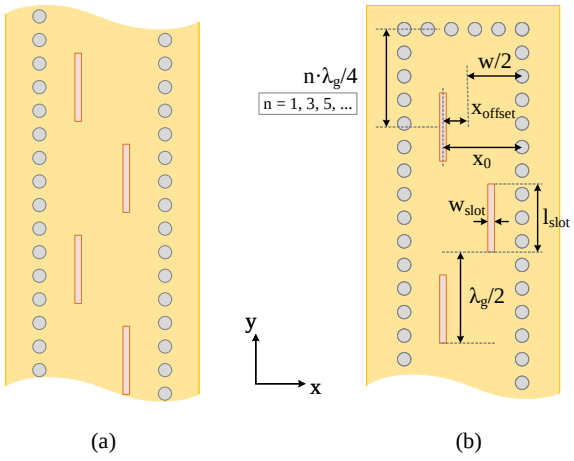

Figure 4.13: Top view of the two types of SIW slot antenna arrays: traveling-wave (a) and standing-wave (b). The bound wave for radiation propagates from the bottom to the top in (b).

The first one has more flexibility in terms of spacing between slots. By properly tuning this distance we have the ability to achieve a non-broadside main beam (frequency scanning array). For the second one, the spacing needs to be $\lambda_g/2$, making the radiation pattern strictly broadside and symmetric [33]. Additionally, for proper termination, the distance of the last slot to the transversal wall has to be equal to $\lambda_g/4$ or $3\lambda_g/4$ as it is depicted in Fig. 4.13(b).

Different displacement offsets for each slot from the axial center of the SIW in the x axis (x_{offset}), slot widths (w_{slot}) and lengths (l_{slot}), are tuned at each of the slots for cancellation of high order mode coupling. A good slot length approximation to start tuning from is given by Eq. 4.4.1 [34].

$$l_{\text{slot}} = \frac{\lambda_0}{\sqrt{2\left(\varepsilon_{\text{r}} + 1\right)}} \tag{4.4.1}$$

Given that the proposed antennas for the radar of this chapter are meant to work only in the azimuth plane, a standing-wave SIW slot sub-array configuration is the chosen one for the final design, with a sub-array size of 3×1. In addition, as it will be shown, having three slot elements (within each sub-array) provides a suitable antenna gain with a broad beam pattern in the azimuth plane or angular range of interest for the radar. As the 4×4 butler matrix provides 4 outputs, 4 sub-arrays are therefore needed for the final design, making a total array size of 4×3, as shown in Fig. 4.14. It has to be noted that the relevant dimensions from Fig. 4.13(b) which are dependent on the guided wavelength, λ_{g}, are slightly different to the values shown in the table from Fig. 4.14. This was caused by a hidden mistake in the calculations which went through the whole design and manufacturing process, because simulation and measurement results were acceptable. Therefore, for this case, dimensions are based on the freespace wavelength, λ_0 instead of λ_{g}. Also, common values for the slot lengths, widths and displacements (alternating left and right) have been considered for simplicity, given that these are individually tuned if a particular amplitude and phase distribution is required [29].

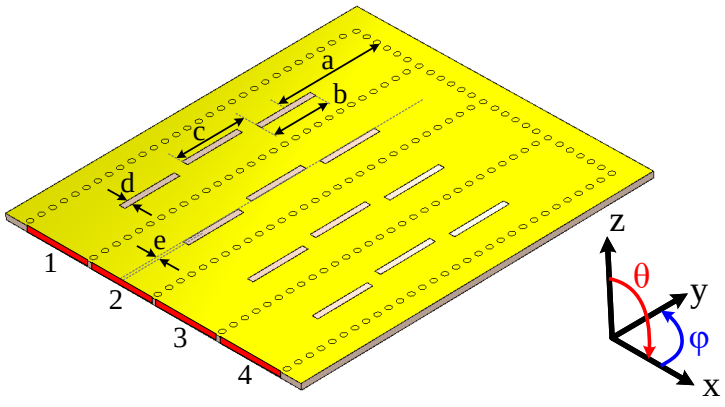

Parameter	Dimension [in mm]
a	9.28
b	4.89
c	6.10
d	0.54
e	0.28

Figure 4.14: Proposed SIW standing-wave slot antenna array, defined by four 3×1 sub-arrays.

Reflection coefficients at each port of the proposed SIW array are shown in Fig. 4.15(a), which exhibits an operational bandwidth of 7.25% (1.75 GHz) and covering, therefore, the 250 MHz of required bandwidth for the radar. One of the main reasons to use this type of antenna, apart from the ones aforementioned, is the decent bandwidth provided. This enables the possibility to scale the design up to the 77 GHz band for future radar designs and still cover the required 4 GHz band comfortably. Additionally, Fig. 4.15(b) shows the radiation and total efficiencies for the array. The total efficiency for the whole operating band is above 85% and it reaches values over 90% around 24.75 GHz. This behaviour improvement out-of-band is caused by the frequency shift of the active S-Parameters up to these frequencies.

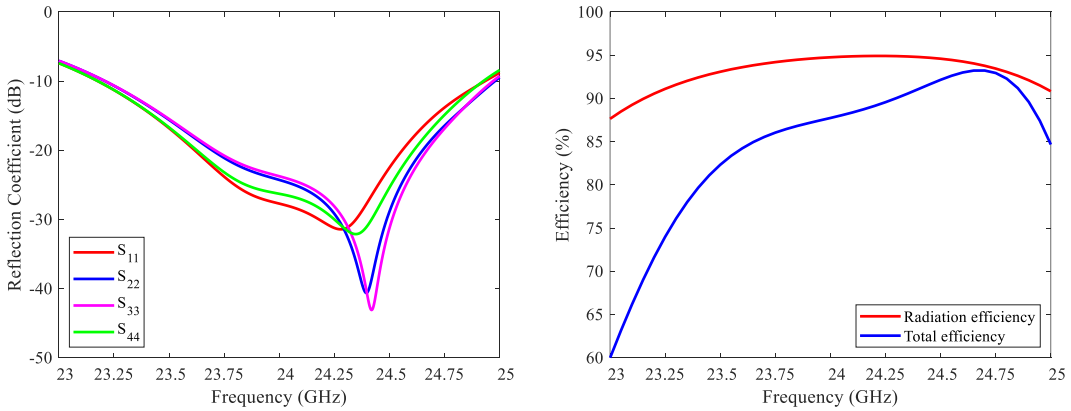

Figure 4.15: Simulated reflection coefficient (a) and radiation and total antenna efficiencies (b) for the 4×3 antenna array.

In terms of realized gain and pattern characteristics over frequency, simulated results can be found in Fig. 4.16(a) and (b), respectively. Realized gain values over 15dBi are achieved over the entire operating band. Moreover, it is important to check the main lobe direction for this kind of SIW series slot antenna array, given that the phasing at each slot will be different versus frequency, as the distance between them is always fixed. For this case, the main lobe direction (MLD) over frequency in both planes confirms that there is no significant beam scanning along the band of operation, of about 0.7° in the YZ plane ($\phi = 90°$), and it can therefore, perhaps, be neglected. On the other hand, sidelobe-level (SLL) values around -13 dB for the XZ plane and -23 dB for the YZ plane are achieved, confirming the good performance of the array.

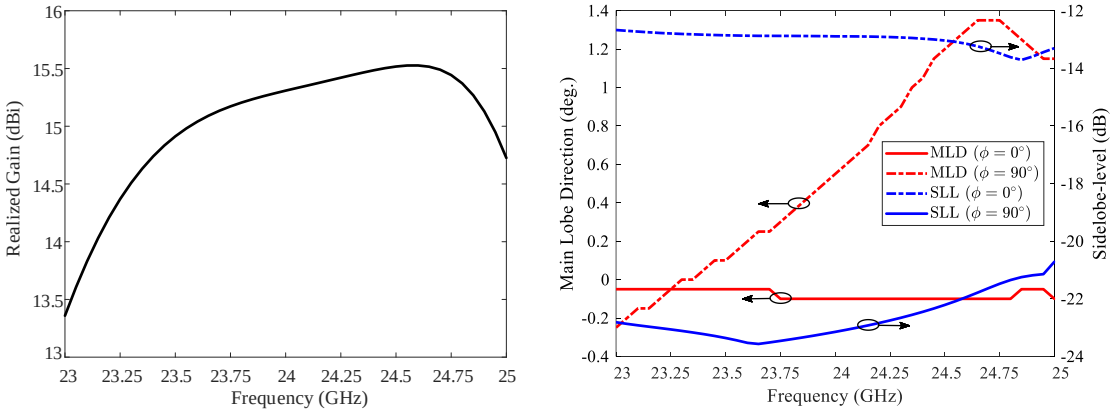

(a) (b)

Figure 4.16: Simulated broadside realized gain versus frequency (a) and sidelobe-level (SLL) and main lobe direction (MLD) versus frequency (b) for the 4×3 array.

Finally, E and H radiation pattern plots are shown in Fig. 4.17 for three different frequencies: the two extremes of the frequency of operation, and the middle one. It has to be noted that they stay almost the same which is the key for proper FMCW radar performance. Thus, all in all, these plots confirm the designed array as the chosen one to be implemented in the final radar system along with the butler matrix, which design will be described in the next subsection.

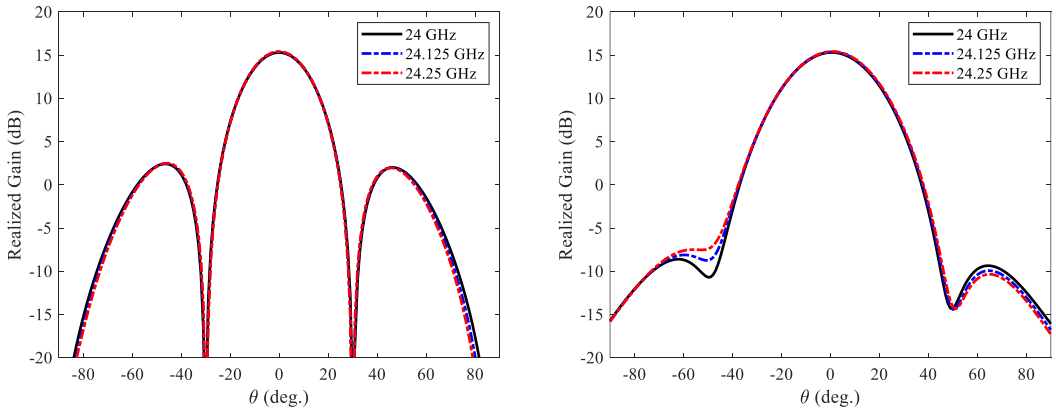

(a) (b)

Figure 4.17: Simulated realized gain versus angle at $\phi = 0°$ (a) and $\phi = 90°$ (b) for the 4×3 array at the extreme frequencies and the center frequency of 24.125 GHz.

4.5 Butler Matrix Design and Antenna Integration

As it has been shown in Fig. 4.9, the three components needed to build a 4×4 butler matrix are 90° hybrid couplers, delay lines and crossovers. Therefore, the first step in this design process is to build each component individually and test its correct operation.

Firstly, the hybrid coupler is based on Riblet's waveguide design from [35], which by the proper selection of the length, L (as shown in Fig. 4.18(b)), the power split through output ports 2 and 3 experiences a phase difference of 90°. Moreover, for an even power split and good matching, a proper selection of w_m must be considered [36]. Simulation results for this component are shown in Fig. 4.18, exhibiting low insertion losses in the operating bandwidth (around 0.2 dB), very high isolation (below 30 dB) and good output phase difference in the whole simulated bandwidth.

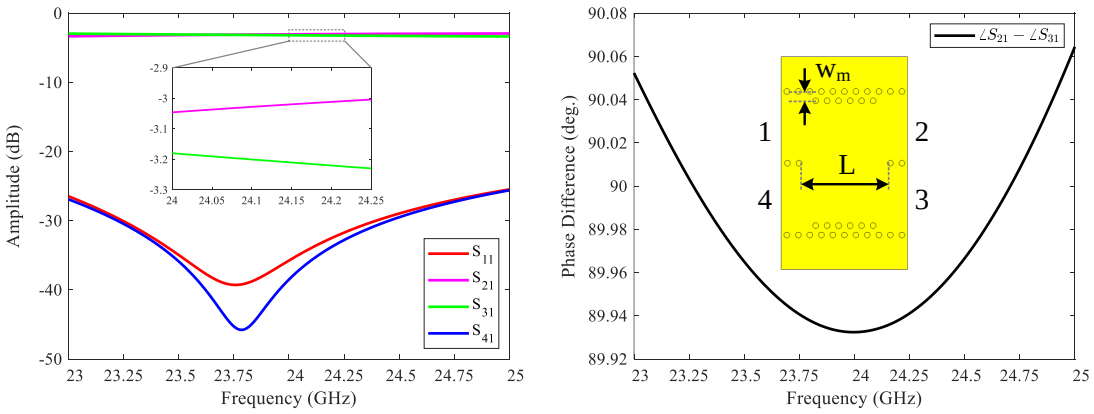

Figure 4.18: S-Parameters (a) and output phase difference between ports 2 and 3 if port 1 is excited (b). Also, a top view of the 90° SIW hybrid is shown in the inset.

For the design of the crossover two cascaded hybrids are used as in Fig. 4.19(a). This is possible given the split and combining characteristics of the 90° hybrid coupler: when port 1 is excited, at the two outputs of the first hybrid (red dashed square) there is a 90° of phase difference. Therefore, at the second hybrid the two ports are excited simultaneously making it to perform as a combiner and outputting all the signal through port 3. In other words, in the second stage, the hybrid is working in reverse to the first one. Simulated results when port 1 is excited are

shown in Fig. 4.19(b) which demonstrate the proper operation for this component by having excellent matching, high isolation and insertion losses about 0.2 dB. With respect to the required delay lines, 90° bends have been used including vias on each of the corners for matching purposes [37]. Moreover, phase delay adjustments for this component are made by tuning l_{delay}. The employed delay line is depicted in Fig. 4.20.

Given that the SIW width is narrower than the actual connector width, a transition had to be designed. Figure 4.21(a) shows the input SIW paths followed by each individual port. In this case, unlike the SIW delay lines, 90° curvatures [37] were

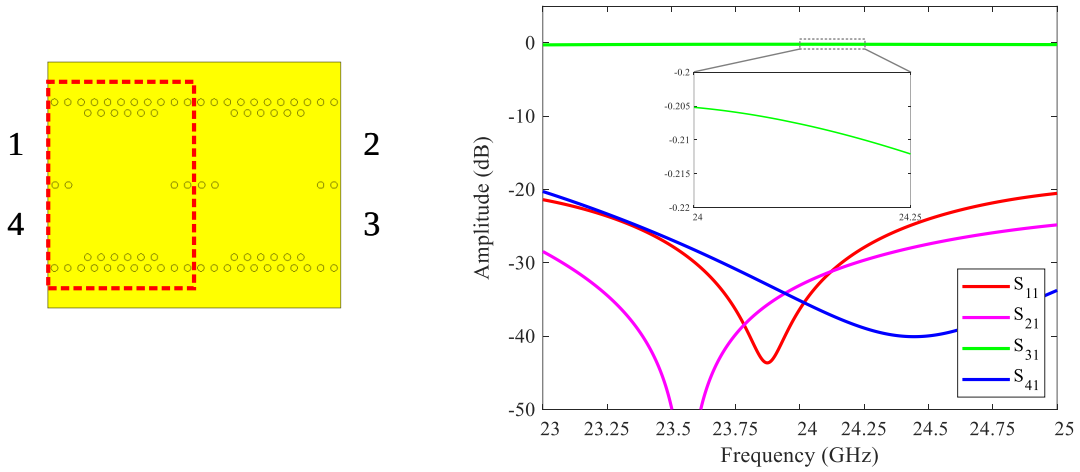

(a) (b)

Figure 4.19: Top view of the crossover which is conformed by 2 riblet short 90° hybrids (see one of them in red dashed line) (a) and S-Parameters at port 1 (b) where it can be observed that all the input power is diverted to port 3.

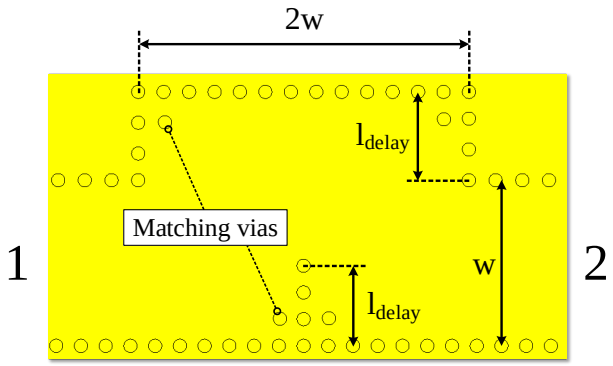

Figure 4.20: Top view of the proposed delay line.

chosen instead of 90° bends as the performance in terms of matching was better. This is likely related to the proximity of the input ports of the BM which makes this area more sensitive to mismatching problems. Also, it has to be noted that these different paths had to be properly adjusted to avoid any phase offset between them. Additionally, in Fig. 4.21(b) the transition is shown from microstrip to SIW following [38], in which it was shown that by the exponential tapering of the vias (w') that are closer to the microstrip-SIW interface, matching can be improved significantly.

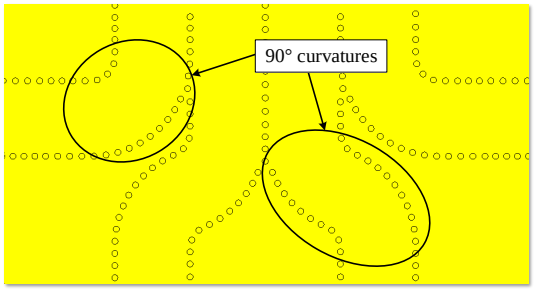

(a)

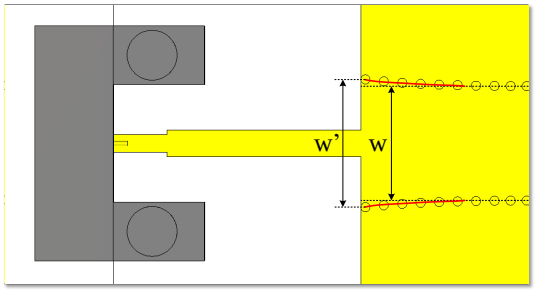

(b)

Figure 4.21: SIW bends using curvatures for better matching (a) and microstrip to SIW transition following the exponential tapering (in red) proposed in [38] (b).

A photograph of the manufactured butler matrix is shown in Fig. 4.22. As the dimensions of the via diameter and the pitch between consecutive vias was too small for in-house fabrication, Trackwise Designs PLC, a manufacturer company using printed circuit technology, was sub-contracted the manufacturing of the device, as well as the BM embedding the antenna array. Simulations and measurements of the amplitude balance for each of the four states is depicted in Fig. 4.23, where a shift in 2 dB is noticeable. This might be caused by incomplete connector modelling and losses in the microstrip lines and transitions.

On the other hand, output phase differences are shown in Fig. 4.24. It can be

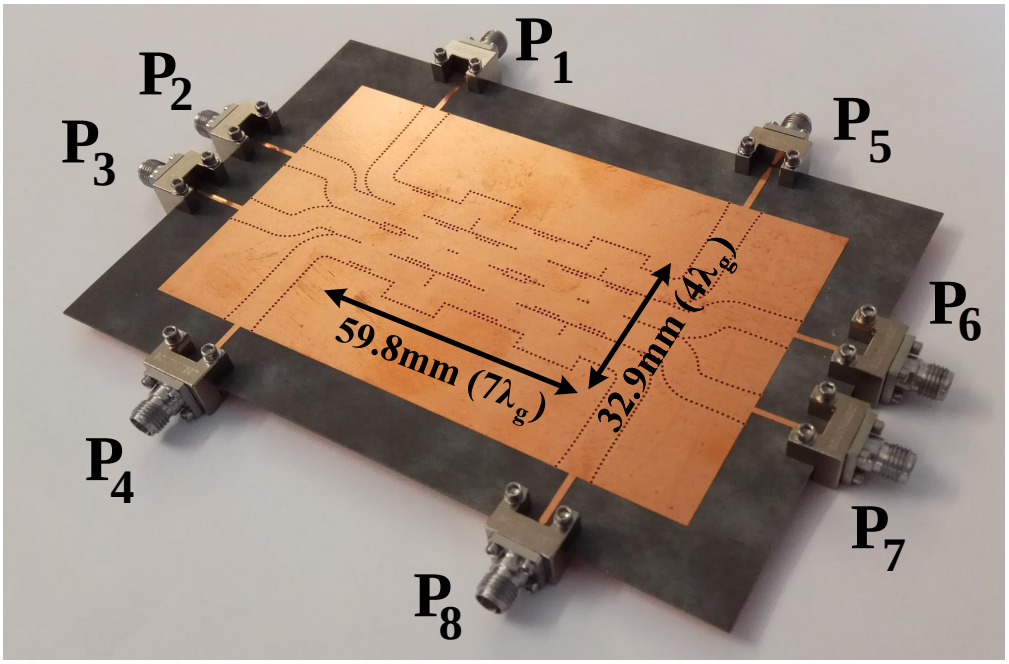

Figure 4.22: Picture of the prototyped BM. Considering P_{1-4} corresponding to the input ports, P_{5-8} are the outputs.

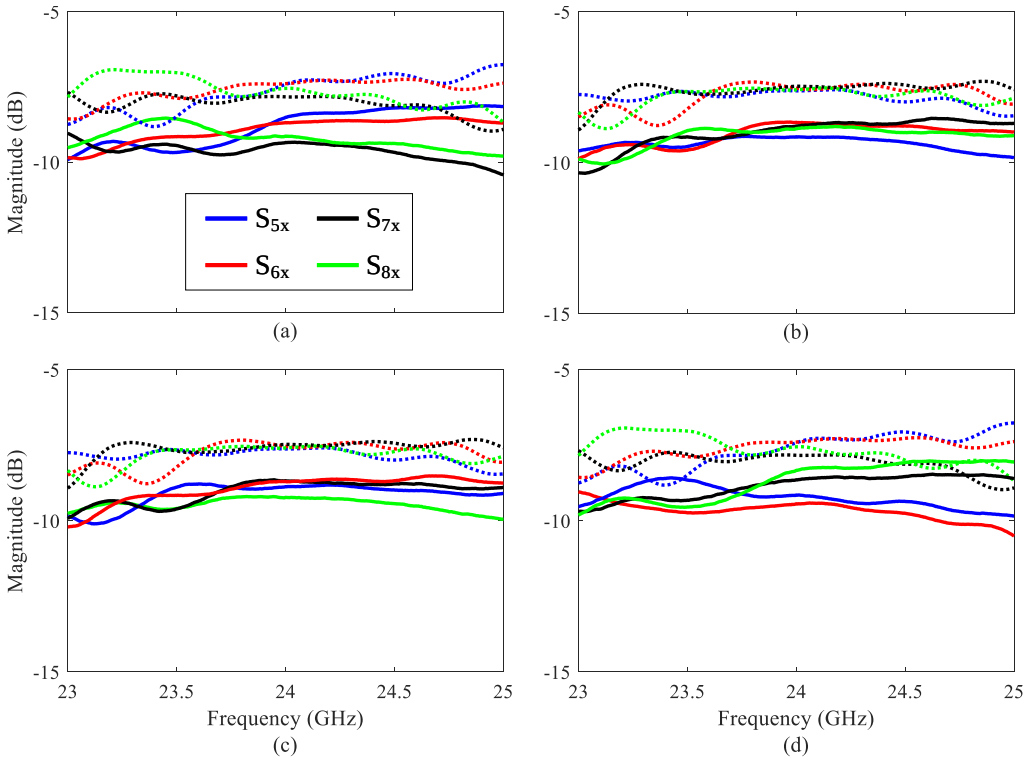

Figure 4.23: Amplitude balance when each individual input port (1-4) is excited: port 1 (a), port 2 (b), port 3 (c) and port 4 (d). Dashed lines correspond to simulations and solids lines to measurements.

seen in this Figure, that simulations and measurements match nicely each of the different beam switching states. The error between them stays within 5°, which might slightly affect in the final radiation pattern of the array in terms of beam pointing angle.

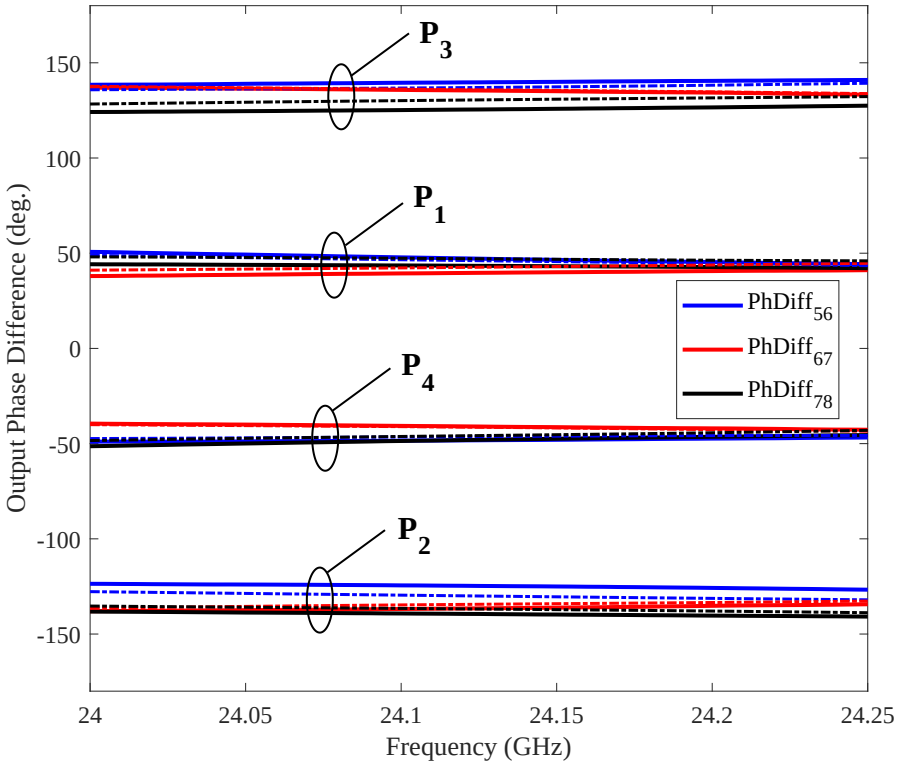

Figure 4.24: Phase differences between consecutive output ports (5-8) when each individual input port (1-4) is excited. Each of the obtained output phase states match the expected values as they are shown in Table 4.2. Dashed lines correspond to simulations whereas solid lines relate to measurements.

4.5.1 The Beamformer and Antenna Array Integration

The manufactured beamforming system is shown in Fig. 4.25. It can be noticed that the radiating slots were etched in the ground plane to avoid any unwanted coupling coming from the microstrip sections at each port. Reflection coefficients for the relevant bandwidth are shown in Fig. 4.26(a) which are below $-10\,\mathrm{dB}$. The four normalized radiation patterns, depending on the driven port, are shown in Fig. 4.26(b) showing a very good agreement between simulations and measurements. It has to be mentioned that due to the far-field scanner limitations, the measurements only cover the range that goes from $-60°$ to $60°$.

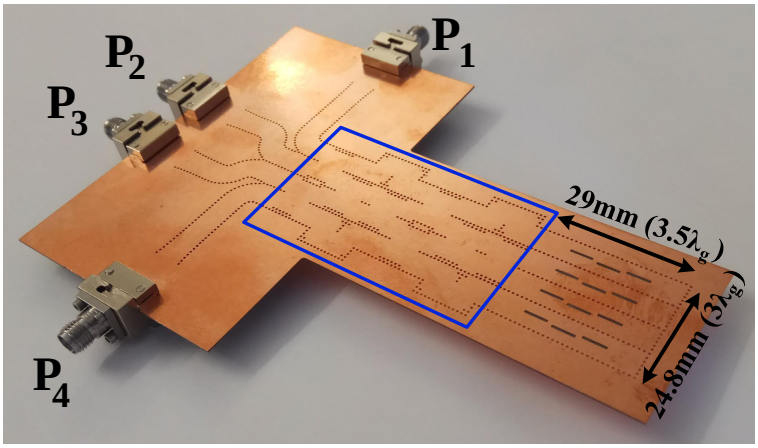

Figure 4.25: Picture of the prototyped BM (blue) and antenna array.

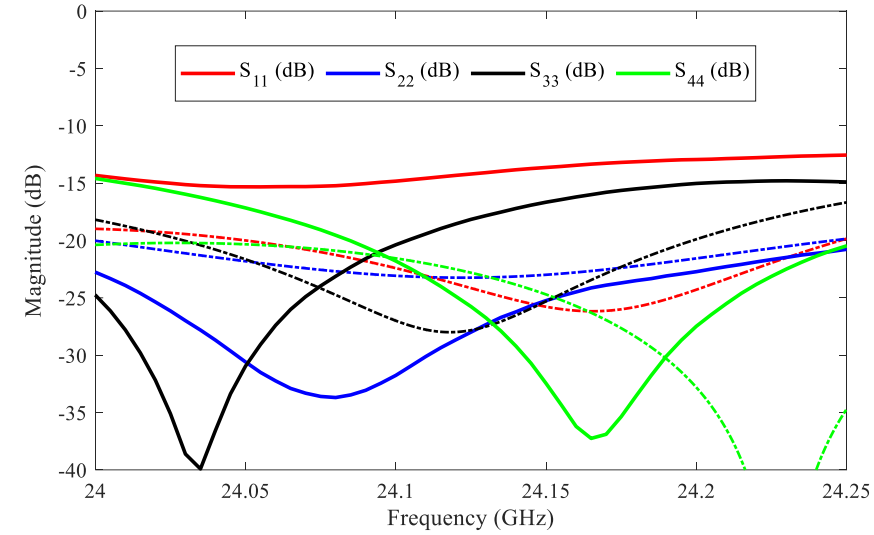

(a)

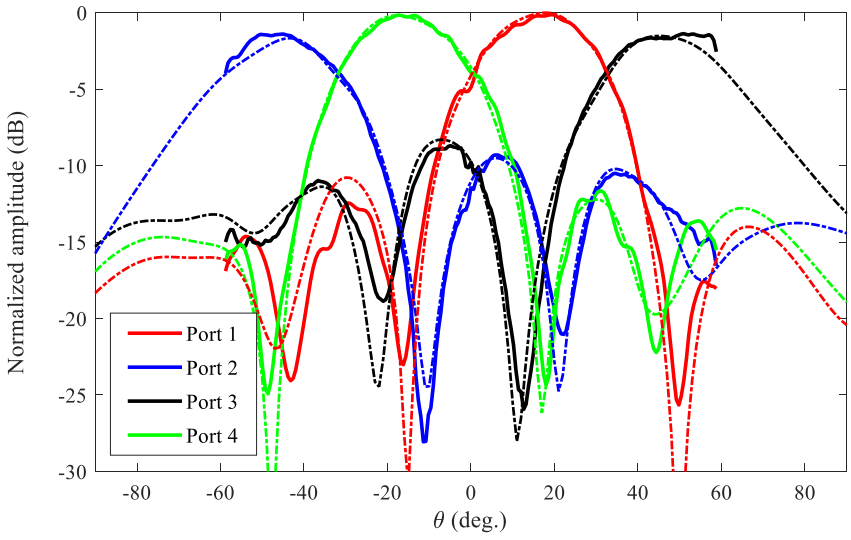

(b)

Figure 4.26: Simulated and measured reflection coefficients (a) and radiation patterns (b) for the proposed beamformer. Dashed lines correspond to simulations, while solid lines relate to measurements.

4.6 Proposed FMCW BM Radar and Developed Signal Processing

The proposed BM-radar architecture is shown in Fig. 4.27. The main difference with the classical SIMO and MIMO configurations is the inclusion of a 4×4 BM and 4×3 array at transmit. This BM is connected to the only transmitter of the system which will provide four different views depending on the port excited. Such views, which sectorize the space in 4 angular sections, combined in post-processing with the signal post-processing technique called Pwr_+, will provide improved angular resolution along with a more optimized total processing time. These developments will be further described in this section.

But before the design was pursued, preliminary validation studies regarding the delay of the system were made to understand the performance of the BM radar over a conventional 4×4 MIMO radar in terms of processing time. The three different scenarios are: 1×4 SIMO, 4×4 MIMO and the proposed BM radar. This one could be considered as a 1×4 SIMO but with the benefit that the BM provides four different views with less RF chains. To do so, every time one image is received, the transmitter is switched to the next BM port as it can be seen in Fig. 4.27(a).

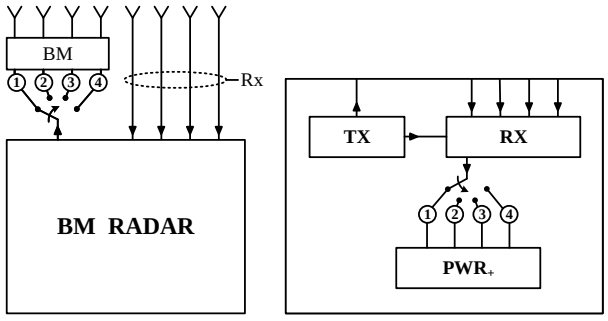

Figure 4.27: Schematic of the proposed BM radar system (a) and a more detailed schematic for the BM radar box (b), where each of the 4 states of the switch are individually processed in the Pwr_+ box, providing parallel computation as shown in Fig. 4.28(c).

Timing diagrams for the signal processing shown in Fig. 4.28(a,b and c) give an estimation of the total delay that starts from the moment that the transmitter sends the signal and finishes right at the moment at which the information of the target

position is acquired. In such diagrams, there are 4 different types of timing blocks:

1. R: time that starts from the moment at which the transmitter starts sending the pilot signal to the air. This signal hits the target and finishes with the reception of this raw data at the receivers. It depends on the distance to the target (d) and the time that the receiver block takes to record and store the received RAW data, which is the limiting factor (t_{storage}). Therefore, the factor that relates to the distance to the target can be neglected, given that $t_{\text{storage}} \gg \frac{2d}{c}$.
$$R = \frac{2d}{c} + t_{\text{storage}}$$

2. 1×4 SIMO: time needed by the system to process the RAW data and obtain the information of the target position, which is approximately 36 ms (as processed in MATLAB, see Fig. 4.28(d)).

3. 4 × 4 MIMO: time needed by the system to process the RAW data, once the four different views have been received and ready to process, which is approximately 125 ms.

4. Pwr_+: time needed to apply the proposed Pwr_+ algorithm right after the four views have been acquired by SIMO processing, which is approximately 0.3 ms.

All the estimations for the duration of each block were obtained by running 1000 iterations of the MATLAB (R2017b) code that performs the relevant radar processing, as it is shown in Fig. 4.28(d). The OS of the PC used for these simulations is Windows 10 running on the Intel(R) Core(TM) i7-4790 CPU, which works at 3.60 GHz, with 4 cores and 8 logical processors and 16 GB of RAM. Therefore, the total required time for each scenario is:

$$\Delta t_{\text{SIMO}} = t'_1 - t'_2 = R + t_{1\times4\,\text{SIMO}} = R + 36\,\text{ms}$$

$$\Delta t_{\text{MIMO}} = t''_1 - t''_2 = 4R + t_{4\times4\,\text{MIMO}} = 4R + 125\,\text{ms}$$

$$\Delta t_{\text{BM}-\text{Pwr}_+} = t_1 - t_2 = 4R + t_{1\times4\,\text{SIMO}} + t_{\text{Pwr}_+} = 4R + 36.3\,\text{ms}$$

where R is considered much less significant than the other factor. Taking into account the three different scenarios under comparison (classic 1 × 4 SIMO, classic 4 × 4 MIMO and the proposed architecture), it can be seen how the proposed architecture ($\Delta t_{\text{BM}-\text{Pwr}_+}$) is significantly faster than the classic 4 × 4 MIMO (Δt_{MIMO}), as shown in Fig. 4.2.

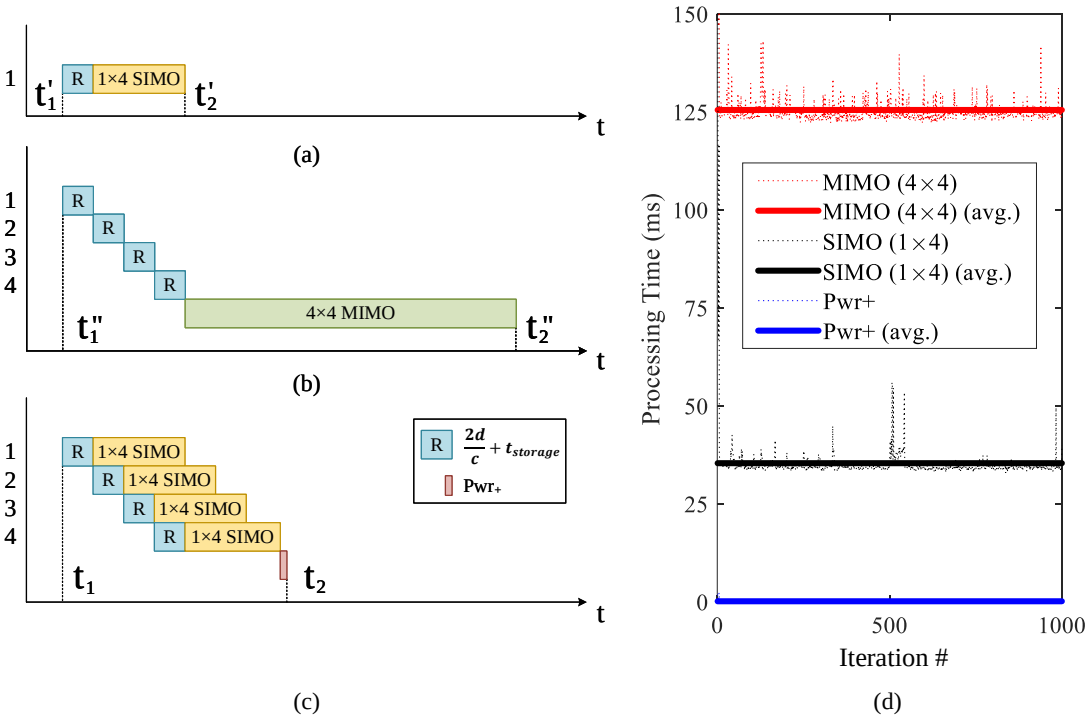

Figure 4.28: Timing sequence diagram for the three different systems under comparison: 1×4 SIMO (a), 4×4 MIMO (b) and the proposed *BM-Pwr*$_+$ (c). Estimation of the processing time for each of the boxes that are shown in the timing diagrams (d).

4.6.1 Developed Signal Combining Approach (*Pwr*$_+$) using Butler Matrices

The proposed *BM-Pwr*$_+$ procedure, illustrated in Fig. 4.29, is as it follows (see Fig. 4.27):

1. Both switches are synchronized to be at the same position from 1 to 4. Then, the BM is excited through the first port and the scattered signal back from the targets is collected by the 4 receivers and stored into the *Pwr*$_+$. Once the signal has been completely stored, both switches are changed to the next position, and right after the signal is processed as a conventional 1×4 SIMO radar. It has to be noted that within the *Pwr*$_+$ block it includes 4 independent processors to avoid queues that could make the total delay longer (see Fig. 4.28(c)). The process is repeated 4 times in sequence.

2. When the 4 datasets have been processed to describe their own individual

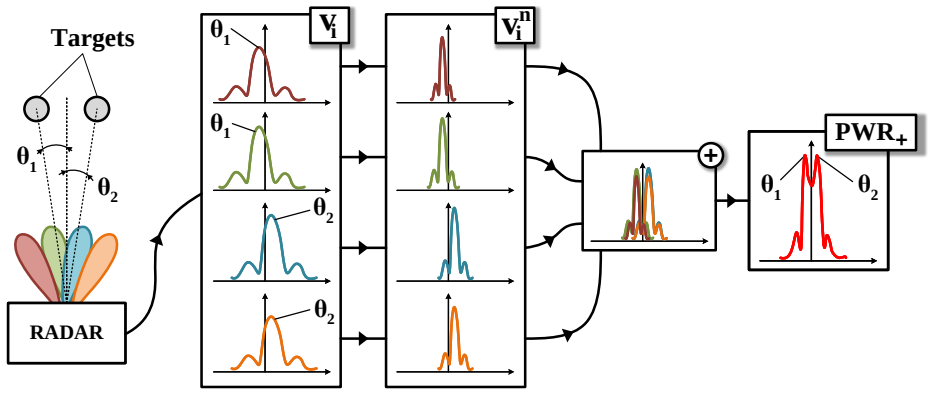

Figure 4.29: Working procedure of the proposed *Pwr+* algorithm, given two targets located at angles θ_1 and $\theta 2$. Each individual view is multiplied by itself n times and added afterwards. The resulting angle target estimate plot is shown in red.

target angular position estimates, they are then combined by the following algorithm:

$$v_{\mathrm{Pwr}_+} = v_1^n + v_2^n + v_3^n + v_4^n$$

where, v_i represents each independent view, and n corresponds to a positive integer greater than 1.

This makes the final view (v_{Pwr_+}) for the total radar to be sharper and more well defined. Therefore, the radar will work faster improving the resolution over the conventional SIMO while exhibiting a performance better than a MIMO system in terms of processing time (see Section 4.6). The reasoning behind making to make the power to the n for each individual radar view, is to achieve a sharper individual pattern so that when addition of all four views is made, two targets that are below the angular resolution of an individual view can be easily distinguished.

4.7 Radar System Results

In order to test the capabilities of the proposed radar system, a set of measurements in the anechoic chamber at Heriot-Watt University have been made. Fig. 4.30(a) shows the proposed butler matrix antenna (BMA) as the transmitter. The results reported in this chapter were obtained by manually switching the ports of the BMA and terminating the other three with 50Ω loads. The antenna array shown in the bottom of the same figure corresponds to the receiver, where only the four central elements of the array have been used, following the aforementioned architecture

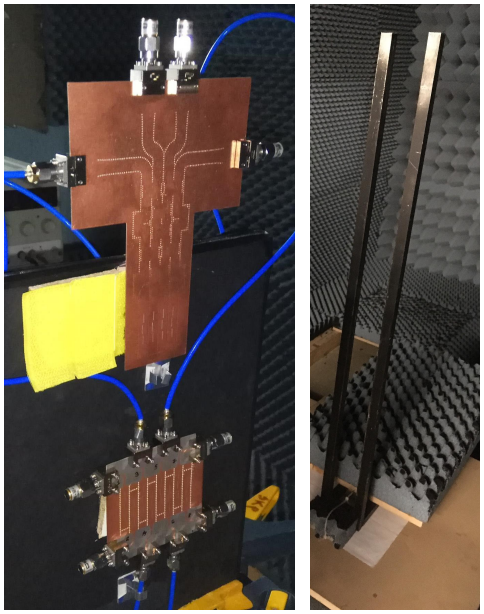

(a) (b)

Figure 4.30: Proposed transmit RF beamformer (top) and the 4 element receiver (bottom) (a). Metallic posts employed as targets in the measurements (b).

depicted in Fig. 4.27. Each of the receivers is connected to an HMC751LC4 LNA amplifier from Analog Devices in order to reduce the overall noise of the system, and increasing significantly the maximum detectable range. The employed radar system electronics are the EVAL-RADAR-MMIC from Analog Devices and the obtained RAW data has been post-processed through MATLAB. It should be noted that the measurements were made at a range of around 2 meters using as targets the two vertical metallic posts shown in Fig. 4.30(b).

The measurement procedure was very simple. As already mentioned before, each port of the BMA is excited individually, collecting at the radar module, almost instantly, the returned scattered signal by the targets and processed them as an individual SIMO radar. Once the four views are obtained, the Pwr_+ algorithm is applied. However, due to the fact that each individual view has an angular resolution above the angle between the two targets, the resulting view will only show one peak that will point to the target position which is closer in angle to the transmitting beam maxima of the BMA. This fact limits the number of detectable targets to four, corresponding to the number of different transmit beams that the system exhibits, but since the system will be used in the front bumper of a car, it will be challenging to face more than four targets at once making the proposed system very convenient for automotive radar applications and collision avoidance.

Table 4.3: Comparison of a 4×4 MIMO radar with the proposed BM radar

	4×4 MIMO	PWR+ ($n = 20$)	PWR+ ($n = 50$)	PWR+ ($n = 100$)	PWR+ ($n = 1000$)
3dB Beamwidth (deg.)	7.18	9.4	5.91	4.18	1.42
Delay (ms)	$4R + 125$	$4R + 36.0933$	$4R + 36.099$	$4R + 36.1011$	$4R + 36.1112$
Δt (ms)	0	-88.9067	-88.901	-88.8989	-88.8888

[1] Δt refers to the total delay ($t_2 - t_1$, see Fig. 4.28(c)), with respect a 4×4 MIMO case. Negative values mean a shorter processing time than the referenced case.

Some results are shown in Fig. 4.31, where the two targets are separated 10, 6, 4 and 2 degrees, respectively. The grey lines show the independent SIMO views corresponding to 30° of angular resolution, and the coloured lines are the resulting shape after applying Pwr_+ for different n values. It should be noted that the resolution improves with the increment of n, as Table 4.3 also shows. The only possible inconvenience of increasing n in the algorithm is a possible increase of the total processing time. However, this time increase is negligible as previously described in this chapter (see Table 4.3), making the proposed algorithm in combination with an RF beamformer in transmit a nice approach to improve the total processing time while maintaining high angular resolution if a proper value of n is selected.

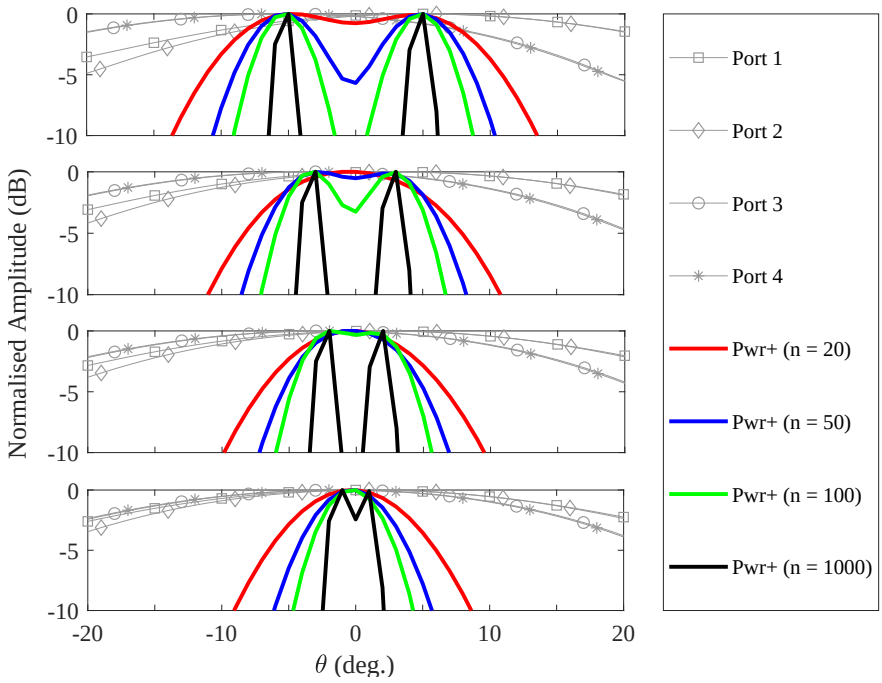

Figure 4.31: Radar measurements where two targets are resolved using the Pwr_+ algorithm for different values of n. Targets positioned at a distance of 2 meters and: ±5°, ±3°, ±2° and ±1°.

4.8 Conclusion

This chapter presents the *butler-matrix-pwr+* technique for improving the processing time in FMCW-MIMO radars by the use of a passive BM beamformer at transmit in combination with an algorithm that combines each independent view in a way that also improves the angular resolution. An SIW butler matrix connected to an antenna array has also been designed as part of the proposed radar, and good agreement between simulations and measurements has been observed. The proposed system, composed by one transmit connected to the BMA and four receivers is compared in resolution and total delay with a conventional 4×4 MIMO radar, showcasing an overall better performance. For example, measurement results show that targets can be resolved up to 2 degrees apart which would require a conventional 7×8 MIMO radar to achieve the same angular resolution.

References

[1] D. W. Bliss and K. W. Forsythe, "Multiple-input multiple-output (mimo) radar and imaging: degrees of freedom and resolution," in *The Thrity-Seventh Asilomar Conference on Signals, Systems Computers, 2003*, vol. 1, Nov 2003, pp. 54–59.

[2] E. Fishler, A. Haimovich, R. Blum, D. Chizhik, L. Cimini, and R. Valenzuela, "Mimo radar: an idea whose time has come," in *Proceedings of the 2004 IEEE Radar Conference (IEEE Cat. No.04CH37509)*, April 2004, pp. 71–78.

[3] I. Bekkerman and J. Tabrikian, "Target detection and localization using mimo radars and sonars," *IEEE Transactions on Signal Processing*, vol. 54, no. 10, pp. 3873–3883, Oct 2006.

[4] A. M. Haimovich, R. S. Blum, and L. J. Cimini, "Mimo radar with widely separated antennas," *IEEE Signal Processing Magazine*, vol. 25, no. 1, pp. 116–129, 2008.

[5] N. H. Lehmann, A. M. Haimovich, R. S. Blum, and L. Cimini, "High resolution capabilities of mimo radar," in *2006 Fortieth Asilomar Conference on Signals, Systems and Computers*, Oct 2006, pp. 25–30.

[6] K. Ogawa and A. Kajiwara, "2d high resolution of stepped-fm radar based on music scheme," in *2018 IEEE Topical Conference on Wireless Sensors and Sensor Networks (WiSNet)*, Jan 2018, pp. 51–54.

[7] P. Stoica and A. Nehorai, "Music, maximum likelihood, and cramer-rao bound: further results and comparisons," *IEEE Transactions on Acoustics, Speech, and Signal Processing*, vol. 38, no. 12, pp. 2140–2150, Dec 1990.

[8] R. Schmidt, "Multiple emitter location and signal parameter estimation," *IEEE Transactions on Antennas and Propagation*, vol. 34, no. 3, pp. 276–280, Mar 1986.

[9] C. Vaidyanathan and K. M. Buckley, "Performance analysis of the mvdr spatial spectrum estimator," *IEEE Transactions on Signal Processing*, vol. 43, no. 6, pp. 1427–1437, Jun 1995.

[10] R. Roy, A. Paulraj, and T. Kailath, "Esprit–a subspace rotation approach to estimation of parameters of cisoids in noise," *IEEE Transactions on Acoustics, Speech, and Signal Processing*, vol. 34, no. 5, pp. 1340–1342, Oct 1986.

[11] J. Capon, "High-resolution frequency-wavenumber spectrum analysis," *Proceedings of the IEEE*, vol. 57, no. 8, pp. 1408–1418, Aug 1969.

[12] R. Mucci, "A comparison of efficient beamforming algorithms," *IEEE Transactions on Acoustics, Speech, and Signal Processing*, vol. 32, no. 3, pp. 548–558, Jun 1984.

[13] ITU, "Radio regulations," pp. RR5–30, 2016, section 5.150.

[14] K. Ramasubramanian, K. Ramaiah, and A. Aginskiy, "Moving from legacy 24 ghz to state-of-the-art 77 ghz radar," Texas Instrument, Tech. Rep., October 2017.

[15] L. Brown, *A Radar History of World War II: Technical and Military Imperatives*. Institute of Physics Publishing, 1999.

[16] "Sawtooth wave," http://mathworld.wolfram.com/SawtoothWave.html, accessed: 2019-04-23.

[17] C. A. Alistarh, P. D. H. Re, T. M. Strober, S. A. Rotenberg, S. K. Podilchak, C. Mateo-Segura, Y. Pailhas, G. Goussetis, Y. Petillot, J. Thompson, and J. Lee, "Millimetre-wave fmcw mimo radar system development using broadband siw antennas," in *12th European Conference on Antennas and Propagation (EuCAP 2018)*, April 2018, pp. 1–5.

[18] C. Balanis, *Antenna Theory: Analysis and Design*. Wiley, 2015.

[19] S. Rao, "MIMO Radar," Texas Instruments, Tech. Rep., May 2017.

[20] J. Blass, "Multidirectional antenna - a new approach to stacked beams," in *1958 IRE International Convention Record*, vol. 8, March 1960, pp. 48–50.

[21] R. F. Gleason and R. M. Greene, "A wide-aperture HF direction-finder with sleeve antennas," U. S. Naval Research Laboratory, Tech. Rep., August 1958.

[22] J. Butler and R. Lowe, "Beam-forming matrix simplifies design of electronically scanned antennas," *Electronic Design*, pp. 170–173, April 1961.

[23] H. Moody, "The systematic design of the butler matrix," *IEEE Transactions on Antennas and Propagation*, vol. 12, no. 6, pp. 786–788, November 1964.

[24] T. MacNamara, "Simplified design procedures for butler matrices incorporating 90 hybrids or 180 hybrids," *IEE Proceedings H - Microwaves, Antennas and Propagation*, vol. 134, no. 1, pp. 50–54, February 1987.

[25] K. Wu, D. Deslandes, and Y. Cassivi, "The substrate integrated circuits - a new concept for high-frequency electronics and optoelectronics," in *6th International Conference on Telecommunications in Modern Satellite, Cable and Broadcasting Service, 2003. TELSIKS 2003.*, vol. 1, Oct 2003, pp. P–III.

[26] F. Xu and K. Wu, "Guided-wave and leakage characteristics of substrate integrated waveguide," *IEEE Transactions on Microwave Theory and Techniques*, vol. 53, no. 1, pp. 66–73, Jan 2005.

[27] D. Pozar, *Microwave Engineering, 4th Edition.* Wiley, 2011, p. 119.

[28] R. Rao, *Microwave engineering*, 2nd ed. PHI Learning, 2015, p. 219.

[29] R. Elliott, "An improved design procedure for small arrays of shunt slots," *IEEE Transactions on Antennas and Propagation*, vol. 31, no. 1, pp. 48–53, January 1983.

[30] R. Elliott and W. O'Loughlin, "The design of slot arrays including internal mutual coupling," *IEEE Transactions on Antennas and Propagation*, vol. 34, no. 9, pp. 1149–1154, Sep. 1986.

[31] A. T. Alreshaid, M. S. Sharawi, S. Podilchak, and K. Sarabandi, "Compact millimeter-wave switched-beam antenna arrays for short range communications," *Microwave and Optical Technology Letters*, vol. 58, no. 8,

pp. 1917–1921, 2016. [Online]. Available: https://onlinelibrary.wiley.com/doi/abs/10.1002/mop.29940

[32] Q. Yang, Y. Ban, J. Lian, Z. Yu, and B. Wu, "Siw butler matrix with modified hybrid coupler for slot antenna array," *IEEE Access*, vol. 4, pp. 9561–9569, 2016.

[33] S. E. Hosseininejad and N. Komjani, "Optimum design of traveling-wave siw slot array antennas," *IEEE Transactions on Antennas and Propagation*, vol. 61, no. 4, pp. 1971–1975, April 2013.

[34] A. J. Farrall and P. R. Young, "Integrated waveguide slot antennas," *Electronics Letters*, vol. 40, no. 16, pp. 974–975, Aug 2004.

[35] H. J. Riblet, "The short-slot hybrid junction," *Proceedings of the IRE*, vol. 40, no. 2, pp. 180–184, Feb 1952.

[36] L. T. Hildebrand, "Results for a simple compact narrow-wall directional coupler," *IEEE Microwave and Guided Wave Letters*, vol. 10, no. 6, pp. 231–232, June 2000.

[37] D. Deslandes and K. Wu, "Design consideration and performance analysis of substrate integrated waveguide components," in *2002 32nd European Microwave Conference*, Sep. 2002, pp. 1–4.

[38] E. Diaz Caballero, A. Belenguer Martinez, H. E. Gonzalez, O. M. Belda, and V. B. Esbert, "A novel transition from microstrip to a substrate integrated waveguide with higher characteristic impedance," in *2013 IEEE MTT-S International Microwave Symposium Digest (MTT)*, June 2013, pp. 1–4.

Chapter 5

Conclusions and future work

5.1 Conclusions

This thesis has investigated new antenna array designs and microwave circuit systems for retrodirective wireless power transmission and radar. After a comprehensive analysis of the available techniques found in the literature on wireless power transmission (WPT) and multiple-input-multiple-output (MIMO) radar, new approaches are presented which focus on achieving a balance between performance and simplicity while reducing costs while achieving performance which advances the state-of-the-art.

In Chapter 2, the most common retrodirective antenna array (RDA) types have been introduced. Moreover, a tracking performance analysis in the near-field (NF) region has been carried out with a simple prototype in order to demonstrate that a Pon RDA can work in this region, and therefore, can be the right choice for the intended application of WPT for the wireless charging of handheld devices in the near-field and the far-field. The newly proposed system offers one-dimensional target object tracking and removes the need of circulators, having independent transmit and receive antennas but with opposite polarizations, which improve the isolation between transmit and receive paths. It has been also designed to enable circular polarization (CP) for orientation flexibility of the device under charge (DUC). Moreover, a study to assess the performance of a prototype which uses subarrays in transmit has been carried out, and it has been confirmed to be a feasible option to achieve the targeted goals of received power for a distance between the RDA and

DUC of 50 cm (considering an initial beacon tone of 6.6 dBm transmitted from the DUC for direction finding) [1]. Additionally, a passive Van Atta RDA has been presented which removes the need of circulators and bidirectional amplifiers. It also has the ability to work as a monopulse radar antenna which also can enable two-dimensional retrodirective operation for WPT and mobile phone charging. [2].

Chapter 3 discusses a new antenna array design which is an alternative to the subarray proposed in Chapter 2. The motivation for this new design was to achieve more compactness, enabling a shorter distance between subarrays which can allow for the suppression of grating lobes and an improvement in the side lobe level (SLL). To do so, a higher relative dielectric constant for the substrate and meandered lines have been used. These meander lines are needed to synchronize the elements for uniform excitation, and also to achieve the proper phase difference that enables CP operation for each antenna. Additionally, by the use of transmission line impedance transformers, the designer can choose the desired amplitude distribution by changing the corresponding transmission line widths and lengths. Measurements and simulations are presented along with a comparison to other relevant works, showing a very good performance for applications such as WPT, radar, and retrodirective arrays [3].

In Chapter 4 an initial comparison between SIMO and MIMO radars has been made in terms of angular resolution and processing time. Basic concepts for those radars have been introduced as well as frequency-modulated-continuous-wave (FMCW) radar. These systems have application to automotive radar systems and self-driving vehicles. From this initial study, a technology gap has been identified that requires a balance between angular resolution and processing time. This is generally because to achieve higher angular resolutions MIMO radars are preferred, but at the same time can lead to complicated signal processing and increased computation time. These challenges gave way to the proposed butler matrix antenna array design for a SIMO radar system as newly developed in this thesis. The antenna design is based on substrate integrated waveguide (SIW) technology and is divided in two elements: first, the butler matrix (BM), which brings the possibility of discrete beamforming depending on the excited port. And second, the antenna array formed by four subarrays, where each of those is a standing-wave slot antenna array. Measurements and simulations of the design have also been reported. Finally, a new and simple

processing technique called Pwr_+ has been proposed, which takes the four individual target images generated by the SIMO radar, and applies this algorithm that allows for the target angular estimation patterns to be sharper when compared to more conventional approaches. This allows for an improvement of the angular resolution of the radar while also performing computations faster than more conventional MIMO radar processing [4].

In general, the research and development carried out in this thesis demonstrates that novel and creative solutions are possible when striving for simplicity and cost savings. Moreover, these new systems can also provide performance improvements when compared to more conventional approaches. Both WPT and automotive radar are developing very fast as they are a very hot topic nowadays, and this is the main reason why achieving a balance between costs and performance is very desirable and that such research activities should be encouraged.

5.2 Future Work

The topics covered in this thesis open potential lines of future work:

- In Chapter 2, the transmitting power amplifiers are directly connected to the transmit antenna subarrays. Given that the measured return losses at the frequency of operation are not negligible and, at the same time, the output power on each of the power amplifier is relatively high (about 30 dBm), a considerable amount of power is reflected back to the amplifiers. This effect can potentially degrade their performance with time, so a possible solution would be to introduce circulators between them or another more advanced circuit antenna system that recycles and re-radiates any back reflected power. Additionally, in order to make the system more efficient, signals with a certain bandwidth could also be considered, to improve the overall efficiency [5].

- In Chapter 3, the proposed series-fed array was originally designed to have the meanders that control the inter-element phase synchronization oriented to the bottom, to make the design as compact as possible. However, given that the bottom part of the meanders were very close to the corner of the patches, there was coupling causing degradation of the axial ratio. A quick solution to this

issue was to flip the meanders upwards as done in this thesis. Nevertheless, this makes the width of the subarray broader making it not very convenient if additional sub-arrays were used to form a bigger array. This is because the distance between each sub-array would be beyond $\lambda_0/2$, causing grating lobes to appear and an unwanted increment of the SLL. Therefore, future work for this design could be to find a solution to this problem. For example, instead of the meanders (which take up additional space) metamaterial transmission line sections could be introduced, or some other type of compact reactive loading to achieve the required phasing between the radiating patches.

- In Chapter 4, the Pwr_+ algorithm was computed by using a desktop computer. A good activity for the future could be to make the processing in a smaller device such as a *Raspberry-Pi* or another similar microcontroller for system integration. Also, scaling up the system in frequency to the 77 GHz frequency band would take advantage of the benefits of SIW antennas in terms of broad impedance bandwidth.

References

[1] P. D. Hilario Re, S. K. Podilchak, S. Rotenberg, G. Goussetis, and J. Lee, "Circularly Polarized Retrodirective Antenna Array for Wireless Power Transmission," *IEEE Transactions on Antennas and Propagation*, 2019, (submitted).

[2] P. Le Bihan, P. D. Hilario Re, D. Comite, S. K. Podilchak, C. Tucker, K. MacColl, Y. Zhaksylyk, M. Garca-Vigueras, and G. Goussetis, "Dual-Polarized Aperture-Coupled Patches with Application to Retrodirective and Monopulse Arrays," *IEEE Transactions on Antennas and Propagation*, 2019, (submitted).

[3] P. D. Hilario Re, D. Comite, and S. K. Podilchak, "Single-Layer Series-Fed Array with Controlled Aperture Distribution for Circularly Polarized Radiation," *IEEE Access*, 2019, (submitted).

[4] P. D. Hilario Re, C. Alistarh, S. K. Podilchak, G. Goussetis, J. Thompson, and J. Lee, "Millimeter-wave fmcw radar development using siw butler matrix for time domain beam steering," in *2019 16th European Radar Conference (EuRAD)*, 2019, (accepted).

[5] C.-G. Sun and J.-L. Li, "Wideband time reversal of microwave signals based on phase conjugating," *Radioengineering*, vol. 27, pp. 1085–1091, 09 2018.

Appendix A

A.1 Measuring CP

The DAMS 7000 far-field positioner from Diamond Engineering has been used in order to measure the patterns reported in this thesis. A linear polarized horn was used and therefore, two measurements were needed to obtain each of the CP patterns (one horizontal and one vertical). Then, the expression for the horizontal and vertical field components is shown in Eq. A.1.1, and in Eq. A.1.2 it is shown the expression that relates the horizontal and vertical components with the CP components. The measurement setup is shown in Fig. A.1.

$$E_1 = E_{+1}e^{j\theta} \qquad E_2 = E_{+2}e^{j\phi} \tag{A.1.1}$$

$$E_{LHCP} = \frac{1}{\sqrt{2}}\left(E_1 - jE_2\right) \qquad E_{RHCP} = \frac{1}{\sqrt{2}}\left(E_1 + jE_2\right) \tag{A.1.2}$$

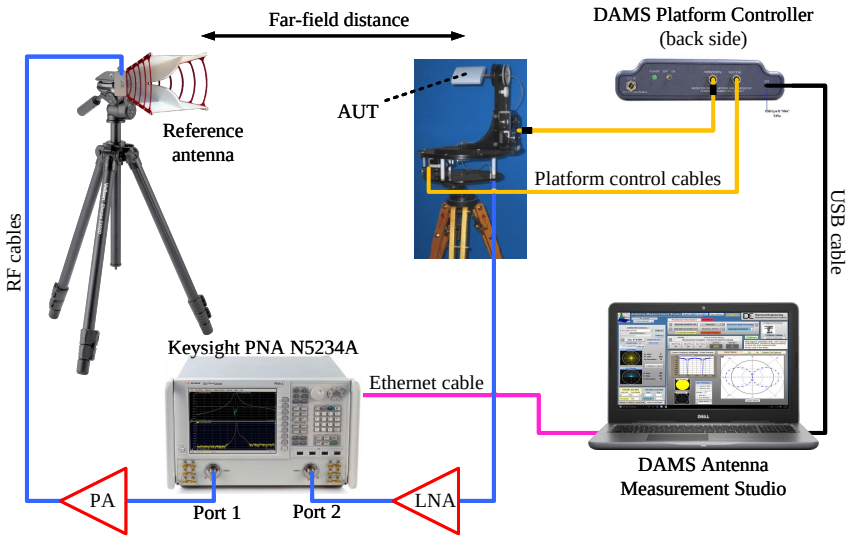

Figure A.1: Measurement setup to obtain the radiation patterns. AUT refers to the antenna under test.